

Hybrid Halide Perovskite-Based Near-Infrared Photodetectors and Imaging Arrays

Luyao Mei, Runfeng Huang, Chaorong Shen, Jianguo Hu, Pu Wang, Zhengji Xu, Zhanfeng Huang, and Lu Zhu*

Hybrid halide perovskites have been demonstrated to be prospective materials in optoelectronic devices due to their outstanding photoelectric properties and facile manufacturability by low-cost and fast solution-processed methods. Particularly, to meet increasingly potential applications in near-infrared (NIR) detection and imaging, perovskites have been introduced and explored their roles, some of which achieve the comparable performance with traditional silicon counterparts. Here, the recent advancements of hybrid halide perovskite-based NIR photodetectors and imaging arrays in terms of perovskite formation, device structures, working mechanisms, and device performances are reviewed. Pb perovskite-based devices either employ sub-bandgap absorption and intraband transition, or incorporate with narrow-bandgap semiconductors to achieve NIR detection, which could reach the spectral response onset at 2.6 μm wavelength. Sn perovskite-based devices employ the strategies of template-assisted engineering and reducing additives to inhibit the oxidation of Sn^{2+} states for efficient detection. Sn–Pb mixed perovskite devices employ compositional engineering, passivation strategies, crystallization tuning, and encapsulation to achieve efficient and long shelf-life photodetectors with an external quantum efficiency of 70% at 940 nm wavelength. Finally, potential prospects are proposed, including spectral response extension, pixel integration, flexible devices, and stability, to advance perovskite-based NIR detection and imaging toward commercial applications.

1. Introduction


Photodetectors (PDs) are the essential component of various modern photodetection and imaging techniques, including spectroscopy, optical fiber communication, silicon-based complementary metal-oxide semiconductor (CMOS) image sensing,

light detection and ranging, X-ray imaging, biomedical imaging, etc.^[1–4] Photodetection processes generally involve photon absorption, carrier generation and extraction, signal storage, data processing, and subsequent signal reconstruction, which convert incident optical signals that could carry the modulated photon information into processable electrical signals. Biologically, compared with UV (200–400 nm) and visible-light (400–780 nm) PDs, near-infrared (NIR) PDs with the typical spectral response of 780–1100 nm and up to 1800 nm could capture more fluorescent information of biological molecules and tissue structures since NIR photons achieve the improved tissue penetration depth of $\approx 1\text{--}20$ mm.^[5] Apart from biomedical fluorescence imaging, NIR PDs exhibit increasing potentials in other emerging scientific and industrial applications, as selected in **Figure 1**, including autonomous driving, food security monitoring, machine vision, functional NIR spectroscopy, biometric identification, smart agriculture, etc.^[6–11]

Nowadays, photoactive materials of commercially available NIR PDs are usually composed of silicon (detecting down to 1100 nm), germanium (detecting 800–1800 nm), or indium gallium arsenide (InGaAs, detecting 800–1700 nm).^[12] Typically, the film growth of these inorganic narrow-bandgap semiconductor crystals requires the strict high temperature and high vacuum environment. The complexity of fabrication processes and rigid nature of these inorganic materials are also the inevitable obstacle for their applications in flexible electronics. Alternatively, low-temperature and solution-processed narrow-bandgap materials are an emerging and promising class of NIR photoactive semiconductors. Benefiting from the bandgap tunability and solution availability, organic semiconductors (small molecules and polymers) and inorganic quantum dots (QDs) have been intensively investigated in past decades.^[13,14] A few number of organic semiconductors have been employed to achieve NIR detection. Moreover, the electrical disorder nature of organic semiconductors could result in the low carrier mobility and thus influence external quantum efficiency (EQE) and the response speed of organic NIR PDs.^[14,15] Although surface traps of inorganic QDs greatly contribute to the photocurrent gain, excess surface traps simultaneously limit the carrier transport and thus significantly lower the -3 dB bandwidth (typical less than 100 Hz).^[12,15]

L. Mei, R. Huang, C. Shen, P. Wang, Z. Xu, Z. Huang, L. Zhu
Guangdong Provincial Key Laboratory of Optoelectronic Information
Processing Chips and Systems
School of Microelectronics Science and Technology
Sun Yat-sen University
Zhuhai 519082, China
E-mail: zhulu5@mail.sysu.edu.cn

J. Hu
School of Microelectronics Science and Technology
Sun Yat-sen University
Zhuhai 519082, China

 The ORCID identification number(s) for the author(s) of this article can be found under <https://doi.org/10.1002/adom.202102656>.

DOI: 10.1002/adom.202102656

Solution-processed and low-temperature hybrid halide perovskites possess the excellent photoelectric properties of high absorption coefficients ($\approx 10^5 \text{ cm}^{-1}$), tunable bandgaps (2.88–1.17 eV), excellent defect tolerance and low mid-gap defect densities, high carrier mobilities, long carrier lifetimes, and diffusion lengths.^[17–19] These remarkable properties enable perovskites to become the limelight in optoelectronic devices, including X-ray imaging,^[20–22] UV–vis–NIR PDs,^[23–26] solar cells,^[27] light emitting diodes,^[28,29] and lasers.^[30] Generally, perovskites have a common composition formula of ABX_3 (Figure 2a), where A shall be larger cations (e.g., methylammonium (CH_3NH_3^+ , MA^+), formamidinium ($\text{HN} = \text{CHNH}_3^+$, FA^+), cesium (Cs^+), rubidium (Rb^+), or their mixtures), B shall be smaller cations (e.g., lead (Pb^{2+}), tin (Sn^{2+}), or their mixtures), X shall be an anion (e.g., chlorine (Cl^-), bromine (Br^-), iodine (I^-), or their mixtures). The electrostatic interaction between A-site cations and the BX_6 octahedra largely determines the crystal structure and structural stability of perovskites, which can be predicted by the Goldschmidt tolerance factor (t). The Goldschmidt tolerance factor is an empirical index and can be calculated using ionic radiuses of atoms by Equation (1):

$$t = \frac{r_A + r_X}{\sqrt{2}(r_B + r_X)} \quad (1)$$

where r_A , r_B , and r_X are ionic radiuses of the A-site cation, the B-site cation, and the X-site anion, respectively. In general, hybrid halide perovskites tend to adopt the orthorhombic structure, the cubic structure and the hexagonal structure when the tolerance factor is less than 0.8, within 0.8–1 and greater than 1, respectively.^[31] Experimental results indicate that perovskites within $0.85 < t < 1$ could achieve a stable perovskite phase.^[32] The value of tolerance factors of common perovskites is

calculated and summarized in Figure 2b, suggesting the stable perovskite phase for most hybrid halide perovskites but except for CsSnI_3 , CsPbI_3 , and FAPbI_3 . Notably, extensively investigated Pb-based perovskites exhibit the strong absorption mainly in the visible range determined by their optical bandgap of $\approx 1.55 \text{ eV}$, which indicates their failure in NIR absorption and photodetection.^[39,40,42,46]

To employ the excellent photoelectric properties of perovskites and simultaneously expand the absorption to the NIR range, various narrow-bandgap semiconductors have been incorporated to Pb-based perovskite PDs. Narrow-bandgap materials, such as, inorganic QDs (e.g., PbS , CuInSe_2 , PbSe , etc.),^[47–49] polymers (e.g., poly(diketopyrrolopyrrole-terthiophene) (PDPP3T), poly[2,5-bis(2-hexyldecyl)-2,5-dihydropyrrolo[3,4-c]pyrrole-1,4-dione-3,6-di(5-thiophen-2-yl)yl-alt-N-(2-ethylhexyl)-dithieno[3,2-b:2',3'-d]pyrrole-2,6-diyl] (PDPPDTPT), diketopyrrolopyrrole-dithienylthieno[3,2-b]thiophene (DPP-DTT), etc.),^[50–52] small molecules (e.g., 2-[2-(2-chloro-3-[2-(1,3-dihydro-3,3-dimethyl-1-ethyl-2H-benz[e]indol-2-ylidene) ethylidene]-1-cyclohexen-1-yl)-ethenyl]-3,3-dimethyl-1-ethyl-1H-benz[e]indolium hexafluoro-phosphate (CyPF_6), and 1-butyl-2-(2-[3-(2-(1-butyl-1H-benzo[cd]indol-2-ylidene)-ethylidene)-2-diphenylaminocyclopent-1-enyl]-vinyl)-benzo[cd]indolium tetrafluoroborate (Cy1BF_4)),^[53] and upconversion nanocrystals (e.g., $\text{NaYF}_4:\text{Yb}/\text{Er}$),^[54] have been effectively introduced. Generally, these devices exhibit the relatively low performance in the NIR range due to the weak NIR absorption and/or inefficient photogenerated carrier extraction induced by the poor energy-level alignment at the interface of Pb-based perovskites/narrow-bandgap materials. Meanwhile, NIR materials might influence the crystallization of perovskites, and potentially increase the production complexity and costs.^[47,53] Alternatively, Sn–Pb mixed perovskites, partial incorporation of Sn into Pb-based perovskites,

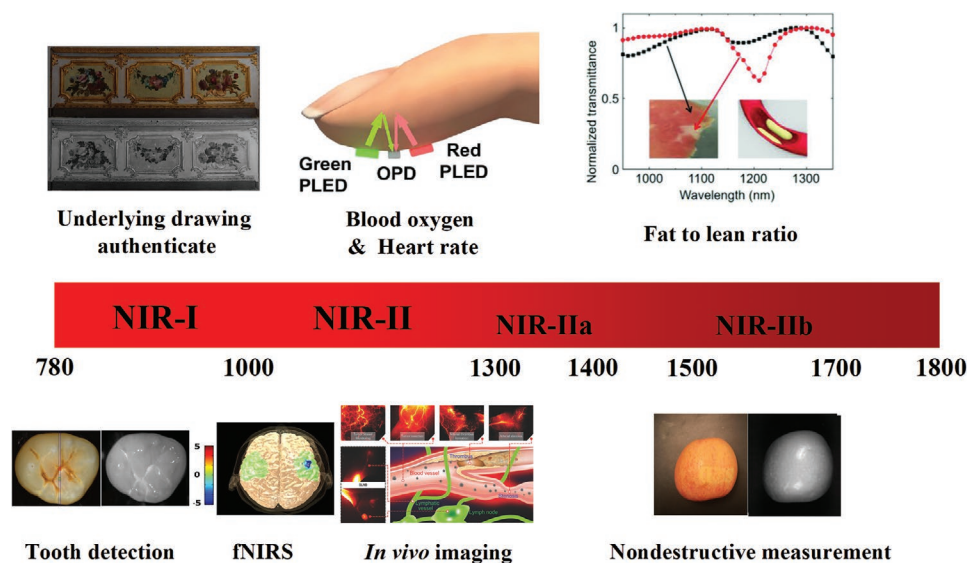


Figure 1. Promising applications of NIR PDs from NIR-I (700–1000 nm) to NIR-II (1000–1800 nm) spectral regions, including tooth detection (Reproduced with permission.^[6] Copyright 2019, Society of Photo-Optical Instrumentation Engineers), underlying drawing authenticate (Reproduced with permission.^[7] Copyright 2020, Springer Nature), fNIRS (Reproduced with permission.^[8] Copyright 2014, Elsevier Inc.), blood oxygen and heart rate measurement (Reproduced with permission.^[9] Copyright 2016, American Association for the Advancement of Science), in vivo biomedical imaging (Reproduced with permission.^[10] Copyright 2017, Wiley-VCH), fat to lean ratio (Reproduced with permission.^[11] Copyright 2018, Wiley-VCH), nondestructive measurement (Reproduced with permission.^[16] Copyright 2019, Elsevier B.V.).

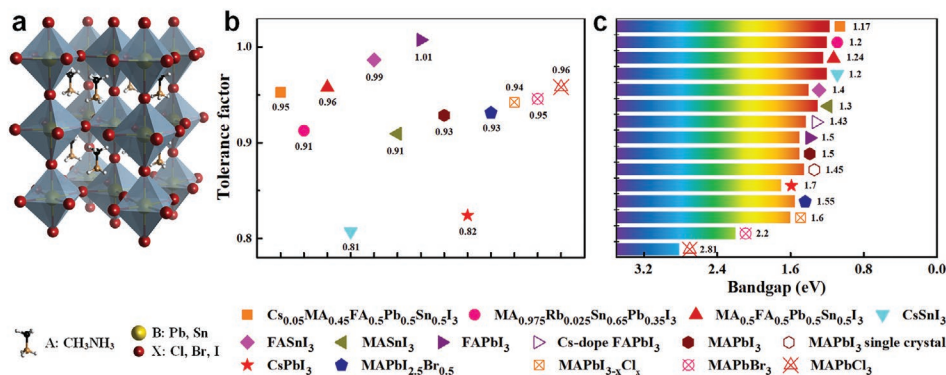


Figure 2. a) The typical tetragonal structure of perovskites (P4mm) in the pseudo-cubic space group, with A cations (e.g., CH₃NH₃⁺) occupying the lattice corners, B cations (e.g., Pb and Sn) occupying the interstitial site, and X anions (halogen anions) occupying the lattice faces. b) Tolerance factors and c) bandgaps of typical perovskites, with Cs_{0.05}MA_{0.45}FA_{0.5}Pb_{0.5}Sn_{0.5}I₃ of 0.95 and 1.17 eV,^[33] MA_{0.975}Rb_{0.025}Sn_{0.65}Pb_{0.35}I₃ of 0.91 and 1.2 eV,^[25] MA_{0.5}FA_{0.5}Pb_{0.5}Sn_{0.5}I₃ of 0.96 and 1.24 eV,^[34] CsSnI₃ of 0.81 and 1.2 eV,^[35] FASnI₃ of 0.99 and 1.4 eV,^[36] MASnI₃ of 0.91 and 1.3 eV,^[37] Cs-doped FAPbI₃ of 1.01 and 1.43 eV,^[38] FAPbI₃ of 1.01 and 1.5 eV,^[39] MAPbI₃ of 0.93 and 1.5 eV,^[40] MAPbI₃ single crystal of 0.93 and 1.45 eV,^[41] CsPbI₃ QDs of 0.82 and 1.7 eV,^[42] MAPbI_{2.5}Br_{0.5} of 0.93 and 1.55 eV,^[43] MAPbI_{3-x}Cl_x of 0.94 and 1.6 eV,^[44] MAPbBr₃ single crystal of 0.95 and 2.2 eV,^[45] and MAPbCl₃ single crystal of 0.96 and 2.81 eV, respectively.^[46]

could achieve the tunable bandgaps from ≈ 2.88 to ≈ 1.17 eV, which show the absorption onset at 1060 nm and thus potentially act as the NIR photoactive material.^[55,115] The bandgaps and tolerance factors of common Pb-, Sn-, and Sn–Pb-based perovskites are summarized in Figure 2c,b, respectively. Notably, easy oxidation of Sn²⁺ to Sn⁴⁺ states in Sn- and Sn–Pb-based perovskites could cause p-type self-doping. It would turn semiconducting features into metal-like ones, which result in the reduced diffusion length, poor device performance, and stability.^[19] Some strategies of inhibiting Sn²⁺ oxidation, including SnF₂, SnF₂-pyrazine complex, hydroxybenzene sulfonic acid, metallic tin powders, and formamidinesulfonic acid, have been demonstrated and improved the carrier diffusion length of Sn-contained perovskites.^[56–59] Consequently, low-temperature and solution-processed Pb-, Sn-, and Sn–Pb-based perovskites with remarkable photoelectric properties can be a promising alternative to inorganic semiconductors for NIR PDs and imaging arrays.

Currently, there have been several reviews on Pb-based perovskite UV–vis PDs.^[60–62] Narrow-bandgap Sn- and Sn–Pb-based perovskites have been intensively studied and applied in single-junction solar cells and tandems.^[63–66] Distinctively, in this Review, we focus on recent advances in NIR photo-detection and imaging applications of hybrid halide perovskites from the perspective of both materials and devices. Specifically, Section 2 introduces the formation and optoelectronic properties of hybrid halide perovskites, followed by the introduction of detection mechanisms and figures of merit of perovskite-based NIR devices in Section 3. In Section 4, we discuss the NIR spectral response extension of Pb-based perovskite single crystals/polycrystalline films incorporated with various narrow-bandgap NIR materials, including inorganic QDs,^[40,47] small molecules/polymers,^[50,53] up-conversion nanocrystals,^[54,67] etc. Sections 5 and 6 cover the latest progress of Sn-based and Sn–Pb-based perovskite NIR devices, respectively. Finally, we will propose the outlook on hybrid halide perovskite-based NIR PDs and imaging arrays, and summarize this review.

2. Formation and Optoelectronic Properties of Perovskites

High-quality photoactive semiconductors (i.e., low trap concentrations, long carrier lifetimes, high carrier mobilities, etc.) will give rise to high-performance PDs. Numerous methods have been adopted to fabricate high-quality perovskites with various morphologies, such as bulk single crystals, single-crystalline thin films, nanowires, nanocrystals, polycrystalline thin films, etc. In the following of this section, some typical crystal growth methods of perovskites and their unique optoelectronic properties will be briefly discussed.

2.1. Formation of Perovskites

2.1.1. Bulk Single Crystals

Hybrid halide perovskite single crystals, which possess ultralow trap densities, long carrier lifetime, and diffusion length, have been widely explored their applications in PDs, solar cells, light emitting diodes, lasers, etc.^[18,22,32,60,71–75] The prospects of these applications drives numbers of researchers to adopt various methods to grow perovskite single crystals, such as inverse temperature crystallization (ITC),^[68,76] antisolvent vapor-assisted crystallization,^[69] room-temperature liquid diffused separation induced crystallization,^[77] the space-confined solution-processed strategy,^[78] top-seeded solution growth,^[71] etc. The crystallization process diagram of ITC and antisolvent vapor-assisted crystallization are depicted in **Figure 3a,b**, respectively. Specifically, based on the retrograde solubility of perovskites at a high temperature in certain solvents (e.g., gamma-butyrolactone (GBL), dimethyl sulfoxide (DMSO), *N,N*-dimethylformamide (DMF), or their mixtures), ITC (Figure 3a) exhibits manifest merits in fast, large-scale, and high-quality crystallization, and thus ITC has been widely adopted in growing perovskite single crystals. Osman M. Bakr and

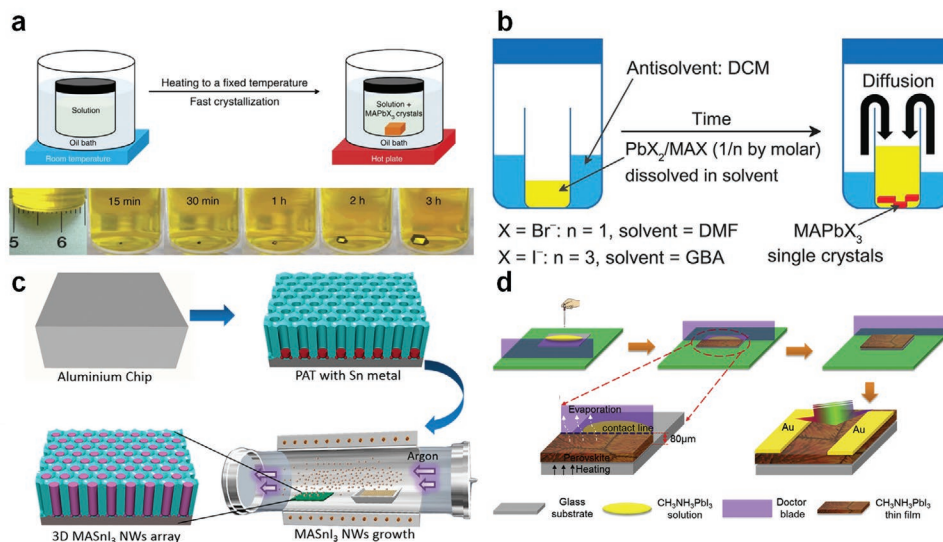


Figure 3. Typical growth methods for perovskites. a) Inverse temperature crystallization. b) Antisolvent vapor-assisted crystallization. c) Vapor synthesis. d) Doctor-blade coating. a) Reproduced with permission.^[68] Copyright 2015, Nature Publishing Group. b) Reproduced with permission.^[69] Copyright 2015, American Association for the Advancement of Science. c) Reproduced with permission.^[37] Copyright 2016, American Chemical Society. d) Reproduced with permission.^[70] Copyright 2017, Elsevier B.V.

co-workers found that the retrograde solubility of FAPbI_3 in GBL and FAPbBr_3 in 1:1 v/v DMF:GBL, in which they studied the temperature-dependent solubility curves of hybrid perovskites with various compositions in different solvents through the ITC strategy.^[76] MAPbX_3 perovskite single crystals have also been demonstrated by ITC and exhibited the outstanding crystallization speed and quality.^[68,79] Furthermore, to improve the crystal quality, various revised methods have been adopted in ITC, among which precisely controlling the crystallization temperature and appropriate selection of the solvent are pretty crucial.^[76,80] In the method of antisolvent vapor-assisted crystallization (Figure 3b), a perovskite-precursor-insoluble antisolvent diffuses and then initiates the crystallization of perovskites dissolved in a highly-soluble solvent.^[69] The high yield and practicability of this method have been extensively deployed to produce perovskite single crystals,^[68,81,82] but the difficulty in growing large grain sizes and time-consuming processes limit its wider applications. Recently, room-temperature liquid diffusion induced crystallization developed by Guojia Fang, Qianqian Lin, Chen Tao, and co-workers was proposed to produce high-quality perovskite single crystals at low temperatures.^[77] Since the density of silicone oil is slightly higher than that of solvents but lower than that of perovskite precursors, silicone oil is selected to extract solvents from the precursor solution, which lead to the oversaturated precursor solution and thus induce the crystallization of MAPbX_3 . It exhibits a high yield up to $\approx 92\%$ and better optoelectronic performance than MAPbBr_3 grown in high temperatures.^[77]

2.1.2. Single-Crystalline Thin Films

Monocrystalline perovskite thin films with large surface areas and high aspect ratios potentially show better photoelectric properties and robust environmental stability for some certain

devices based on certain crystallographic planes.^[83] Strategies of surface-tension^[84] or space-confined^[78] assisted crystallization have been successfully applied to grow monocrystalline perovskite thin films, which have been widely applied in the field of photodetection. Based on the mechanism of ITC, surface-tension assisted crystallization employs the effect of surface tension to induce the nucleation at the solution surface layer. The process of nucleus growing to a crystal continues on the solution surface until it reaches the size when surface tension can no longer remain the crystal afloat.^[84] In the space-confined assisted crystallization, two flat substrates are clipped together to tune the shape and thickness of resultant single-crystalline thin films. The crystallization is induced by the top-seeded solution growth,^[71] where the bottom precursor solution is saturated and the top is supersaturated. Simultaneously, a temperature gradient induces the sufficient convection from bottom to top, and thus results in the continuous growth of monocrystalline thin films.^[78]

2.1.3. Nanowires

Nanowires provide quantum-confined channels for the transport of photogenerated carriers to their respective electrodes. Compared with their thin film counterparts, nanowires potentially possess higher carrier mobilities, longer diffusion length, and excellent mechanical flexibility, which are beneficial for high-efficiency rigid/flexible PDs.^[85–88] Typically, MAPbI_3 nanowires can be facilely constructed through coating PbI_2 layers with an isopropanol solution of MAI in the presence of a small amount of polar aprotic solvents,^[86] or through a dissolution-recrystallization process where perovskite thin films are treated with a mixed solvent of DMF and isopropanol.^[85] Moreover, together with nanoengineering templates, Zhiyong Fan and co-workers introduce a vapor phase chemical reaction method to produce several perovskite nanowires, including MAPbI_3 .^[89]

and MASnI_3 .^[37] Regarding MASnI_3 nanowires, an array of 3D MASnI_3 nanowires in a porous alumina template was achieved by the electrochemical deposition of Sn on the template bottom and subsequent vapor diffusion of MAI under the argon protection at 170 °C, as illustrated in Figure 3c. In addition, nanochannel-confined growth strategies have been successfully introduced to tune the orientation and dimensions of perovskite nanowire arrays, which largely influence the charge transport behavior, and thus determine the performance of PDs.^[87,90]

2.1.4. Polycrystalline Thin Films

Due to remarkable advantages of simple-processability, energy-efficiency, low-cost, and high-throughput production, perovskite polycrystalline thin films have been widely explored and fabricated by many solution techniques (including spin-coating,^[91] doctor-blade coating,^[70,92] roll-to-roll coating,^[93] inkjet printing,^[94] spray coating,^[95] slot-die coating,^[96] etc.) for lab-scale or industrial-scale optoelectronic devices. Typical solution-processed approaches for perovskite polycrystalline thin films include the one-step method that direct spin-coat perovskite precursors on substrates followed by the annealing treatment,^[97–98] the antisolvent washing that enable a nonpolar antisolvent (e.g., diethyl ether, toluene, chlorobenzene, etc.) drip on spin-coated perovskite precursor films to accelerate their supersaturation and induce the rapid crystallization,^[99,100] and the two-step method that first deposit lead/tin halide precursor layers on substrates subsequently treated by organic salts.^[101–103] Regarding narrow-bandgap Sn–Pb mixed perovskites in NIR PDs, their polycrystalline thin films particularly suffer from the uncontrollable nucleation and fast crystallization between SnI_2 films and organic salts.^[104] The crystallization process could be retarded due to the intermediate phases formed through the interaction of DMSO molecules with SnI_2 .^[27] Additionally, to tune the crystallization of Sn–Pb mixed perovskites, various approaches have been studied including additive enhanced crystallization,^[10,105–109] the hot-casting method,^[110] alloying engineering of two perovskite precursors (FASnI_3 and MAPbI_3 , FAPbI_3 and CsSnI_3),^[111,112] the vacuum-assisted annealing method,^[113] and functionalized carrier-extraction layer assisted crystallization.^[114] Among them, additive enhanced crystallization has been extensively explored to control the crystallinity and the orientation of Sn–Pb mixed perovskite polycrystalline films. The additives are chloride, cesium, rubidium, C_{60} , metallic tin, guanidinium thiocyanate, etc.

Compared with widely-used spin-coating for lab-scale polycrystalline thin films, scalable doctor-blade coating was proposed to adopt a scraper to linearly swipe over the perovskite precursor solution on desirable substrates at a certain speed. The flow chart of doctor-blade coating is depicted in Figure 3d. The waste of raw materials in spin-coating processes could be effectively reduced and the thickness of perovskite films could be precisely controlled by changing the concentration of the precursor solution and the gap between the blade and the substrate.^[70,92] In addition, the doctor-blade coating can be matched with roll-to-roll coating in large-scale and industrial production for flexible devices. However, both doctor-blade coating and roll-to-roll coating exhibit the difficulty in fabricating high-quality

perovskite polycrystalline films as the spin-coating method presents the difficulty in uniform nucleation and controllable crystallization for large-scale films. Methods of inkjet printing, spray coating and slot-die coating are also generally adopted to produce large-scale perovskite polycrystalline films, however, the quality of perovskite films prepared by these methods is still inferior to that of films by traditional methods.^[94–96]

2.2. Optoelectronic Properties of Perovskites

It is critical to separate electron-hole pairs, transport free carriers, and ultimately collect these carriers by respective electrodes after the active layer of perovskite-based PDs absorbing the incident light and generating electron-hole pairs. With excellent optoelectronic properties, such as high optical absorption coefficient of $\approx 10^5 \text{ cm}^{-1}$, low trap densities ($\approx 10^{15} \text{ cm}^{-3}$ for polycrystalline films, $\approx 10^9 \text{ cm}^{-3}$ for single crystals), high carrier mobility of tens to hundreds ($\text{cm}^2 \text{ V}^{-1} \text{ s}^{-1}$), long carrier lifetimes at microsecond scale, and long carrier diffusion lengths at micrometer scale, perovskites are compelling active materials in photoelectric devices.^[69,71,116,119–127] A brief review on optoelectronic properties of perovskites is provided and summarized in **Table 1** for readers to keep a rough impression and better understand their wide applications described in the rest of this review.

2.2.1. High Optical Absorption Coefficient

The absorption coefficient presents the degree to which the incident light could penetrate the desirable material before it is absorbed. Hence, the higher absorption coefficient allows the thinner thickness of active layers in PDs for sufficient light absorption. Silicon shows the weak NIR absorption and has the low absorption coefficient of around 100 cm^{-1} at 940 nm wavelength.^[128,129] Interestingly, perovskites are direct bandgap semiconductors and typically exhibit a high optical absorption coefficient of approaching 10^5 cm^{-1} in the visible wavelength range (for Pb-based perovskites).^[130,131] Narrow-bandgap Sn–Pb mixed perovskites achieve the NIR absorption extension with respect to Pb-based perovskites and notably have a high absorption coefficient of $\approx 10^4 \text{ cm}^{-1}$ at 940 nm wavelength, which is near two orders of magnitude greater than silicon.^[125,126] The remarkable optical properties can be related to direct and isotropic optical transitions between a triply degenerated conduction-band and a single valence-band in a simple group representation, that is, the high joint density of state of conduction-band states and valence-band states.^[132–134] Apart from the direct band-to-band transition caused by the incident light, photon recycling can increase the level of optical absorption in perovskite-based devices (such as, PDs and solar cells), in which photons generated by radiative recombination of electrons with holes will be partially reabsorbed by perovskites.^[130,131,135]

2.2.2. Low Trap Density and High Defect Tolerance

Defects, especially intrinsic point defects in perovskites (e.g., V_{MA} , V_{Pb} , MA_i , I_{Pb} , Pb_i , etc.), could induce two distinctive trap

Table 1. Optoelectronic properties of perovskites and their corresponding test methods.

Properties	Value	Test methods	Physical definition	Ref.
Bandgap	≈1.17–2.88 eV	UV–vis diffuse reflectance spectroscopy Photoluminescence spectroscopy	The energy required to excite a valence electron to become a conduction electron.	[18,26,55,115]
Exciton binding energy	≈10–25 meV	Magneto absorption spectroscopy	The energy required to dissociate photogenerated electron-hole pairs to produce free carriers.	[116–118]
Trap density	≈10 ¹⁴ –10 ¹⁷ cm ⁻³ for polycrystalline films, ≈10 ⁹ –10 ¹¹ cm ⁻³ for single crystals	Space charge limit current Thermal admittance spectroscopy	Trap density is number of traps located in the forbidden band of a semiconductor per unit volume.	[24,69,71,119,120]
Carrier lifetime	≈1–10 μs	Time-resolved photoluminescence Time-resolved microwave conductance	The average time it takes an excess minority carrier to recombine.	[121,122]
Carrier mobility	≈10–10 ³ cm ² V ⁻¹ s ⁻¹	Hall effect analyzer Terahertz spectroscopy Space charge limit current	Carrier mobility is the drift velocity attained by a charge carrier per unit of applied electric field.	[19,71,123,124]
Carrier diffusion length	≈1–100 μm		The average distance that a charge carrier moves between generation and recombination.	[69,71,121]
Optical absorption coefficient	Approaching 10 ⁵ cm ⁻¹ in the visible spectrum	Photothermal deflection spectroscopy Spectrally resolved photoluminescence	The degree to which the incident light could penetrate a material before it is absorbed.	[125–127]
Urbach energy	15 meV for MAPbI ₃ , 33 meV for Sn–Pb mixed perovskites	Photothermal deflection spectroscopy	An indicator of the energetic disorder in crystal structures.	[75,110,126]

states, that is, shallow traps and deep traps. These traps generally exit in surfaces/boundaries of perovskite polycrystalline films and would present two opposite effects on the photoelectric performance of perovskite devices.^[136–138] Shallow traps can provide a certain number of free carriers for the current circulation (i.e., enhanced photocurrent of PDs) and even contribute to the NIR photodetection for MAPbI₃.^[70,139,140] Distinctively, deep traps cause non-radiative recombination and thereby decrease the photoelectric performance of devices. According to first-principles density-functional theory (DFT) calculations, shallow traps, including MA_i, V_{Pb}, MA_{Pb}, I_i, V_I, and V_{MA}, own the low formation energy and have the value of transition energy less than 50 meV below (above) conduction band minimum (valence band maximum). Deep traps, such as I_{Pb}, I_{MA}, Pb_i, and Pb_V, possess the relatively high formation energy and potentially cause Shockley–Read–Hall non-radiative recombination. Hence, defects in perovskite films prefer to generate shallow-level trap states.^[69,71,134,141] Such unusual defect properties could be attributed to the strong antibonding coupling between Pb lone-pair *s* orbital and I *p* orbital of MAPbI₃.^[141] Moreover, ionic perovskites tend to form large polarons induced by the long-range Coulomb potential between the excess electron (hole) and the ionic lattice. Large polarons can provide the effect of Coulomb screening and thus reduce the scattering of carriers, contributing to the low recombination rate and defect tolerance.^[142–145] Concerning narrow-bandgap Sn–Pb mixed perovskites, the incorporation of Sn does not introduce a mid-gap state and thus avoid trap states at both low and high Sn contents. Sn–Pb mixed perovskites could transfer small polarons for the low Sn content to large polarons for the high Sn content (greater than 25%). Notably, compared with Pb-based perovskites, Sn–Pb mixed perovskites decrease

nonadiabatic electron-phonon coupling, which reduces the non-radiative recombination and increases excited-state lifetime.^[146,147] Experimentally, the energetic disordered crystal structure can induce defect states near the band edge, which can be characterized by Urbach energy.^[148] Perovskites have a steep absorption spectrum below the band edge, and achieve the Urbach energy of 15 meV for MAPbI₃ and 33 meV for Sn–Pb mixed perovskites, which is compared with that of 11 meV for crystalline silicon, indicating low localized defect levels within the bandgap.^[75,110,126]

2.2.3. Remarkable Carrier Transport Properties

Electronic structure calculations of typical lead halide perovskites exhibit the strong spin-orbit coupling (i.e., a relativistic coupling between electronic spin and orbital momentum) of 6p orbital in heavy Pb atom and thus cause the large dispersion for both valence and conduction bands that have recently been experimentally observed.^[132,149–152] The large dispersion would contribute to small effective masses of photogenerated electrons and holes of 0.1–0.2 *m_e* (*m_e* is the bare-electron mass), suggesting the ambipolar transport property and high carrier mobility.^[117,149,153,154] Employing noncontact terahertz conductivity measurements, the combined electron and hole mobility of typical MAPbI₃ at room temperature is 59 cm² V⁻¹ s⁻¹ for single crystals and 33 cm² V⁻¹ s⁻¹ for polycrystalline thin films. The room-temperature mobility is dominated by Fröhlich scattering of charge carriers with multiple phonon modes, the slight reduced mobility for polycrystalline films is primarily limited by the grain-boundary scattering.^[124] Furthermore, reduced electron and hole effective masses will result in the

small exciton binding energy, which is an indicator of energy to dissociate photogenerated electron-hole pairs. The experimental value of exciton binding energy of typical MAPbI₃ is only 16 meV in low temperatures and reduce to a few meV at room temperature.^[117,118] The small value indicates the spontaneous generation of free electrons and holes following the photo-absorption, which is beneficial to the carrier extraction for efficient PDs. Benefiting from the low trap density and high carrier mobility, the diffusion length of perovskites single crystals, defined by the average distance a charge carrier moves between generation and recombination, was estimated to be several μm and even up to 100 μm.^[69,71,124] Importantly, the diffusion length for polycrystalline thin films was greater than 1 μm, which is thicker than the active layer of typical perovskite-based PDs and thus guarantee the efficient carrier extraction.^[124,155]

3. Fundamentals of Perovskite-Based Near-Infrared Detection

According to device structures related with different photo-detection mechanisms, PDs can be generally divided into photoconductors, photodiodes, and phototransistors. Their device architectures and working mechanisms are summarized in Table 2. In order to realize NIR detection of perovskites, some strategies including interband/intraband response, sub-bandgap response, and indirect response are introduced and discussed in detail below.

3.1. Near-Infrared Detection Mechanisms of Perovskites

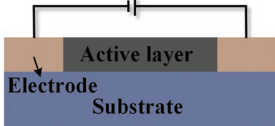
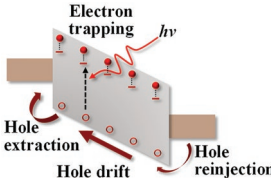
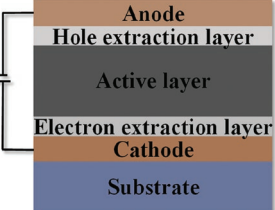
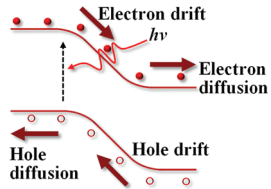
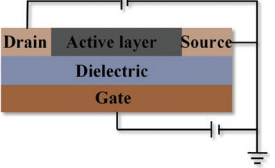
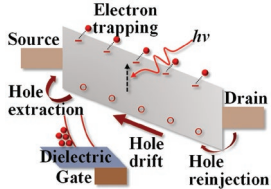
3.1.1. Interband/Intraband Response

Pb-based perovskites possess the lowest bandgap of around 1.5 eV, which absorb a tiny fraction of NIR signals. To realize the response at longer wavelengths, the excited electrons could undergo the intraband transition, which provides the possibility of NIR response for perovskites (Figure 4).^[156] Further, an effective way to narrow the bandgap of perovskites has been proved to employ ion substitution, for example, replacing chloride and bromide anions with larger iodide anions, and substituting lead cations with smaller tin cations (down to 1.17 eV for Cs_{0.05}MA_{0.45}FA_{0.5}Pb_{0.5}Sn_{0.5}I₃).^[33,157] Beneficially, A-site cation compositional engineering could also moderately tune the bandgap through controlling the competing of octahedral tilting and lattice contraction.^[158]

3.1.2. Sub-Bandgap Response

In addition to interband/intraband transition, sub-bandgap absorption including third-order nonlinear two-photon absorption and trap state absorption also contributes to the NIR response of perovskites-based devices (Figure 4). Two-photon absorption states that perovskites can simultaneously absorb two photons with the half energy of their bandgap. With the two-photon absorption, the spectral response onset of MAPb_{0.75}Sn_{0.25}I₃ can reach 1.8 μm with respect to its absorption

Table 2. Device architectures and working mechanisms of perovskite-based NIR PDs.

Device architectures	Working mechanisms	Principles of photocurrent extraction
<p>Photoconductors</p> 		<p>Under illumination, the inevitable charge traps within semiconductors would localize one type of the photogenerated carriers, while the opposite type of carriers generated by an external voltage would circulate many times in the circuit before recombination, resulting in the gain.</p>
<p>Photodiodes</p> 		<p>The significant difference in work functions between carrier-selective extraction layers/active layers produces a built-in potential to assist the separation of photogenerated carriers after the excitation process. Separated electrons/holes drift in different directions toward cathode/anode electrodes driven by the built-in potential, which further diffuse to selective contacts.</p>
<p>Phototransistors</p> 		<p>Under illumination, photogenerated electron-hole pairs will be extracted to corresponding electrodes by the drain-source electrical field. The gate voltage can effectively separate the carriers by the capacitive coupling and then increase their recombination time. Charge traps located in the bulk or surfaces of channel semiconductors contribute to the photoconductive gain.</p>

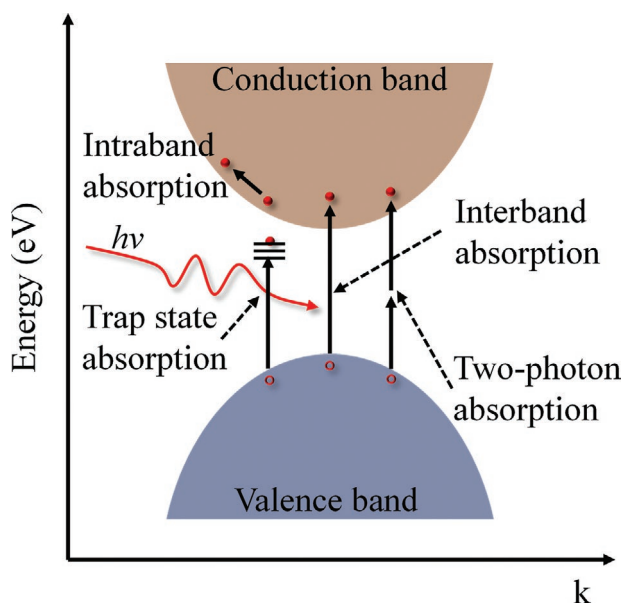


Figure 4. Schematic diagram of perovskite-based NIR detection, including interband absorption, intraband absorption, trap state absorption, and two-photon absorption.

onset at 912 nm wavelength.^[159] Typically, perovskite-based NIR devices with the two-photon absorption need ultrahigh intensities of incident light, high working voltages, and achieve the low responsivity.^[160–162] Differently, trap state absorption does not need the high-photon flux irradiation. NIR response induced by trap state absorption typically occurs in perovskite single crystal-based devices rather than polycrystalline film-based devices due to their minimized grain boundaries, which promise a lower carriers combination rate and higher carriers collection efficiency. Besides, trap state absorption also can be utilized in charge collection narrowing strategy to achieve filterless narrowband PDs.^[163]

3.1.3. Indirect Response

Incorporating narrow-bandgap materials (e.g., inorganic QDs,^[40,47,184,189,192] polymers,^[50–52,202] small molecules,^[53,185,190] upconversion nanocrystals,^[54,164] etc.) with Pb-based perovskites has been an effective and widely-used method to achieve NIR detection. The key point of realizing efficient indirect NIR response are the band alignment, interface defect passivation, and high-quality perovskites. Typically, the energy-level alignment at the interface of perovskite/narrow-bandgap semiconductors should facilitate the extraction of photogenerated carriers within active layers, contributing to the high responsivity.

3.2. Figures of Merit

To quantitatively describe and compare the overall performance of diverse PDs, it is crucial to define some common indicators for evaluating these devices. Generally, they are responsivity, EQE, gain, noise current, noise equivalent power (NEP), linear

dynamic range (LDR), specific detectivity (D^*), response speed, and -3 dB bandwidth. The definition of these parameters is summarized in Table 3.

4. Pb Perovskite-Based Near-Infrared Photodetectors and Imaging Arrays

The NIR detection and imaging using Pb perovskites have been realized through sub-bandgap absorption or intraband transition of Pb-based perovskites. In addition, incorporated narrow-bandgap semiconductors with Pb perovskites (including silicon, CuO, transition-metal dichalcogenides (TMDs), inorganic QDs, organic semiconductors, and upconversion nanocrystals) have been demonstrated to present NIR photodetection. We will discuss the current progress of Pb perovskite-based NIR PDs and imaging arrays below and summarize the advancements in Table 4.

4.1. Pb Perovskite Single Crystals for Near-Infrared Photodetection

With the assistance of trap state absorption, perovskite bulk single crystals exhibit a certain degree of NIR detection capability.^[45,69,71,198] Paul Burn, Paul Meredith, and co-workers employed the NIR absorption of surface trap states and fabricated NIR PDs using millimeter-sized MAPbBr₃ (8 mm × 8 mm × 3 mm) and MAPbI₃ (10 mm × 8 mm × 3 mm) single crystals grown by ITC.^[45] Thick photodiodes sandwiched between Al and Au electrodes were first demonstrated and achieved the NIR response of 1064 nm wavelength with the incident light intensity of ≈ 10 mW cm⁻², corresponding to the relatively low responsivity of 10^{-5} A W⁻¹. This phenomenon that perovskite photodiodes are sensitive to NIR photons far below the bandgap of MAPbI₃ single crystals was attributed to the absorption by sub-gap states derived from surface trap states of active layers, given that the bulk has relatively lower trap densities in perovskites. To effectively employ the NIR absorption of surface trap states and thus enhance the NIR photocurrent response, planar photoresistors with interdigitated electrodes (similar to the structure of photoconductors) onto the surface of MAPbI₃ single crystals were demonstrated as shown in Figure 5a. Photoresistors could achieve the NIR response down to 900 nm wavelength at the relatively low incident light intensity of 0.2 mW cm⁻² (Figure 5b,c).

Shengzhong (Frank) Liu, Zhou Yang, and co-workers employed ITC to prepare large MAPbI₃ single crystals with the length of 80 mm, which exhibit a narrow bandgap of 1.45 eV, the low trap density of 2.1×10^9 cm⁻³, and a high carrier mobility of 67.27 cm² V⁻¹ s⁻¹.^[44] They further investigated their applications in the mass production of integrating PDs by slicing bulk crystals into wafers^[199] and subsequently depositing Au electrode arrays on wafer surfaces, as presented in Figure 5d. The integrated photoconductors show a broad spectral response to around 900 nm wavelength and achieve a rise time of 39 μ s and a fall time of 1.9 μ s, as displayed in Figure 5e. Besides, the photocurrent of unencapsulated PDs remain stable under the continuous illumination for ≈ 37 min at the ambient air with a humidity level of $\approx 50\%$. It remains

Table 3. Figures of merit, formula, and their definition of PDs.

Parameters	Formula	Unit	Definition
Responsivity	$R_\lambda = \frac{I_p - I_d}{P_\lambda}$ where I_p is the photocurrent measured under illumination, I_d is the dark current measured in dark, and P_λ is the intensity of the incident light with a wavelength of λ .	A W ⁻¹	The ratio of the net current increment to the incident light intensity at a specific wavelength.
EQE	$\text{EQE}_\lambda = \frac{(I_p - I_d)/e}{P_\lambda/h\nu} = R_\lambda \frac{hc}{e\lambda}$ where e is the elementary charge, h is the Planck constant, ν and λ are the frequency and wavelength of the incident light.	%	The ratio of the average extracted electron number over the incident photon number per unit time at a specific wavelength.
Gain	$G_\lambda = \frac{\tau_{it}}{\tau_{tt}} = \frac{\tau_{it}}{d^2/\mu V}$ where τ_{it} and τ_{tt} represent the carrier lifetime and the transit time, respectively. The parameters of d , μ , and V are the thickness of the active layer or the channel length, the carrier mobility and the applied voltage, respectively.		The number of collected carriers divided by the number of absorbed photons.
Noise current	$I_{\text{noise}} = \sqrt{I_{th}^2 + I_{sh}^2 + I_{1/f}^2 + I_{gr}^2}$ where I_{th} , I_{sh} , $I_{1/f}$, I_{gr} represent thermal noise, shot noise, flicker noise, and generation-recombination noise, respectively.	A Hz ^{-1/2}	Thermal noise arises from the thermal agitation of electrons. Shot noise is caused by the random excitation and capture of generated carriers. Flicker noise is a frequency-dependent conductance fluctuation. Generation-recombination noise originates from the fluctuation in free carrier densities because of generation and recombination processes.
NEP	$\text{NEP}_\lambda = \frac{I_{\text{noise}}}{R_\lambda}$	W Hz ^{-1/2}	The ratio of the total noise current over the responsivity in units of W Hz ^{-1/2} .
LDR	$\text{LDR} = 20(10) \times \log \frac{P_{\text{sat}}}{P_{\text{noise}}}$ where P_{sat} is the maximum linearly incident light intensity. P_{noise} is the lowest linearly detectable light intensity governed by the total noise current.	dB	The range of light intensities where the photocurrent density of PDs is linearly proportional to the incident light intensity.
Specific detectivity	$D_\lambda^* = \frac{\sqrt{A}}{\text{NEP}_\lambda} = \frac{R_\lambda \sqrt{A}}{I_{\text{noise}}}$ where A is the photoactive area of PDs.	Jones (cm Hz ^{1/2} W ⁻¹)	A performance parameter for comparison of PDs with different areas.
Response speed		s	Rise time and fall time are defined as the time taken by photocurrent to rise from 10% to 90%, or fall from 90% to 10% of its stable value, respectively.
-3 dB bandwidth	$f_{-3\text{dB}}^2 = f_t^2 + f_{\text{RC}}^2$ where f_t is the carrier transit time limited bandwidth and f_{RC} is the RC limited bandwidth.	Hz	The frequency of the incident light at which the photocurrent is half of its maximum value.

92.5% after 10 days storage and 88% after 20 days storage under the ambient atmospheric condition, as depicted in Figure 5f. Importantly, the integration of PDs on perovskite monocrystalline wafers indicates a potential application in the field of integrated circuits.

4.2. Pb Perovskite Polycrystalline Films for Near-Infrared Photodetection

Intraband transitions contribute to the NIR photocurrent response of polycrystalline perovskite-based PDs. Iman Roqan

and co-workers employed the intraband transition in MAPbI₃ perovskites to present a broad spectral response with the wavelength region of 250–1357 nm.^[156] Vertical-structured Gd-doped ZnO nanorods/MAPbI₃ heterojunction PDs (Figure 6a) were fabricated by first depositing an array of Gd-doped ZnO nanorods (450 nm length and 60–85 nm diameter) on a stainless steel substrate by pulsed laser deposition, and subsequently spray-coating a 1500 nm thick MAPbI₃ perovskite layer to completely cover the ZnO nanorods array. The excellent energy-level match between the metal substrate and the conduction band of Gd-doped ZnO nanorods, together with the type-II band alignment at the interface of Gd-doped ZnO nanorods/MAPbI₃

Table 4. Figures of merit and current progress of Pb perovskite-based NIR devices.

Photoactive materials	Spectral range [nm]	Responsivity [mA W ⁻¹]	Specific detectivity [Jones]	EQE	f_{-3dB} [kHz]	LDR [dB]	t_{rise}/t_{fall} [μs]	Ref.
Photodiodes								
MAPbI ₃ /Gd-doped ZnO nanorods	250–1357	220 @ 1357 nm	9.3 × 10 ⁹ @ 1357 nm ^{a)}	–	–	–	4 × 10 ⁵ /5 × 10 ⁵	[156]
PVP-modified MAPbI ₃ Cl _{3-x} /Si	405–988	≈1250 @ 988 nm	≈5.3 × 10 ¹¹ @ 808 nm ^{a)}	≈275% @ 808 nm	–	44 ^{c)}	645/560	[165]
Cs-doped FAPbI ₃ /Si nanowire array	300–1200	14.86 @ 850 nm	2.04 × 10 ¹⁰ @ 850 nm ^{a)}	–	7.5	–	4/8	[38]
MAPbI ₃ /CuO nanowires	350–1050	562.9 @ 800 nm 7.3 @ 1000 nm	2.15 × 10 ¹³ @ 800 nm 2.91 × 10 ¹¹ @ 1000 nm ^{a)}	–	–	–	<2 × 10 ⁵ / <2 × 10 ⁵	[166]
FA _{0.85} Cs _{0.15} PbI ₃ /PtSe ₂	300–1200	117.7 @ 808 nm	2.91 × 10 ¹² @ 808 nm ^{b)}	14.9% @ 808 nm	≈2 × 10 ³	–	0.078/0.060	[167]
MAPbI ₃ Cl _{3-x} /Si	300–1150	870 @ 800 nm	6 × 10 ¹² @ 800 nm ^{a)}	–	–	–	5 × 10 ⁴ /1.5 × 10 ⁵	[168]
FA _{0.85} Cs _{0.15} PbI ₃ /PtSe ₂	200–1550	313 @ 808 nm	2.72 × 10 ¹³ @ 808 nm ^{a)}	≈50% @ 808 nm	≈20.1	–	3.5/4	[169]
Si/MAPbI ₃	300–1150	50.9 @ 815 nm	2.23 × 10 ¹² @ 815 nm ^{a)}	<10%	–	–	1.3 × 10 ⁴ /1.46 × 10 ⁴	[170]
MAPbI ₃ /PbS QDs layer	375–1100	132 @ 900 nm	5.1 × 10 ¹² @ 900 nm ^{a)}	18.2% @ 900 nm	–	100 ^{d)}	–	[47]
MAPbI ₃ /PbSe QDs layer	300–2600	628 @ 1300 nm 238 @ 2400 nm	1.59 × 10 ¹² @ 1300 nm 6.01 × 10 ¹¹ @ 2400 nm ^{a)}	≈20% @ 1350 nm	–	69 ^{c)}	4/32	[40]
MAPbI ₃ /CuInSe ₂ QDs layer	300–1100	>20 @ 800–1000 nm	7.7 × 10 ¹¹ @ 850 nm ^{b)}	–	241	75.1 ^{c)}	0.277	[48]
FA _{0.83} Cs _{0.17} Pb(I _{0.9} Br _{0.1}) ₃ :CyPF ₆	450–1000	24 @ 850 nm	2 × 10 ⁸ @ 900 nm (CyPF ₆)	–	65 (CyPF ₆)	–	65/74 (CyPF ₆)	[53]
FA _{0.83} Cs _{0.17} Pb(I _{0.9} Br _{0.1}) ₃ :Cy1BF ₄	450–1600	(CyPF ₆)	2 × 10 ⁷ @ 1500 nm ^{b)} (Cy1BF ₄)	–	85 (Cy1BF ₄)	–	–	
MAPbI _{2.5} Br _{0.5} :PbS QDs	400–1400	99 @ 975 nm	4 × 10 ¹² @ 1240 nm ^{b)}	40% @ 1240 nm	60	60 ^{d)}	<10	[43]
MAPbI ₃ :PbS QDs	400–1000	–	3.30 × 10 ¹¹ @ 900 nm ^{a)}	≈6% @ 900 nm	–	–	<5 × 10 ⁵	[171]
MAPbI ₃ /PDPP3T	380–950	≈300 @ 875 nm	≈3 × 10 ¹³ @ 875 nm ^{a)}	≈50%	≈60	112 ^{c)}	4.82/4.30	[172]
MAPbI ₃ /PDPPDTPT	350–1050	–	≈1 × 10 ¹¹ @ 900 nm ^{b)}	10–20% @ 800–950 nm	–	95 ^{d)}	6.1 × 10 ⁻³	[51]
MAPbI ₃ /SWCNTs/NDI-DPP	375–1400	150 @ 1064 nm	2 × 10 ¹² @ 920–940 nm ^{a)}	≈20% @ 920–940 nm	–	>90 ^{d)}	4.32/12.16	[173]
MAPbI ₃ /PTB7-Th/IEICO-4F	340–940	518 @ NIR	>10 ¹⁰ @ 340–940 nm ^{b)}	>70%	–	–	500/510	[174]
MAPbI ₃ /IEICO	300–900	140 @ 820 nm	7.37 × 10 ¹¹ @ 820 nm ^{b)}	30% @ 800–900 nm	–	192 ^{c)}	–/0.027	[175]
MAPbI ₃ /F8IC:PTB7-Th	300–1000	370 @ 870 nm	2.3 × 10 ¹¹ @ 870 nm ^{b)}	54% @ 850 nm	–	191 ^{d)}	35/20	[176]
Si/MAPbBr ₃ single crystal	405–1064	≈5 @ 1064 nm	≈2 × 10 ¹⁰ @ 1064 nm ^{a)}	–	–	–	0.52/2.44	[177]
MAPbI ₃ /Si-NPA	400–1050	8.13 @ 780 nm	9.74 × 10 ¹² @ 780 nm ^{a)}	–	–	–	253.3/230.4	[178]
CsPbBr ₃ /GeSn	450–2200	≈4.7 @ 2200 nm	–	–	–	–	–/26	[179]
MAPbI ₃ /Si	400–1200	18.4 @ 970 nm	1.8 × 10 ¹² @ 970 nm ^{a)}	23.5%	–	–	–	[180]
MAPbI ₃ /DPP-CNTVT	400–980	500 @ 720 nm	10 ¹⁴ @ 720 nm ^{a)}	≈90 @ 720 nm	–	265 ^{c)}	0.27/0.21	[181]
Photoconductors								
MAPbI ₃	400–1000	≈4 × 10 ³ @ 800 nm	–	≈600% @ 800 nm	–	–	39/1.9	[41]
MAPbI ₃	400–1064	≈150 @ 820 nm (MAPbI ₃)	–	≈22% @ 820 nm	–	–	1.2 × 10 ⁵ /8 × 10 ⁴	[45]
MAPbI ₃ /PDPP3T	300–940	154 @ 835 nm 5.5 @ 937 nm	8.8 × 10 ¹⁰ @ 835 nm 3.2 × 10 ⁹ @ 937 nm ^{b)}	≈1% @ 937 nm	–	–	≈3 × 10 ⁴ / ≈1.5 × 10 ⁵	[50]
MAPbI _{3-x} (SCN) _x /Si-NWs	350–1100	1.3 × 10 ⁴ @ 800 nm	1.0 × 10 ¹³ @ 800 nm ^{a)}	–	–	–	22.2/17.6	[182]
MAPbI ₃ nanocrystal	400–980	1.42 × 10 ³ @ 808 nm; 4.43 × 10 ⁻² @ 980 nm	1.7 × 10 ¹³ @ 808 nm 1.34 × 10 ⁸ @ 980 nm ^{a)}	–	–	–	2.79 × 10 ⁵ / 3.41 × 10 ⁵	[183]
FA _{0.85} Cs _{0.15} PbI ₃ /Bi ₂ Se ₃	300–1000	1.02 × 10 ³ @ 980 nm	2.08 × 10 ¹² @ 980 nm ^{a)}	1604% @ 650 nm	–	–	16/14	[184]
MAPbI ₃ /SnPc	300–1000	0.72 @ 980 nm	6.98 × 10 ⁹ @ 980 nm ^{a)}	0.09% @ 980 nm	–	–	390/530	[185]
MAPbI ₃ /PbS QDs	300–1200	2 × 10 ⁹ @ 800 nm	10 ¹⁵ @ 800 nm ^{b)}	80% @ 600–900 nm	–	–	2/23.8	[186]

Table 4. Continued.

Photoactive materials	Spectral range [nm]	Responsivity [mA W ⁻¹]	Specific detectivity [Jones]	EQE	f_{-3dB} [kHz]	LDR [dB]	t_{rise}/t_{fall} [μs]	Ref.
MAPbI ₃ /PbS-SCN QDs layer	365–1550	1.58 × 10 ³ @ 940 nm	3.0 × 10 ¹¹ @ 940 nm ^{a)}	–	–	–	<4.2 × 10 ⁴	[187]
MAPbI _{3-x} Cl _x /PbS QDs	300–1500	350 @ 1300 nm	9 × 10 ¹⁰ @ 1300 nm ^{a)}	–	100	–	250/500	[188]
MAPbI ₃ /CuInSe ₂ QDs	400–880	10.4 @ 880 nm	–	–	1.5	–	-/236	[189]
MAPbI _{3-x} Cl _x /PbPc	400–850	2.51 @ 830 nm	2 × 10 ¹⁰ @ 830 nm ^{a)}	0.4% @ 830 nm	–	–	520/416	[190]
NaYF ₄ :Yb,Er QDs layer/α-CsPbI ₃ QDs layer	260–1100	–	–	–	–	–	5 × 10 ³ /5 × 10 ³	[191]
NaYF ₄ :Yb/Er nanoparticles layer/ MAPbI ₃ microarray	408–1033	270 @ 980 nm	7.6 × 10 ¹¹ @ 980 nm ^{a)}	14% @ 850 nm 48% @ 980 nm	–	–	5.2 × 10 ⁴ /6.7 × 10 ⁴	[67]
(CsPbI ₃) _{0.05} ((FAPbI ₃) _{1-x} (MAPbBr ₃) _{0.5x} (MAPbI ₃) _{0.5x}) _{0.95} /Ti ₃ C ₂ T _x MXene	405–810	1.159 × 10 ⁴ @ 808 nm	4.41 × 10 ¹¹ @ 808 nm ^{a)}	≈10% @ 808 nm	–	82 ^{c)}	2.46 × 10 ⁴ / 1.47 × 10 ⁴	[192]
Phototransistors								
MAPbI _{3-x} Cl _x /poly(3-hexylthiophene)/graphene	350–1300	1.1 × 10 ¹² @ 895 nm; 8.76 × 10 ⁵ @ 1300 nm	–	–	–	–	<10 ⁶	[193]
MAPbI _{3-x} Cl _x	350–1100	7.6 × 10 ¹¹ @ 895 nm; 10 ¹² @ 1100 nm	5.6 × 10 ¹³ @ 895 nm ^{b)}	–	–	–	–	[194]
MAPbI _{3-x} Cl _x /black phosphorous	350–1200	5.2 × 10 ⁸ @ 895 nm	4.3 × 10 ¹² @ 895 nm ^{b)}	–	–	–	8 × 10 ³ /1.7 × 10 ⁴	[44]
MAPbI ₃ /MoS ₂	500–850	1.11 × 10 ⁵ @ 850 nm	2.39 × 10 ¹⁰ @ 850 nm ^{b)}	–	–	–	≈6.17 × 10 ⁶ / ≈4.5 × 10 ⁶	[195]
MAPbI ₃ /PbSe QDs layer	300–1500	≈700 @ 1200 nm	≈7 × 10 ⁷ @ 1200 nm ^{a)}	–	–	–	2.5 × 10 ³ /3 × 10 ³	[49]
CsPbI ₃ QDs/DPP-DTT	350–940	≈3.3 × 10 ⁴ @ 800 nm	–	–	–	–	3.2 × 10 ⁶ /3.3 × 10 ⁶	[42]
Erbium silicate nanosheet/MAPbI ₃	500–800, 1530–1565	0.11 @ 1530 nm	–	0.01% @ 1530 nm	–	–	900/900	[54]
MAPbI ₃	600–900	–	7.13 × 10 ¹¹ @ 800 nm ^{b)}	–	–	–	–	[196]
MAPbI ₃ /graphene	400–1000	≈30 @ 1000 nm	–	≈5% @ 1000 nm	–	–	8.7 × 10 ⁴ /5.4 × 10 ⁵	[197]

^{a)}The specific detectivity of the corresponding device was inferred from the dark current; ^{b)}The specific detectivity of the corresponding device was calculated by the measured noise; ^{c)}The formula coefficient of LDR was 20; ^{d)}The formula coefficient of LDR was 10.

significantly enhance the efficiency of carrier extraction, as the schematic depicts in Figure 6a. Furthermore, the unique structure with MAPbI₃ perovskite immersed the ZnO nanowire array generally has the high surface-to-volume ratio of carriers, contributing to the enhanced performance of PDs. Notably, perovskite heterojunction PDs first expand the spectral range to exceed 1000 nm without the incorporation of narrow-bandgap materials (Figure 6b), which was attributed to the intraband transition. The resultant PDs possess a high responsivity of 0.22 A W⁻¹ and a detectivity of 9.3 × 10⁹ Jones (inferred from shot noise determined by the dark current) under 1357 nm illumination with the intensity of 30 mW cm⁻², and achieve a rise time of 0.3 s and a fall time of 0.8 s (Figure 6c).

Localized trap states within the bandgap of polycrystalline hybrid perovskites broaden the absorption region from UV–vis to NIR.^[44,140,183,193,194,196,197] Feng Yan and co-workers demonstrated the spectral response of the MAPbI_{3-x}Cl_x perovskite phototransistor to 1.1 μm.^[194] The device architecture

of perovskite/organic semiconductor vertical-heterojunction phototransistors is shown in Figure 7a. Under light illumination, photogenerated electron-hole pairs within perovskites can easily dissociate into free carriers in perovskite films or at the interface of perovskite/poly-(3,4-ethylenedioxythiophene)-poly(styrenesulfonate) (PEDOT:PSS). Free holes diffuse to the PEDOT:PSS layer and dominate the channel current of the phototransistor, due to the higher hole mobility (≈5.6 cm² V⁻¹ s⁻¹) of the PEDOT:PSS layer and the lower electron mobility (≈1.7 × 10⁻⁴ cm² V⁻¹ s⁻¹) of the perovskite layer. Meanwhile, free electrons would accumulate in the perovskite layer as illustrated in Figure 7b. Therefore, benefiting from long carrier lifetimes and strong light absorption of perovskites, the photogating effect causes holes in the PEDOT:PSS layer to recirculate many times, resulting in an ultrahigh gain. The presence of the electron accumulation in the MAPbI_{3-x}Cl_x perovskite layer would significantly reduce the response speed of the phototransistor. The thinner thickness of the perovskite

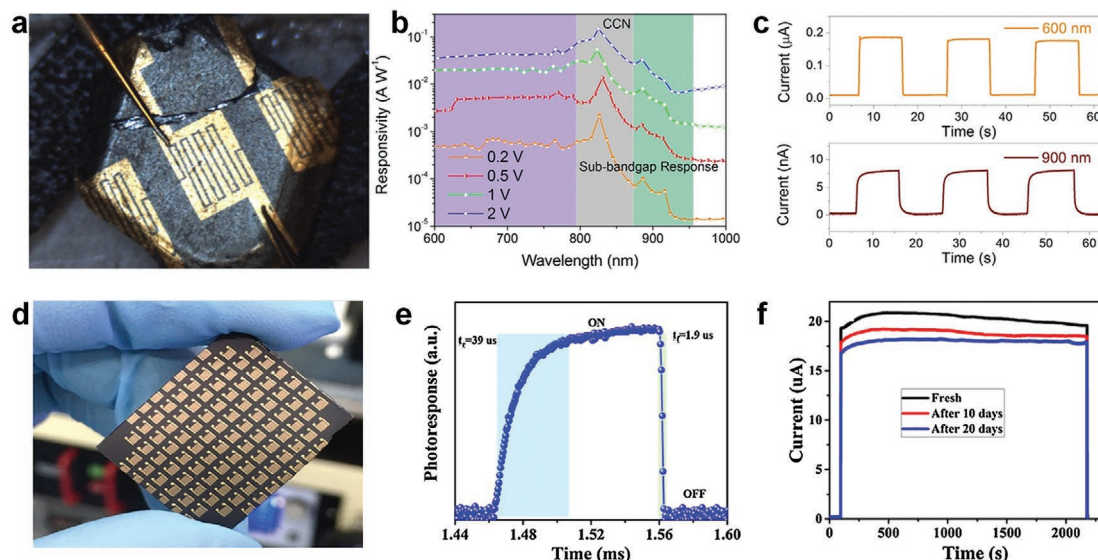


Figure 5. a) Photograph of a photoresistor based on MAPbI₃ single crystals. b) Responsivity of a MAPbI₃ photoresistor with different bias. c) Photocurrent cycles of the MAPbI₃ photoresistor at 0.5 V bias. d) Photograph of a photoconductor array on a MAPbI₃ single crystal wafer and its e) response time. f) The reliability test results of MAPbI₃ PDs under atmospheric conditions. a–c) Reproduced with permission.^[45] Copyright 2016, Wiley-VCH. d–f) Reproduced with permission.^[41] Copyright 2017, Elsevier B.V. and Science Press.

layer, the lower densities of deep trap states, contributing to the increased response speed (greater than 10 min) but a reduced responsivity. Expectedly, the responsivity of the device gradually increases to saturation with the thickness increase of the photoactive layer. The thickness of the MAPbI_{3-x}Cl_x perovskite layer

and the PEDOT:PSS layer were optimized to ≈300 nm and ≈43 nm, and the optimized responsivity, detectivity and gain of the phototransistor were 7.6×10^8 A W⁻¹, 5.6×10^{13} Jones, and 1.1×10^9 at 895 nm wavelength under 0.5 V bias. In addition, as shown in Figure 7c, the flexibility of the phototransistor

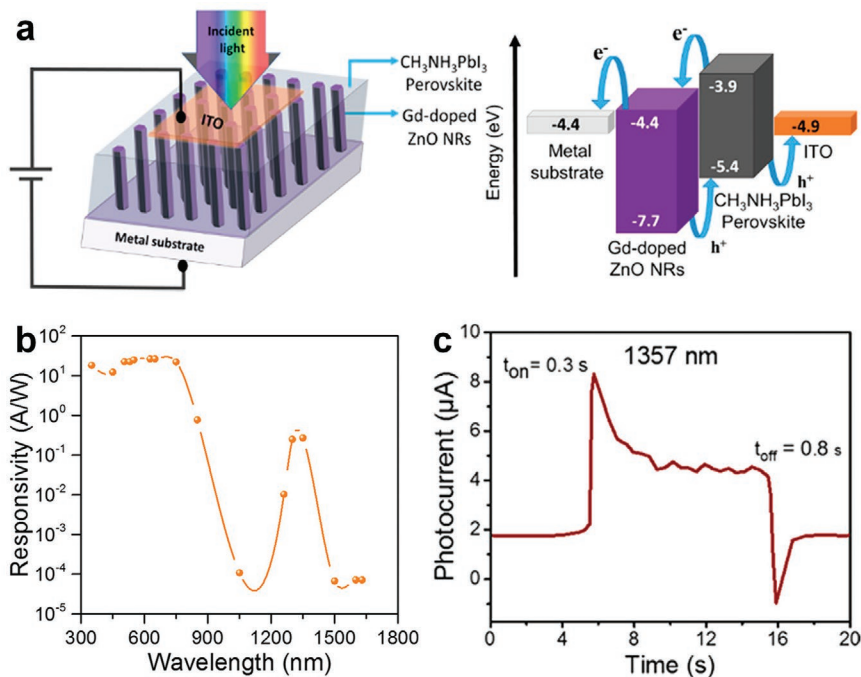


Figure 6. a) Architecture and energy-level diagram of PDs with components of metal substrates, Gd-doped ZnO nanorods, MAPbI₃, and indium tin oxide (ITO). b) Responsivity of PDs. c) Temporal response of PDs under 1357 nm illumination with the power density of 30 mW cm⁻². Reproduced with permission.^[156] Copyright 2017, American Chemical Society.

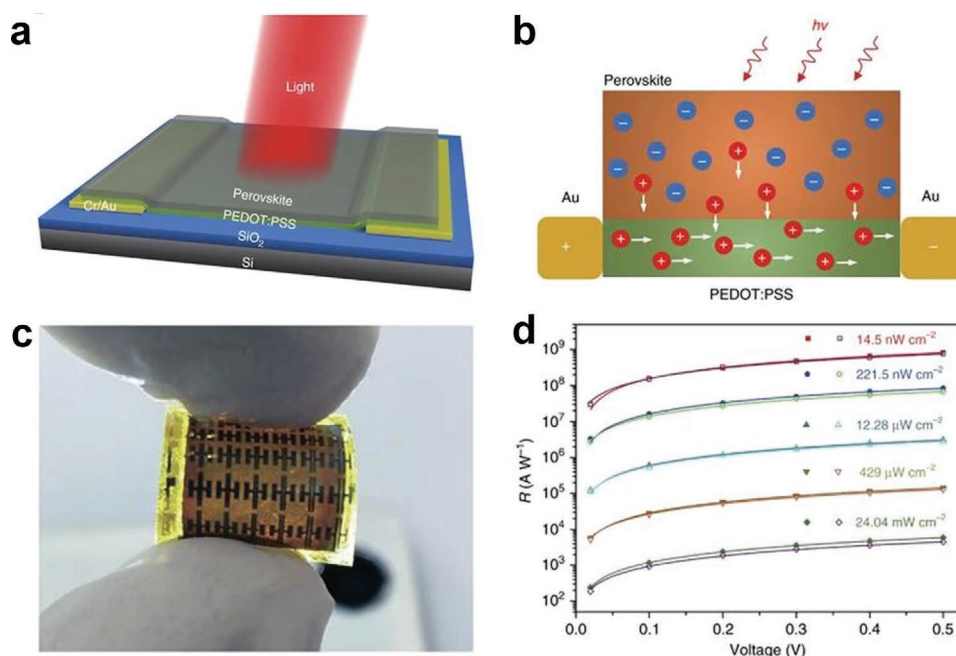


Figure 7. a) Architecture and b) working diagram under light illumination of MAPbI_{3-x}Cl_x/PEDOT:PSS heterojunction phototransistors. c) Photograph of the flexibility of the phototransistor. d) Responsivity comparison of phototransistors before (solid dots) and after (hollow dots) the bending test. Reproduced with permission.^[194] Copyright 2017, Nature Publishing Group.

with the same component was demonstrated by applying a flexible substrate of polyimide. The performance of the flexible device in the NIR range remain almost unchanged after being bent 300 times to a radius of 7 mm (Figure 7d). Apart from PEDOT:PSS, some other functional materials, including graphene,^[197] poly(3-hexylthiophene),^[193] 4,4'-bis([p-trichlorosilylpropylphenyl]phenylamino)-biphenyl (TPD-Si₂),^[140] and black phosphorous,^[44] have also been applied to combine with the perovskite layer to effectively separate and transport carries, and thus significantly improve device performance.

Shengyi Yang and co-workers employed surface trap states correlated with surfaces of MAPbI₃ nanocrystals to achieve the NIR photodetection.^[183] Self-powered coplanar PDs with the device structure of ITO/MAPbI₃ nanocrystals (mean diameter sizes of 6.2 nm)/Ag were fabricated. The work function difference between Ag and ITO could provide the built-in electric field to effectively separate photogenerated electron-hole pairs without an external electric field. Due to trap states related with self-doping and surface states in perovskites, prepared PDs show the spectral response range to about 1000 nm wavelength. Self-powered PDs have a responsivity of 1.42 A W⁻¹, a specific detectivity of 1.77 × 10¹³ Jones (inferred from shot noise determined by the dark current), a $I_{\text{light}}/I_{\text{dark}}$ ratio of 932, a rise time of 279 ms, and a fall time of 341 ms at 808 nm wavelength (26 μW cm⁻²). When the irradiation wavelength was extended to 980 nm, the responsivity, specific detectivity and $I_{\text{light}}/I_{\text{dark}}$ ratio sharply dropped to 4.43 × 10⁻⁵ A W⁻¹, 1.34 × 10⁸ Jones, and 6.61, respectively. Further, an array of 4 × 9 pixels was demonstrated its imaging function. Regarding the storage stability, asymmetric-electrode-configuration PDs based on MAPbI₃ nanocrystals retained its initial photocurrent up to 90% after 1-month storage in the air.

Benefiting from the two-photon absorption, Pb-based perovskites can also achieve NIR response.^[159,200,201] Keli Han and co-workers deposited CsPbBr₃ microcrystals (few tens of micrometers in size) on the ITO substrate to produce NIR photoconductors based on the two-photon absorption.^[161] With the carrier mobility over 100 cm² V⁻¹ s⁻¹ and the low density of trap states of 4.5 × 10¹² cm⁻³, the prepared photoconductors with a channel of 5 μm achieve a responsivity of up to 6 A W⁻¹ under a pulsed laser beam of 800 nm wavelength. Similarly, Weiqiao Deng, Rongxing He, and co-workers deposited FAPbBr₃ microcrystals with the mean size of around 10 μm on an interdigitated ITO substrate to fabricate NIR photoconductors with the active area of 5 μm × 1 mm.^[160] The one-photon responsivity was calculated to be 4000 A W⁻¹ at 495 nm wavelength and the two-photon responsivity was calculated to be 0.07 A W⁻¹ at 800 nm wavelength, suggesting the potential application of Pb-based perovskites in NIR detection based on their nonlinear optical properties.

4.3. Pb Perovskites Incorporated with Near-Infrared Materials for Near-Infrared Photodetection

Although the sub-bandgap absorption of perovskites and the intraband transition of valence electrons could promote their NIR detection capability, PDs generally suffer from the low NIR responsivity induced by the weak NIR absorption, or the slow temporal response caused by trap states. As a consequence, the incorporation of various narrow-bandgap materials with Pb-based perovskites employs the interband transition to fabricate high-responsivity and fast-response NIR PDs, which gradually dominates the mainstream of research.

4.3.1. Pb Perovskites Incorporated with Inorganic Near-Infrared Materials

With a bandgap of ≈ 1.1 eV and the advantage of mature processing techniques, silicon has been widely applied to integrate with perovskites for highly sensitive and broadband light detection.^[38,165,177–180,182] Lin-Bao Luo, Yu-Cheng Wu, and co-workers reported a sensitive NIR PD through coating a vertical p-type silicon nanowire array (an average length of ≈ 15 μm and an average diameter of ≈ 140 nm) with a Cs-doped FAPbI₃ perovskite layer (40–50 nm thickness).^[38] The silicon nanowire/perovskite core-shell heterojunction NIR photodiode shows the spectral detection region from 300 to 1200 nm with the maximum sensitivity at around 850 nm. Benefiting from the photovoltaic effect and the strong light-trapping effect in the core-shell heterojunction structure, self-powered PDs achieve a $I_{\text{light}}/I_{\text{dark}}$ ratio of 1.23×10^4 , a responsivity of 14.86 mA W^{-1} , a specific detectivity of 2.04×10^{10} Jones (inferred from shot noise determined by the dark current), a rise time of 4 μs and a fall time of 8 μs at 850 nm illumination. In addition, dark current and photocurrent of prepared PDs are almost invariant after 3-week storage under ambient conditions, suggesting the excellent ambient stability. Similarly, silicon nanoporous pillar array (NPA)^[178] and silicon nanowire^[182] were applied as the substrate to grow the perovskite layer to realize NIR photodetection. The silicon NPA structure presents several advantages, including the low light reflection, a large specific surface area that enhances the light harvesting capability, nanoporous morphologies that multiply the transport and extraction paths of carriers, an excellent template that facilitates the growth of pinhole-free and dense perovskite thin films,^[38] and a high-hole-mobility p-type contact. The SEM (scanning electron microscope) image of the Si-NPA substrate covered with the perovskite layer is depicted in **Figure 8a**, and the optical absorption spectrum and the photoluminescence (PL) spectrum of different active films are shown in **Figure 8b**. Prepared silicon NPA/MAPbI₃/ZnO heterojunction photodiodes achieve a responsivity of 8.13 mA W^{-1} , a specific detectivity of 9.74×10^{12} Jones (inferred from shot noise determined by the dark current), a rise time of 253.3 μs , and a fall time of 230.4 μs under 780 nm illumination at the zero bias. Additionally, PDs without encapsulation show the 8% photocurrent degradation after one-month storage in air ambient due to the protection of two inorganic layers of silicon NPA and ZnO. Yingquan Peng and co-workers efficiently controlled the morphology and crystallinity of MAPbI_xCl_{3-x} polycrystalline perovskites to fabricate uniform thin films through the introduction of polyvinyl pyrrolidone (PVP), as confirmed by the XRD test results in **Figure 8c**.^[165] Broadband photodiodes with the structure of heavily doped p-type silicon/PVP:MAPbI_xCl_{3-x}/Au have the spectral response extended to 980 nm and show an excellent spectral uniformity of responsivity in the region of 450–808 nm and reproducibility, as shown in **Figure 8d**.

The mismatched energy-level alignment at the interface of perovskite/silicon would impede the carrier transport and extraction, and thus lead to reduced performance. Several metal oxides have been introduced to tackle the energy band mismatch and boost interfacial carrier separation.^[168,170] For instance, Liang Li, Yue Zhang, and co-workers inserted a TiO₂ layer to improve separation and reduce recombination of carriers at the

interface between the n-type silicon wafer and the perovskite layer.^[168] PDs with a tri-layer structure of Ag/MAPbI_xCl_{3-x}/TiO₂ (35 nm thickness)/silicon/indium:gallium extend the spectral response to 1150 nm wavelength and achieve the highest responsivity of $0.87 \text{ A} \cdot \text{W}^{-1}$ at the wavelength of 800 nm, and a specific detectivity of over 10^{12} Jones (inferred from shot noise determined by the dark current) in the NIR region (780–1100 nm). Similarly, a SnO₂ layer (40 nm thickness) has been inserted in the perovskite-silicon interface, which reduces the photogenerated carrier recombination and suppresses the dark current generation, resulting in the enhanced detectivity.^[170]

Perovskite NIR PDs have been explored in the flexible form. Jie Xiong, Liang Li, and co-workers demonstrated a self-powered flexible fiber-shaped photodiode (**Figure 8e**) with the spectral response range of 350–1050 nm.^[166] A compact TiO₂ layer (30 nm thickness) was deposited on a flexible carbon fiber as an electron transport and hole block layer, on which a MAPbI₃ layer was subsequently crystallized. In parallel, the flexible copper wire was annealed in air to form a compact layer of CuO nanowire with a Cu₂O underlayer. The annealed flexible copper wire was twisted with the prepared perovskite/TiO₂/carbon fiber to finally compose the fiber-shaped broadband photodiode. Desirable energy-level alignment is crucial in PDs and could be realized by the insertion of suitable interfacial layers to modulate charge transport behaviors, which would facilitate the extraction of photogenerated carriers within active layers.^[51,168,170] As the energy band diagram illustrated in **Figure 8f**, the inserted layers of TiO₂ and Cu₂O effectively reduced the dark current to as low as 10^{-11} A (at 0 V bias) due to the lower valence band of TiO₂ and the higher conduction band of Cu₂O. Meanwhile both inserted layers contributed to the increased photocurrent as a result of the excellent electron extraction at TiO₂/perovskite interfaces and hole extraction at Cu₂O/perovskite interfaces. The NIR response of the PDs was ascribed to the narrow-bandgap CuO. Self-powered NIR PDs achieve a responsivity of 562.9 mA W^{-1} and a detectivity of 2.15×10^{13} Jones (inferred from shot noise determined by the dark current) at 800 nm wavelength, a responsivity of 7.3 mA W^{-1} and a detectivity of 2.91×10^{11} Jones at 1000 nm wavelength. In addition, fiber-shaped photodiodes present the photocurrent stability after 60 bending cycles, and devices can be deployed to sense photons at a deflected condition (i.e., detecting signals when devices were bent to 90°).

Narrow-bandgap 2D TMDs have been explored their roles in Pb perovskite NIR PDs, including PtSe₂, PdSe₂, and MoS₂.^[167,169,195] Due to the strong built-in electric field generated by the heterojunction contact between TMDs and perovskites, and the NIR absorption and the high carrier mobility of TMDs, Pb-based perovskites incorporated with TMDs could achieve the efficient broadband photodetection and a fast response speed. For instance, self-powered FA_{0.85}CS_{0.15}PbI₃/polycrystalline multilayer semimetal PtSe₂ (≈ 15 nm thickness) heterojunction photodiodes were demonstrated to have a wide spectral response from 300 to 1200 nm, a high responsivity of 117.7 mA W^{-1} and a specific detectivity of $\approx 10^{12}$ Jones at the wavelength of 808 nm. The schematic device structure, the responsivity and detectivity as a function of the wavelength of incident light are presented in **Figure 9a**. The NIR detection was attributed to photo-excited electrons from PtSe₂ to the

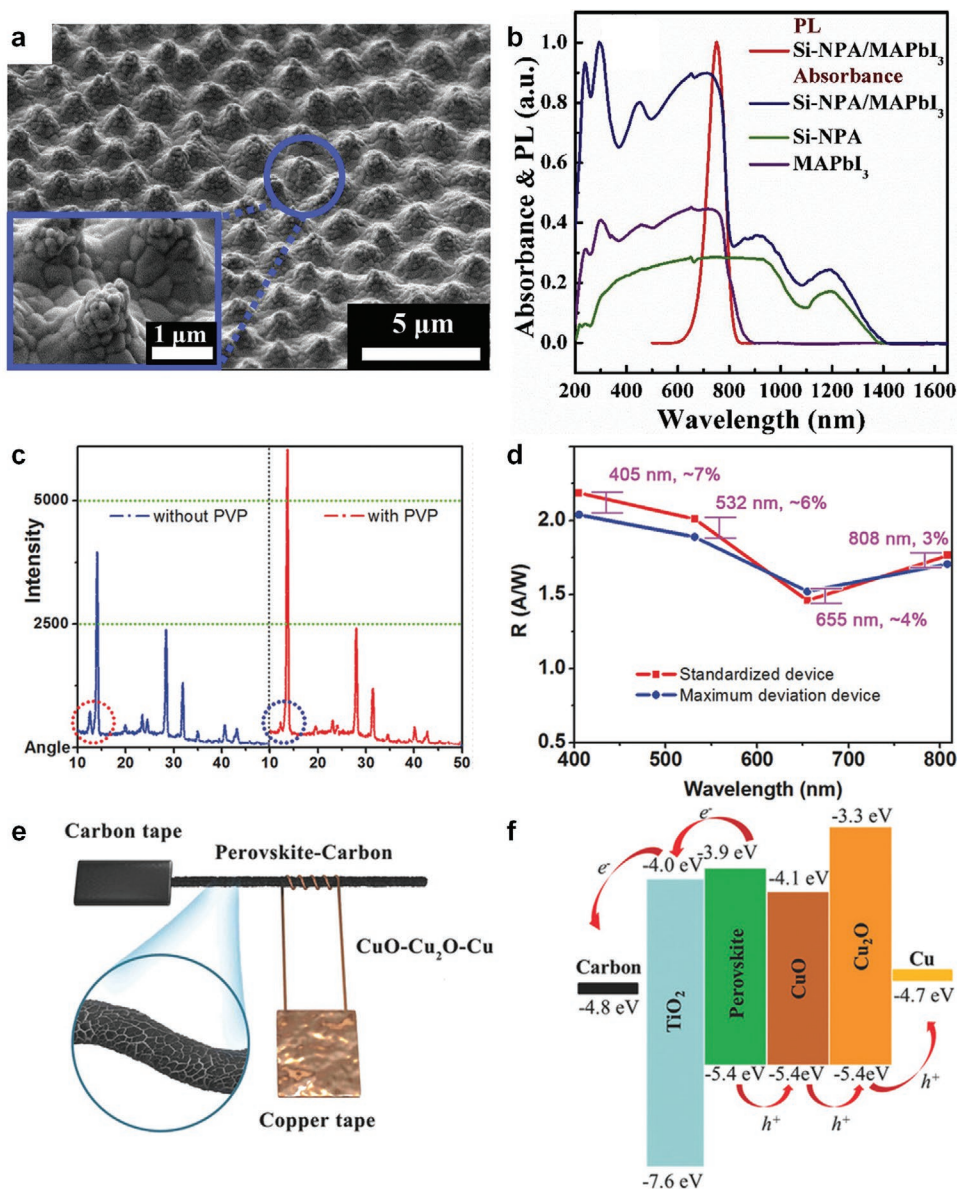


Figure 8. a) The SEM image of the Si-NPA substrate covered with the perovskite layer. b) Optical absorption and PL spectrum of different films. c) XRD patterns of perovskite films with and without PVP. d) Responsivity comparison of devices in different wavelengths. e) Schematic diagram and f) energy-level diagram of fiber-shape PDs. a,b) Reproduced with permission.^[178] Copyright 2020, Elsevier B.V. c,d) Reproduced with permission.^[165] Copyright 2017, Wiley-VCH. e,f) Reproduced with permission.^[166] Copyright 2018, Wiley-VCH.

conduction band of perovskites. Moreover, the photodiode shows a rise/fall time of 78/60 ns in the photovoltaic mode (Figure 9b) and achieves the excellent photocurrent reproducibility of over 1000 cycles and the photocurrent stability after 3-week storage in ambient conditions, as illustrated in Figure 9c.^[167] Yuen Hong Tsang and co-workers demonstrated a self-powered Schottky-junction photodiode with the structure of PdSe₂/FA_{0.85}CS_{0.15}PbI₃.^[169] As-assembled PdSe₂/perovskite photodiodes have the spectral response range from 200 to 1550 nm. The ability of NIR detection is resulted from the photogenerated electrons from semimetal PdSe₂ to perovskites. Byungha Shin, Jin-Hong Park, and co-workers introduced MoS₂ with the MAPbI₃ layer to demonstrate a broadband phototransistor

(Figure 9d) with ultrahigh performance.^[195] With the NIR absorption of MoS₂, the phototransistor achieves a responsivity of 104.24 A W⁻¹ and a specific detectivity of 2.39 × 10¹⁰ Jones at the wavelength of 850 nm. Furthermore, they adopted the APTES ((3-aminopropyl)triethoxysilane) surface treatment on the SiO₂/Si substrate to induce n-type doping with the MoS₂ layer, which would reduce the carrier recombination rate and thus dramatically increase the responsivity in the visible region (Figure 9e). Despite this treatment causes the limited responsivity improvement in the NIR region that is out of the absorption range of the perovskite layer, it could improve the response speed of the phototransistor (Figure 9f). More importantly, they applied a bilayer of OTS (octadecyltrichlorosilane)/PMMA

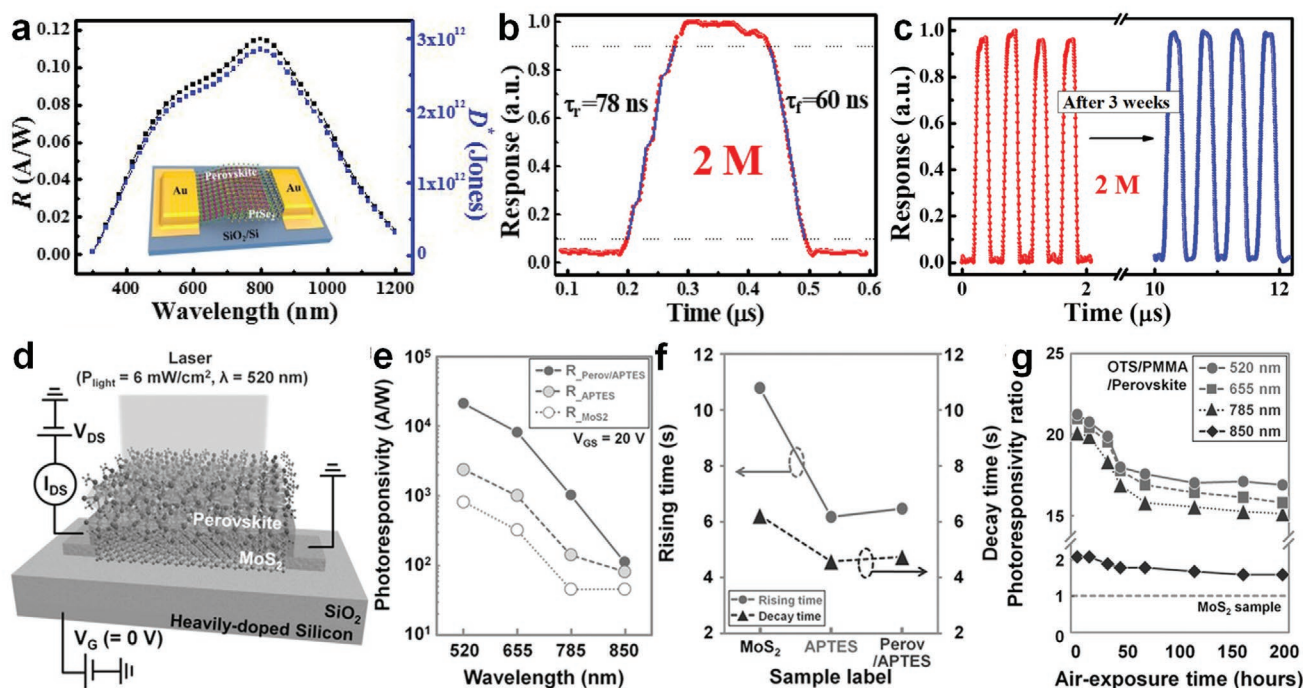


Figure 9. a) Responsivity and detectivity of perovskite/PtSe₂-based PDs. The inset shows the device structure. b) A normalized switching cycle of PDs. c) Comparison of normalized photocurrent response before and after 3-week storage in air. d) Schematic of perovskite/MoS₂-based phototransistors. e) Responsivity and f) the rise/fall time of perovskite/MoS₂/APTES, MoS₂/APTES, and MoS₂ phototransistors. g) Responsivity degradation curve of OTS/PMMA-encapsulated perovskite/MoS₂/APTES phototransistors in ambient conditions. a–c) Reproduced with permission.^[167] Copyright 2018, American Chemical Society. d–g) Reproduced with permission.^[195] Copyright 2016, Wiley-VCH.

(poly(methyl methacrylate)) to encapsulate PDs, which thus intentionally increase the device stability. OTS/PMMA-covered PDs could maintain the responsivity up to 80% and the detectivity up to 70% after the air-exposure time of 200 h (Figure 9g).

Narrow-bandgap inorganic QDs (e.g., PbS and PbSe) are suitable components for complementary NIR absorption in broadband Pb-based perovskite PDs. Benefiting from the size-tunable bandgap of QDs, the high absorption coefficient of perovskites, and the passivation of perovskites on surfaces of QDs, QDs/perovskite heterojunction PDs realize the efficient broadband detection and the fast response.^[43,47,49,187] Xiong Gong and co-workers combined a layer of PbS QDs, of which the average diameter is around 5 nm and the bandgap is around 1.1 eV, with MAPbI₃ perovskite to develop a broadband photodiode as shown in Figure 10a.^[47] Compared with pristine PbS QDs-based PDs, PbS QDs/MAPbI₃-based devices achieve the enhanced responsivity in the NIR region, which originate from the dual-function of MAPbI₃ for simultaneously passivating trap states on surfaces of PbS QDs and broadening the depletion region in the PbS QDs layer. Thus, the dark current of the device was effectively suppressed from 9.4×10^{-8} to 2.1×10^{-9} A cm⁻². The complementary NIR absorption and effective carrier separation contribute to the good photoelectric performance of PbS QDs/MAPbI₃ photodiodes. Resultant PDs show the spectral response region from 375 to 1100 nm, a responsivity of 132 mA W⁻¹ (the corresponding EQE is 18.2%) and a specific detectivity of 5.1×10^{12} Jones (inferred from shot noise determined by the dark current) at 900 nm wavelength. Similarly, the thiocyanate anion (SCN⁻) was introduced to

passivate PbS QDs for energy-level regulation and electrical conductivity enhancement. PbS-SCN/MAPbI₃ composite photoconductors exhibit the broadband photodetection from 365 to 1550 nm, a responsivity of 1.58 A W⁻¹ and a detectivity of 3.0×10^{11} Jones (inferred from shot noise determined by the dark current) at 940 nm wavelength.^[187] Importantly, an array of 10×10 pixels with a pixel size of $100 \mu\text{m} \times 1000 \mu\text{m}$ were successfully demonstrated the function of broadband image sensing, as demonstrated in Figure 10b.

PbSe QDs/MAPbI₃ layered heterojunction PDs have been investigated for sensing NIR. Yating Zhang and co-workers fabricated MAPbI₃/PbSe QDs hybrid phototransistors to realize the broadband detection at the wavelength of 300 to 1500 nm. Hybrid phototransistors possess the rise/fall time of $\approx 2.5/3$ ms, and importantly exhibit the stable and reproducible photocurrent response at 808 nm illumination with the ultrahigh light intensity of 845 mW cm^{-2} in a short time of ≈ 140 s.^[49] Matthew L. Becker, Xiong Gong, and co-workers demonstrated a solution-processed vertical broadband photodiode by combining MAPbI₃ with a PbSe QDs layer.^[40] Remarkably, due to the trap-assisted photomultiplication effect of PbSe QDs, perovskite/PbSe QDs bilayer photodiodes achieve the high responsivity of over 230 mA W⁻¹ and the specific detectivity of 10^{11} Jones (inferred from shot noise determined by the dark current) covering the range from 300 to 2600 nm under a negative bias of 1 V. Notably, the high response in the infrared range is related to formamidinium iodide-treated conductive PEDOT:PSS thin films, which possess over 60% transmittance in the NIR region and 40% in the middle IR region (up to

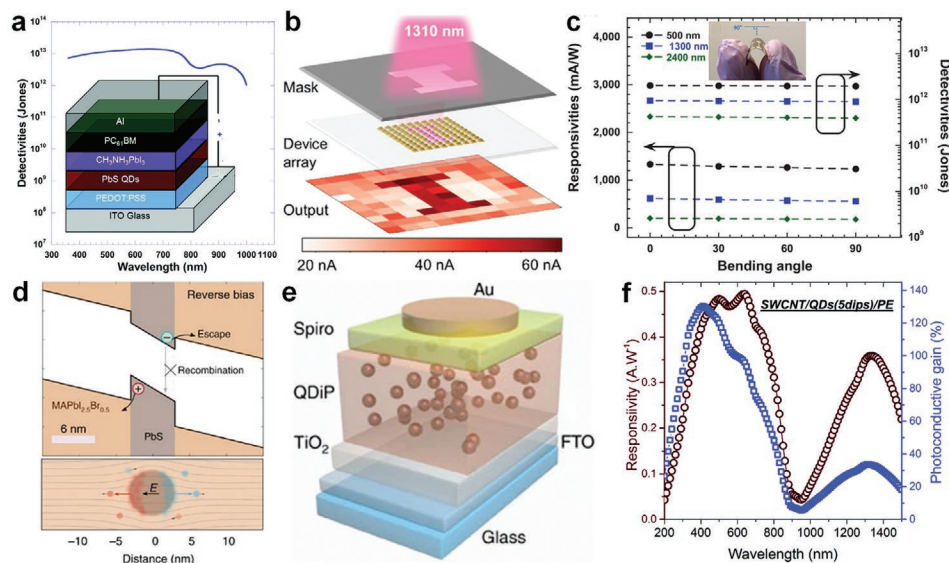


Figure 10. a) Wavelength-dependent detectivity of PbS QDs/MAPbI₃ PDs. The insert shows the schematic of PDs. b) Imaging demonstration of 10 × 10 PDs array under NIR illumination. c) Responsivity and detectivity of PDs under different bending angles. The insert shows a bending angle of 90°. d) Band alignment of PbS QDs/MAPbI_{2.5}Br_{0.5} under a reverse bias. e) Device schematic of quantum-dots-in-perovskite PDs. f) Responsivity and gain of PDs under different wavelength. a) Reproduced with permission.^[47] Copyright 2015, The Royal Society of Chemistry. b) Reproduced with permission.^[187] Copyright 2019 American Chemical Society. c) Reproduced with permission.^[40] Copyright 2020, Wiley-VCH. d,e) Reproduced with permission.^[43] Copyright 2017, Springer Nature. f) Reproduced with permission.^[188] Copyright 2018, The Royal Society of Chemistry.

7 μm), and the high electrical conductivity of 1562 S cm⁻¹. Moreover, vertical broadband photodiodes show the excellent flexibility with the negligible degradation of both responsivity and the specific detectivity when devices are bent into even 90°, as shown in Figure 10c.

PbS QDs:perovskite bulk heterojunction has been introduced to obtain NIR PDs. Edward Sargent and co-workers mixed PbS QDs into MAPbI_{2.5}Br_{0.5} perovskite through a solution process and fabricated field-emission photodiodes with the detection range extending to 1400 nm.^[43] They proposed a new type of semiconductors called quantum-dots-in-perovskite (i.e., QDs embedded in an epitaxially grown perovskite matrix), in which forms the type-I heterojunction between PbS QDs and MAPbI_{2.5}Br_{0.5} perovskite. Without an external electric field, photogenerated excitons are confined inside QDs due to the type-I heterojunction; with a large electric field, excitons photo-generated inside QDs will separate and then these free charges may be ejected from QDs into the host perovskite matrix by Fowler–Nordheim tunneling (Figure 10d), contributing to the photocurrent. Prepared photodiodes have the device structure of FTO (fluorine-doped tin oxide)/TiO₂/quantum-dots-in-perovskite/Spiro-MeOTAD (a hole transport layer)/Au, as shown in Figure 10e. The reported photodiodes showcase an EQE of 40% at 1240 nm wavelength under a bias of -3 V, a -3 dB bandwidth of 60 kHz, a LDR of 60 dB (the coefficient of LDR is 10), a high specific detectivity of 4 × 10¹² Jones at 1240 nm wavelength, and a working stability of over 100 h under continuous operation. Jiang Huang, Junsheng Yu and co-workers employed an antisolvent additive solution process to disperse PbS QDs between the grain boundaries of MAPbI₃ perovskite and optimized its crystallization and morphology by controlling the volume of antisolvent additive.^[171] The

antisolvent additive solution process was realized by adding PbS QDs in toluene to the perovskite precursor in DMF. PbS QDs:MAPbI₃ bulk heterojunction photodiodes have a low EQE of ≈6% at 900 nm wavelength in the photovoltaic mode and a low specific detectivity of 10¹¹ Jones (inferred from shot noise determined by the dark current) in the NIR region. Ibrahim Ka, Riad Nechache, Sylvain G. Cloutier, and co-workers incorporated single-wall carbon nanotubes (SWCNT) into the hybrid of MAPbI_{3-x}Cl_x and PbS QDs to form broadband photoconductors (Figure 10f).^[188] The embedded SWCNT functionalize as a charge collector. Apart from harvesting NIR, PbS QDs facilitate the charge transfer from perovskite to the network of SWCNT. SWCNT–PbS QDs–perovskite hybrid photoconductors achieve a responsivity of 0.35 A W⁻¹ and a detectivity of 9 × 10¹⁰ Jones (inferred from shot noise determined by the dark current) at 1300 nm wavelength, and a rise/fall time of 250/500 μs. Furthermore, PDs without encapsulation show the poor storage stability with 70% photocurrent after 10-day storage and no photocurrent after 20-day storage, possibly resulting from the poor moisture-resistant ability of perovskites.

4.3.2. Pb Perovskites Incorporated with Organic Near-Infrared Semiconductors

Organic narrow-bandgap semiconductors with flexibility and the desirable NIR absorption have been adopted to combine with perovskites to achieve flexible and broadband PDs. Dan Xie, Gaoquan Shi, and co-workers pioneered the practice of spin-coating PDPP3T (a kind of commercially conjugated polymers) solution on the top of a MAPbI₃ perovskite layer to develop a flexible broadband photoconductor.^[50] The lateral

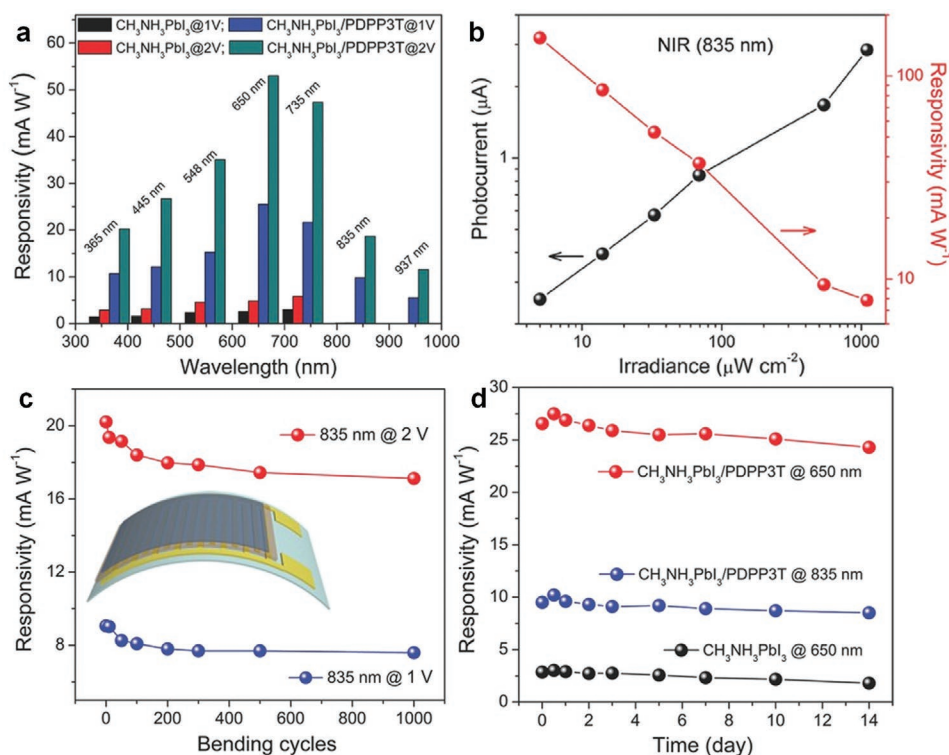


Figure 11. a) Wavelength-dependent responsivity of MAPbI₃ and MAPbI₃/PDPP3T PDs. b) Irradiance-dependent photocurrent and responsivity at 835 nm wavelength under the operation of 1 V bias. c) Responsivity versus bending cycles at a radius of 7 mm of PDs at 835 nm wavelength. The inset is the device diagram of flexible PDs. d) Stability comparison of PDs based on MAPbI₃/PDPP3T and MAPbI₃ in an Ar-filled glovebox at room temperature. Reproduced with permission.^[50] Copyright 2016, Wiley-VCH.

device constructed by perovskite/polymer heterojunction on interdigitated Au electrodes (50 μm fingers with 50 μm spaces) was deposited on flexible poly(ethylene terephthalate) (PET) substrates. Heterojunction PDs exhibit a low responsivity of 5.5 mA W⁻¹ and a specific detectivity of 3.2 × 10⁹ Jones at 937 nm wavelength under 1 V bias, indicating the capability of NIR detection with respect to pure Pb-based PDs (Figure 11a,b). It should be noted that perovskite/polymer-based PDs achieve the excellent flexibility and durability. The responsivity remains 85% after 1000 bending cycles at a curvature radius of 7 mm, as shown in Figure 11c. In addition, perovskite/polymer heterojunction devices could increase the responsivity durability, which keep around 90% of the initial responsivity with respect to 80% for pure Pb-based PDs under constant illumination in a Ar-filled glovebox for 14 days, as depicted in Figure 11d.

To increase the photocurrent extraction from organic NIR semiconductors, the hybrid device structure of perovskite/a organic bulk-heterojunction layer (i.e., organic NIR semiconductors mixed with fullerenes) has been investigated. Typically, Jinsong Huang and co-workers integrated PDPPTDTPT:phenyl-C₆₁-butyric acid methyl ester (PC₆₁BM) with MAPbI₃ to produce broadband and ultrafast photodiodes.^[51] As shown in Figure 12a, NIR-generated holes in the bulk-heterojunction layer would transfer to the perovskite layer and then be extracted by the ITO anode, the photogenerated electrons would be directly collected by the Cu cathode. Optimized photodiodes with the PDPPTDTPT:PC₆₁BM ratio of 1:2 exhibit a broad response range of 350–1050 nm (Figure 12b) and a detectivity

of over 1 × 10¹¹ Jones (inferred from the measured noise) at 900 nm wavelength. With the assistance of fullerenes in the passivation effect, the charge-trapping-induced flicker noise is significantly reduced, which ultimately results in a calculated NEP of 5 pW cm⁻². Noteworthy, hybrid photodiodes with the structure of perovskite/organic bulk-heterojunction layer reduce the device capacitance with respect to the pure organic bulk-heterojunction photodiodes, contributing to the fast response time of 88 ns for the typical device area of 7 mm² and of 6.1 ns for a small device area of 0.1 mm². Similarly, Dongge Ma and co-workers combined a bulk layer of PDPP3T:(6,6)-phenylC₇₁-butyric acid methyl ester (PC₇₁BM) with a MAPbI₃ layer to fabricate broadband photodiodes ranging from 390 to 950 nm.^[172] Although hybrid photodiodes can realize the NIR photodetection, the poor energy-level alignment at the interface of perovskite/the organic bulk-heterojunction layer generally results in the reduced responsivity in the visible/NIR region. Gang Wu, Hongzheng Chen, and co-workers introduced dual electron transport layers and demonstrated the proper energy-level alignment and distribution of PC₆₁BM (the second electron transport layer) to facilitate the extraction and transport of photogenerated charges between perovskite and the organic bulk-heterojunction layer.^[174] The integrated photodiodes exhibit the structure of ITO/NiO_x/MAPbI₃/PC₆₁BM/PTB7-Th:IEICO-4F (the first electron transport layer)/BCP/Ag. N-type IEICO-4F provides the capability of NIR absorption, the bulk heterojunction with PTB7-Th, and partially transport visible light-induced electrons transferred from MAPbI₃. The second electron transport

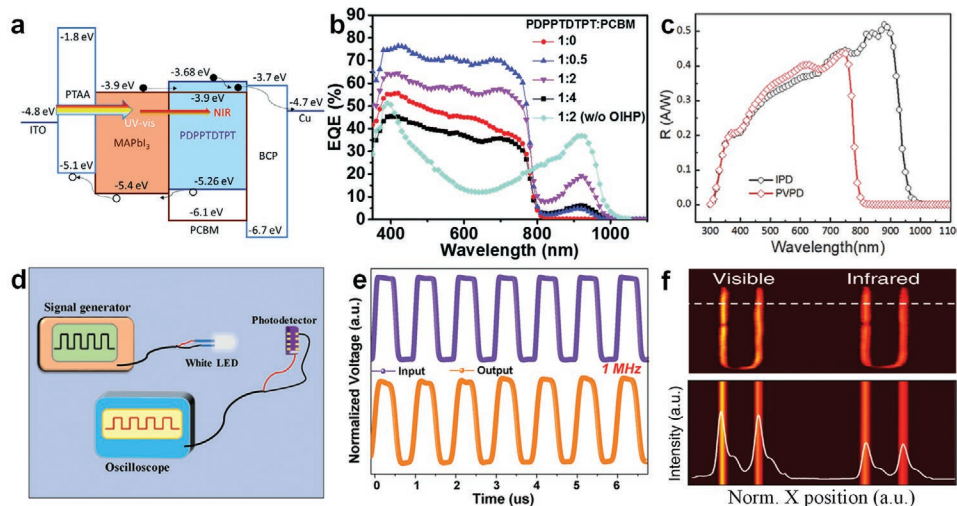


Figure 12. a) Energy band diagram of ITO/PTAA/MAPbI₃/PDPPTDTP:PC₆₁BM/BCP/Cu. b) Wavelength-dependent EQE of PDs with different PDPPTDTP:PC₆₁BM ratios. c) Wavelength-dependent responsivity of IPD and PVPD, in which the active layer of IPD contains MAPbI₃:PC₆₁BM/PTB7-Th:IEICO-4F and the active layer of PVPD only contains MAPbI₃. d) The schematic diagram the LED-PDs light communication system. e) The input and output signal of the LED-PDs light communication system at 1 MHz. f) Visible and NIR imaging. The white line represents the normalized photocurrent intensity. a,b) Reproduced with permission.^[51] Copyright 2017, The Royal Society of Chemistry. c) Reproduced with permission.^[174] Copyright 2018, Wiley-VCH. d,e) Reproduced with permission.^[175] Copyright 2019, Wiley-VCH. f) Reproduced with permission.^[176] Copyright 2020, Nature Publishing Group.

layer of PC₆₁BM promotes the extraction and transport of visible light-induced electrons from MAPbI₃ to cathode. Due to dual electron transport channels of PC₆₁BM and IEICO-4F, integrated PDs achieve the highest responsivity of 0.444 and 0.518 A W⁻¹ in the visible and NIR region, respectively (Figure 12c). Dahui Zhao, Wenping Hu, Xiong Gong, and co-workers combined MAPbI₃:SWCNTs with a bulk layer of poly[(N,N'-bis(2-octyldecyl)-1,4,5,8-naphthalene diimide-2,6-diyl) (2,5-dioctyl-3,6-di(thiophen-2-yl)pyrrolo[3,4-c]pyrrole-1,4-dione-5,5'-diyl)] (NDI-DPP):PC₆₁BM to increase the NIR responsivity.^[173] With a high charge mobility of around 10⁴ cm² V⁻¹ s⁻¹ and the formation of type II band alignment with NIR conjugated polymer NDI-DPP, SWCNTs boost the hole extraction from NDI-DPP under NIR illumination. Additionally, the incorporation of SWCNTs in MAPbI₃ offers the percolation pathways for efficient charge transport, improving the photocurrent in the visible region. Optimized hybrid photodiodes achieve an EQE of ≈20%, a responsivity of ≈150 mA W⁻¹, a specific detectivity exceeded 2 × 10¹² Jones (inferred from shot noise determined by the dark current) in the NIR region, and a LDR of over 90 dB (the coefficient of LDR is 20). Besides, due to the suppressed defects in the perovskite:SWCNTs/NDI-DPP:PC₆₁BM thin film, PDs show a rise time of 4.32 μs and a fall time of 12.16 μs.

Applications of hybrid broadband photodiodes based on perovskite/the organic NIR layer or perovskite/the organic bulk-heterojunction layer have been explored.^[175,176] Benefiting from Lewis base cyano and carbonyl of narrow-bandgap 2,2'-(2Z,2'Z)-((5,5'-(4,4,9,9-tetrakis(4-hexylphenyl)-4,9-dihydro-sindaceno[1,2-b:5,6-b']dithiophene-2,7-diyl)bis(4-((2-ethylhexyl)-oxy)thiophene-5,2-diyl))bis(methanylylidene))bis(3-oxo-2,3-dihydro-1H-indene-2,1-diylidene))dimalononitrile (IEICO) passivate the poorly coordinated Pb²⁺ in MAPbI₃, photodiodes with the structure of ITO/PTAA/MAPbI₃/IEICO/C₆₀/BCP/Cu

achieve a NIR response shoulder at 800–850 nm wavelength with the EQE of around 20%, a dark current density of 2.6 × 10⁻⁵ mA cm⁻² at -0.1 V, a fall time of 27 ns (the device area of 0.6 mm²), a specific detectivity of 737 × 10¹¹ Jones (inferred from the measured noise), and a LDR of 192 dB (the coefficient of LDR is 20) at 820 nm.^[175] The prepared photodiode has been deployed in a white light communication system (Figure 12d) and works as a light signal receiver with the bandwidth capability of 1 MHz, as shown in Figure 12e. Further, photodiodes with the structure of ITO/PTAA/MAPbI₃/F8IC:PTB7-Th/C₆₀/BCP/Cu achieve the spectral response up to 1000 nm, an EQE of ≈54% at 850 nm wavelength, a fall time of 5.6 ns (the device area of 0.1 mm²).^[176] In addition, photodiodes had been demonstrated in the single-pixel visible-NIR imaging system (Figure 12f). The chemical formulas and structural formulas of organic materials mentioned above are summarized in Figure 13 as follows.

In addition to organic macromolecular polymers, narrow-bandgap organic dyes have also been utilized to blend with perovskite for solution-processed NIR PDs. By mixing perovskite with CyPF₆ or Cy1BF₄, Laura M. Herz and co-workers achieved broadband perovskite-based PDs with the short-wavelength infrared detection up to around 1.6 μm.^[53] To determine the optimal ratio of perovskite and narrow-bandgap organic dyes, the absorption of perovskite: CyPF₆ composite films with different blend ratios was conducted, as shown in Figure 14a. The composite film shows the increased absorption with the increment of the dye content, while it displays the weak and broadened absorption at 500–750 nm wavelength when the dye content increases to the ratio of 3:1. Notably, composite films with high dye contents would result in the reduced crystallinity or crystallite sizes of perovskites, which possibly deteriorate the charge transport property. Optimized photodiodes based on perovskite: CyPF₆ (2:1) achieve the spectral detection range from visible up to 1100 nm (Figure 14d), meanwhile PDs have

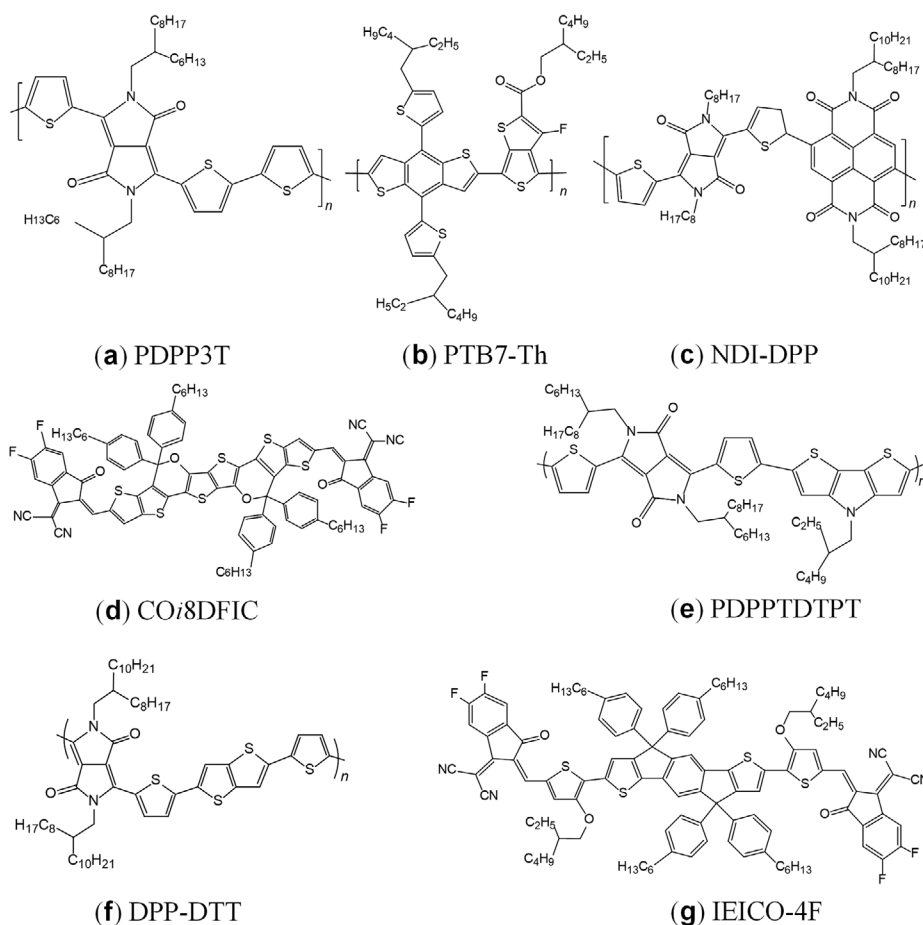


Figure 13. The structural formula of a) PDPP3T,^[50,172] b) PTB7-Th,^[176] c) NDI-DPP,^[173] d) CO8DFIC,^[202] e) PDPPTDTP,^[51] f) DPP-DTT,^[202] and g) IEICO-4F,^[174] which are adopted to combine with perovskite to broaden the spectral response range of Pb perovskite-based PDs.

the dark current density of 10 nA cm^{-2} (Figure 14b), a NEP of $\approx 1.5 \text{ nW Hz}^{1/2}$ and a detectivity of $2 \times 10^8 \text{ Jones}$ at 900 nm wavelength in the photovoltaic mode. Optimized photodiodes

based on perovskite: Cy1BF_4 (2:1) extend the spectral response to $1.6 \mu\text{m}$ (Figure 14e), and present the high dark current density of $2 \mu\text{A cm}^{-2}$ (Figure 14c), a NEP of $\approx 17 \text{ nW Hz}^{1/2}$ and a detectivity

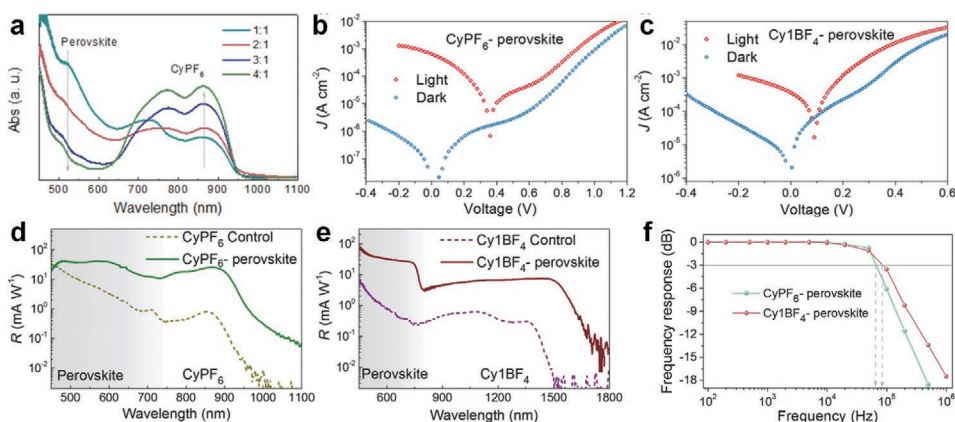


Figure 14. a) Normalized absorption spectra of perovskite: CyPF_6 thin films with different blend ratios. b) Current density–voltage curves of PDs based on perovskite: CyPF_6 . c) Current density–voltage curves of PDs based on perovskite: Cy1BF_4 . d) Wavelength-dependent responsivity comparison of PDs based on CyPF_6 and perovskite: CyPF_6 . e) Wavelength-dependent responsivity comparison of PDs based on Cy1BF_4 and perovskite: Cy1BF_4 . f) Typical frequency response of PDs based on perovskite: Cy1BF_4 and perovskite: CyPF_6 . Reproduced with permission.^[53] Copyright 2017, Wiley-VCH.

of 2×10^7 Jones at 1.5 μm wavelength in the photovoltaic mode. In addition, as shown in Figure 14f, perovskite: CyPF_6 PDs and perovskite: Cy1BF_4 PDs show the -3 dB bandwidth of 65 and 85 kHz, respectively.

4.3.3. Pb Perovskites Incorporated with Upconversion Materials

Through the multi-photon absorption process of multiple excited states, upconversion materials can absorb NIR light and then emit UV–vis light. Therefore, the combination with upconversion materials can efficiently enable Pb perovskite-based PDs to obtain NIR response capability. Shengzhong Frank Liu and co-workers adopted $\text{NaYF}_4:\text{Yb}/\text{Er}$ upconversion nanoparticles (the mean particle size of 20–30 nm) to extend the photodetection region of Pb perovskite photoconductors to ≈ 1100 nm wavelength.^[67,191] They grew MAPbI_3 microarrays on the PET substrate followed by spin-casting a 20–30 nm thick capping layer of $\text{NaYF}_4:\text{Yb}/\text{Er}$ nanoparticles to produce $\text{NaYF}_4:\text{Yb}/\text{Er}/\text{MAPbI}_3$ layered photoconductors with top gold electrodes.^[67] The capping $\text{NaYF}_4:\text{Yb}/\text{Er}$ layer transfers the strong NIR absorption at 850–1033 nm wavelength to the light emission at 400–670 nm wavelength and moderately decreases reflectivity in the visible region compared with the neat perovskite microarrays. Moreover, $\text{NaYF}_4:\text{Yb}/\text{Er}$ layer passivates the underlayer perovskite for the increased photocarrier lifetime, and importantly shows the superior hydrophobic nature for the inhibition of water attack to underlayer perovskite. $\text{NaYF}_4:\text{Yb}/\text{Er}/\text{MAPbI}_3$ layered photoconductors achieve a responsivity of 0.27 A W^{-1} , an EQE of 48%, and a specific detectivity of 0.76×10^{12} Jones (inferred from shot noise determined by the dark current) at

980 nm wavelength (Figure 15a). The $I_{\text{light}}/I_{\text{dark}}$ ratio remains virtually unchanged after PDs are flexed for 2000 times at an angle of 60° , suggesting the excellent flexibility and the robust bending durability. The long-term environmental stability shows that $\text{NaYF}_4:\text{Yb}/\text{Er}/\text{MAPbI}_3$ layered PDs increase the stability with respect to neat perovskite PDs, and their responsivity and detectivity decline around 30% after being exposed under ambient conditions with 30–40% relative humidity for 1000 h (Figure 15b). Anlian Pan and co-workers introduced single-crystalline erbium ytterbium silicate (EYS) nanosheets (the size up to a few tens of micrometers and the thickness of ≈ 400 nm) followed by the deposition of the MAPbI_3 layer (the thickness of ≈ 190 nm) to fabricate EYS/perovskite layered PDs with lateral gold contacts to perovskite.^[54] The underlayer EYS can emit upconversion visible light under the illumination of NIR light, and simultaneously act as the microscale waveguide cavity to confine and propagate the emitted upconversion light. As illustrated by the schematic diagram of optical absorption and corresponding simulation of E-field intensity distribution in Figure 15c, the waveguide cavity can reflect and redirect upconversion visible photons to EYS/perovskite interfaces, resulting in NIR-induced visible photons absorbed by perovskite and contributing to the photocurrent. Consequently, waveguide PDs exhibit the NIR response at the communication wavelength with a low responsivity of 0.012 mA W^{-1} under 1530 nm wavelength illumination at a low bias of 0.1 V (Figure 15d). Recently, Yu He, Qiushui Chen, Huanghao Yang, and co-workers innovatively fabricated an upconversion nanoparticles–perovskite nanotransducer for broadband photodetection spanning from X-rays to NIR.^[203] The novel nanotransducer has the core–shell structure of lanthanide-doped upconversion

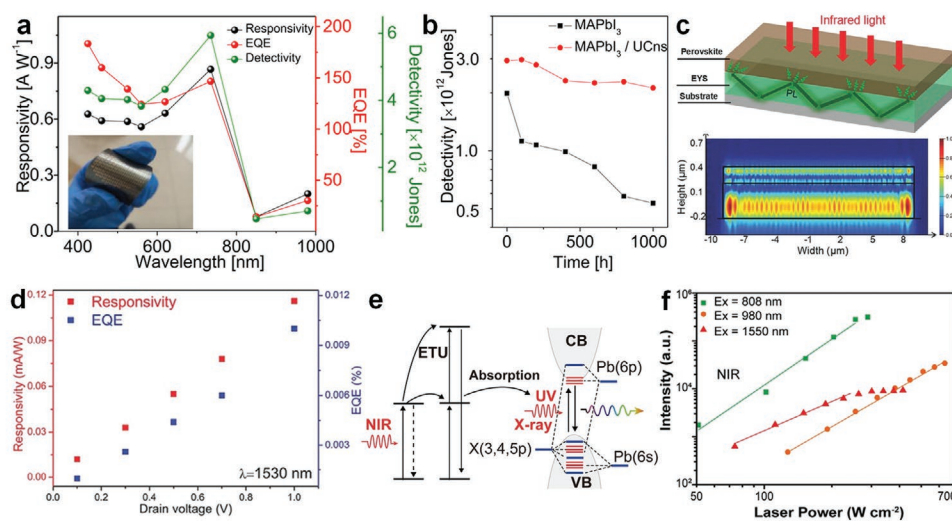


Figure 15. a) Responsivity, EQE and detectivity of $\text{NaYF}_4:\text{Yb}/\text{Er}/\text{MAPbI}_3$ layered photoconductors. The insert exhibits the flexibility of layered devices. b) The long-term environmental stability of $\text{NaYF}_4:\text{Yb}/\text{Er}/\text{MAPbI}_3$ layered photoconductors and neat MAPbI_3 photoconductors. c) Optical absorption principle diagram and E-field intensity distribution simulation (550 nm wavelength) of EYS/perovskite layered PDs. d) Responsivity and EQE of PDs with different drain voltage at 1530 nm wavelength (0.14 W cm^{-2}). e) After being exposed to NIR, lanthanide-doped upconversion nanoparticles emit UV–vis light through energy-transfer upconversion (ETU) processes, and then induce re-absorption processes from lanthanide nanoparticles to perovskite nanodots. f) Photodetection performance of lanthanide–perovskite nanotransducers at 808, 980, and 1550 nm wavelength. a,b) Reproduced with permission.^[67] Copyright 2017, American Chemical Society. c,d) Reproduced with permission.^[54] Copyright 2017, Wiley-VCH. e,f) Reproduced with permission.^[203] Copyright 2021, Wiley-VCH.

nanoparticles@mesoporous silica@MAPbX₃ (X = Cl, Br, or I), in which upconversion nanoparticles are the core and mesoporous silica is the shell incorporated with MAPbX₃ nanodots. After being exposed to NIR, core upconversion nanoparticles absorb NIR photons, then produce UV and blue emission to activate MAPbBr₃ nanodots by the re-absorption process (Figure 15e). Furthermore, by replacing the component of core upconversion nanoparticles, the nanotransducer can detect NIR-I and NIR-II photons at 808, 980, and 1550 nm wavelength. Their corresponding luminescence intensity by multiphoton upconversion could be tuned through the power density of incident NIR photons (Figure 15f).

Lanthanide upconversion nanocrystals generally present the lower luminescent quantum efficiency from NIR to UV–vis light due to the anti-Stokes nature, which result in a relatively high pumping threshold to realize detectable upconversion luminescence accompanied by the low NIR responsivity of PDs. Wen Xu, Hongwei Song, and co-workers introduced a cascade optical field modulation strategy combining the superlensing effect of polymeric microlens arrays and the plasmonic effect of gold nanorods to significantly boost upconversion luminescence with the enhanced ratio of more than four orders of magnitude.^[164,204] Core-shell-shell-structured NaYF₄:Yb³⁺, Er³⁺@NaYF₄@NaYF₄:Yb³⁺, Nd³⁺, Tm³⁺ upconversion nanocrystals were employed to sense 808, 980, and 1540 nm wavelength, respectively. Resultant MAPbI₃/upconversion nanocrystals layered photoconductors with top silver electrodes achieve the responsivity of 30.73, 23.15, and 12.20 A W⁻¹; the EQE of 4726%, 2935%, and 984%; the detectivity (inferred from shot noise determined by the dark current) of 5.36 × 10¹¹, 3.45 × 10¹¹, and 1.92 × 10¹¹ Jones for 808, 980, and 1540 nm wavelength, respectively. Besides, photoconductors have the rise/fall time in the range of 80–120 ms, and exhibit the degraded photocurrent with ≈45% loss after 90-day continuous illumination.^[164]

4.3.4. Pb Perovskites as Functional Layers

In addition to acting as photoactive materials, perovskites have also been utilized as functional layers in surface passivation of NIR QDs. PbS QDs have been proved to be an ideal material for NIR photodetection, however, their nature of massive grain boundaries and long-chain lengths of organic ligands generally result in the low carrier mobility and decreased carrier diffusion lengths. Longfei Mi, Yang Jiang and co-workers employed MAPbI₃ perovskites as a ligand of PbS QDs via a solid-state ligand exchange method to produce broadband Au/MAPbI₃@PbS QDs/Au photoconductors.^[186] The synergistic light absorption of MAPbI₃@PbS QDs covering vis–NIR regions and the effective surface passivation of PbS QDs due to the lattice match between perovskites and PbS QDs contribute to the enhanced spectral response at 300–1200 nm wavelength and a high EQE of around 80% within 600–900 nm wavelength (Figure 16a). The typical type II band alignment between MAPbI₃ and PbS QDs promotes the carrier separation at the contact interface, together with the effective surface passivation, which thus enable PDs with a rise/fall time of 2/23.8 μs (Figure 16b) and a –3 dB bandwidth of 1 MHz. In addition, perovskite-modified PbS QDs-based photoconductors achieve a noise current of less than 1 pA Hz^{-1/2} and a high detectivity up to 10¹⁵ Jones (inferred from the measured noise) at 800 nm wavelength.

Perovskites were utilized as functional layers in optical-field modulation. Germanium is a common photodetection material in optical interconnection due to the spectral absorption in the infrared telecommunication band and its great compatibility with CMOS technology. However, its high refractive index of around 4.0 would partially reflect the incident infrared light and cause a significant portion of light loss, which thus decrease the photocurrent of PDs. Besides, germanium-based PDs have the poor response performance in the visible region owing to the short visible-light penetration length and low photogenerated

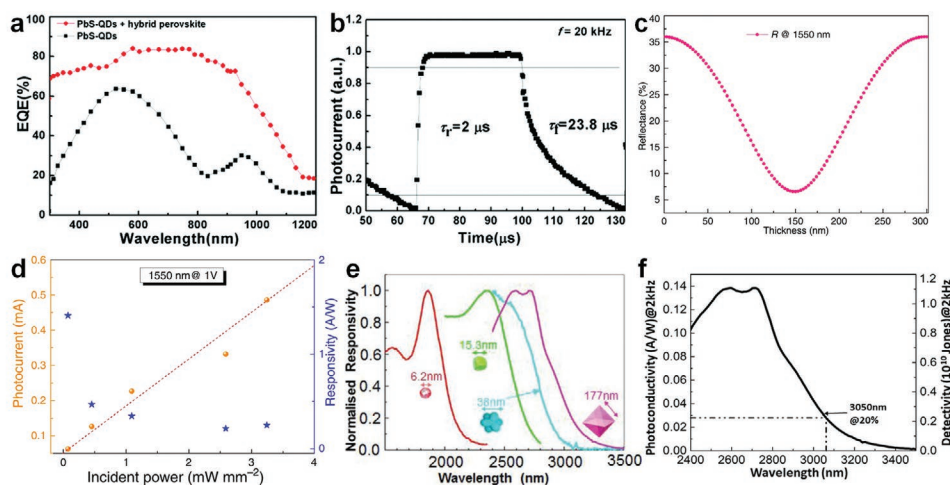


Figure 16. a) Wavelength-dependent EQE of PDs based on PbS QDs and perovskite@PbS QDs. b) A normalized switching cycle of PDs based on perovskite@PbS QDs. c) Reflectance of perovskite films with different thickness at 1550 nm wavelength. d) Irradiance-dependent photocurrent and responsivity at 1550 nm wavelength under the operation of 1 V. e) Normalized responsivity spectra of PbS nanocrystals with different sizes and shapes. f) Wavelength-dependent responsivity and detectivity of PDs based on bulk-like PbS. a, b) Reproduced with permission.^[186] Copyright 2020, The Royal Society of Chemistry. c, d) Reproduced with permission.^[205] Copyright 2019, Springer Nature. e, f) Reproduced with permission.^[13] Copyright 2019, Wiley-VCH.

carrier collection efficiency. To overcome these difficulties and fabricate efficient germanium-based broadband PDs, Chunlai Xue and co-workers deposited a MAPbI₃ film atop a germanium layer (300 nm thickness) working simultaneously as the antireflection layer and the complementary absorption layer of visible light to form germanium/perovskite heterojunction photoconductors.^[205] Through theoretical simulation (Figure 16c) and experimental results, the thickness of the perovskite layer was optimized to 150 nm with the lowest reflectance of 7% at a telecommunication wavelength of 1550 nm. Optimized photoconductors possess the 1/*f* noise feature, a responsivity of 1.4 A W⁻¹ (Figure 16d), a specific detectivity of 10⁸ Jones, and a rise/fall time of 2.1/5.7 ms at 1550 nm wavelength, respectively.

Non-Pb perovskite K₃BiI₆ was utilized as an epitaxial ligand shell of PbS QDs in infrared devices. Although PbS QDs have been widely used in NIR PDs, the quantum confinement in these QDs would cause the blue shift in the absorption spectrum and thus limit their spectral response at longer infrared wavelengths with respect to that of commercial bulk PbS PDs. To approach the cut-off response wavelength of bulk PbS PDs, Wolfgang Heiss and co-workers employed a disubstituted thiourea sulfur precursor to slow down the nucleation rate and thus grew relatively large-size PbS nanocrystals (the tunable average diameter between ≈6 nm and ≈170 nm), suggesting infrared detection in longer wavelengths (Figure 16e).^[13] More importantly, they introduced perovskite K₃BiI₆ as an epitaxial ligand shell, in which K element has the minimal NIR vibrational absorption with respect to common organic cations. Resultant photoconductors with the active layer thickness of 5 μm achieve the responsivity of 20% at 3050 nm wavelength, the peak responsivity of ≈0.12 A W⁻¹ at 2600 nm wavelength (Figure 16f), and a -3 dB bandwidth of 5030 Hz.

5. Sn Perovskite-Based Near-Infrared Photodetectors

Compared with hybrid Pb-based perovskites, non-toxic Sn-based perovskites that simply substitute Pb²⁺ with Sn²⁺ show the narrower bandgap and thus could be employed as photoactive layers in NIR PDs.^[37,206,207] Nevertheless, natural oxidation of Sn²⁺ to Sn⁴⁺ states in Sn-based perovskites would induce p-type self-doping, which turns semiconducting perovskites

to metal-like ones.^[56,104,208–211] This behavior would induce the high carrier concentration, decrease carrier lifetime and diffusion length, and thus result in the poor performance of Sn-contained perovskite-based devices.^[57,212–214] To pursue efficient NIR PDs, some approaches for suppressing the oxidation of Sn²⁺ states in Sn-based perovskites and corresponding photo-detection performances will be discussed. The current progress of Sn perovskite-based NIR devices is summarized in Table 5.

Zhiyong Fan and co-workers grew an array of 3D MASnI₃ nanowires in a porous alumina template by electrochemically depositing Sn on the bottom of the template and subsequently reacting with MAI vapor under the protection of argon at 170 °C (Figure 3c).^[37] Fabricated MASnI₃ nanowires with the cubic crystal structure have a diameter of 250 nm and a period of 500 nm. Moreover, the nanowires have the bandgap of 1.3 eV and show the broad spectral absorption at 300–1000 nm wavelength. Prepared nanowire-based photoconductors with the device structure of Al/MASnI₃ nanowires/Au (Figure 17a) achieve a responsivity of up to 0.47 A W⁻¹, a corresponding detectivity of 8.80 × 10¹⁰ Jones (inferred from shot noise determined by the dark current), and a rise/fall time of 1500/400 ms. Importantly, sidewalls of the alumina template could effectively obstruct lateral permeation pathways of foreign oxygen and water molecules, and thus greatly improve the environmental tolerance of MASnI₃ and resultant devices. Specifically, when exposed to the air with 70% humidity, nanowire-based PDs show the decreased photocurrent from 19.8 to 2.7 μA after 7-day storage (Figure 17b), while thin-film-based PDs present the reduced value to zero just after 30-min storage, suggesting significantly improved device stability for template-protective MASnI₃ nanowires. Similarly, Liang Li and co-workers adopted one-step antisolvent washing to deposit CsSnI₃ within TiO₂ nanorod arrays (the average height is ≈1.8 μm and the diameter is ≈100 nm) and subsequently spin-coated a poly(3-hexylthiophene-2,5-diyl) (P3HT) layer to fabricate broadband photodiodes with the spectral range of 350–1000 nm (Figure 17c).^[35] TiO₂ nanorod arrays and P3HT serve as the electron and hole transport layer, respectively. Importantly, they found that ascorbic acid could be used as a reducing agent to inhibit the oxidation of Sn²⁺ to Sn⁴⁺. By optimizing the concentration of ascorbic acid to 10 mol%, CsSnI₃ films could be stored stably for more than 1 day in the air with the humidity of ≈80%. TiO₂/CsSnI₃/P3HT hybrid photodiodes present a responsivity of 0.257 A W⁻¹ and

Table 5. Figures of merit and current progress of Sn perovskite-based NIR devices.

Photoactive materials	Spectral range [nm]	Responsivity [mA W ⁻¹]	Specific detectivity [Jones]	<i>t</i> _{rise} / <i>t</i> _{fall} [ms]	Ref.
Photodiodes					
3D MASnI ₃ nanowire array	200–1000	470	8.8 × 10 ^{10a)}	1.5 × 10 ³ /4 × 10 ²	[37]
CsSnI ₃	350–1000	257 @ 850 nm	1.5 × 10 ¹¹ @ 850 nm ^{a)}	0.35/1.6	[35]
Photoconductors					
CsSnI ₃ nanowire array	475–940	54 @ 940 nm	3.85 × 10 ⁵ @ 940 nm ^{a)}	83.8/243	[206]
Phototransistors					
FASnI ₃	300–1000	≈2 × 10 ⁸ @ 850 nm	3.2 × 10 ^{12b)}	1.17 × 10 ⁵ /2.06 × 10 ⁵	[36]

^{a)}The specific detectivity of the corresponding device was inferred from the dark current; ^{b)}The specific detectivity of the corresponding device was calculated by the measured noise.

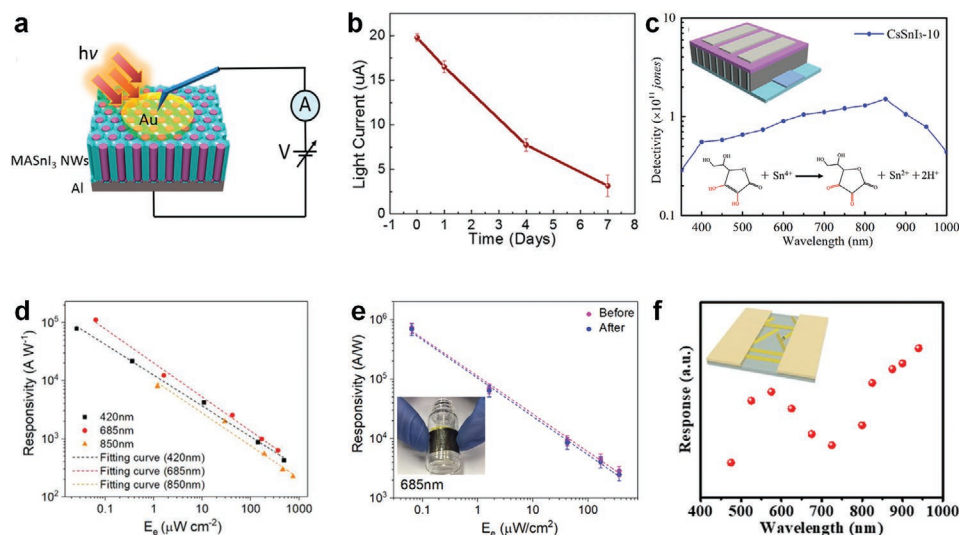


Figure 17. a) Device structure diagram of PDs based on 3D MASnI₃ nanowire arrays. b) Light current of PDs based on 3D MASnI₃ nanowire arrays over time. c) Wavelength-dependent detectivity of PDs based on CsSnI₃ with 10 mol% ascorbic acid (CsSnI₃-10) at 10 mV (the insert top image is the device structure, the bottom is the chemical equation of reduction reaction). d) Light intensity-dependent responsivity of PDs based on FASnI₃ at different wavelengths of 420, 685, and 850 nm. e) Light intensity-dependent responsivity of flexible PDs based on FASnI₃ before and after the bending test (the insert image shows the bending test on a bottle with a radius of 8 mm). f) Response of PDs based on CsSnI₃ nanowire arrays (the insert image is device structure). a, b) Reproduced with permission.^[37] Copyright 2016, American Chemical Society. c) Reproduced with permission.^[35] Copyright 2020, Wiley-VCH. d) Reproduced with permission.^[207] Copyright 2019, Wiley-VCH. e) Reproduced with permission.^[36] Copyright 2020, American Chemical Society. f) Reproduced with permission.^[206] Copyright 2019, American Chemical Society.

a detectivity of 1.5×10^{11} Jones (inferred from shot noise determined by the dark current) at 850 nm wavelength.

Feng Yan and co-workers introduced hydroxybenzene sulfonic acid additive along with excessive SnCl₂ in the growth process of FASnI₃ to significantly improve the antioxidant capacity of Sn-based perovskites.^[36,207] FASnI₃ thin films achieve the absorption edge at ≈ 890 nm wavelength, the hole mobility of ≈ 19 cm² V⁻¹ s⁻¹, and the carrier concentration of $\approx 4.6 \times 10^{16}$ cm⁻³. FASnI₃-based photoconductors with the device structure of Au/FASnI₃ (120 nm thickness)/Au present the ultrahigh responsivity and gain (Figure 17d), which was expected from the selective trapping of photogenerated carriers by defect states.^[207] They also grew FASnI₃ on polyimide substrates to demonstrate its flexibility and resultant devices remained the responsivity after 300 bending cycles at a radius of about 8 mm (Figure 17e). Zai-xing Yang and co-workers adopted a solid-source chemical vapor deposition method to grow Pb-free CsSnX₃ (X = Cl, Br, and I) nanowire arrays on mica substrates, among which the bandgap of CsSnI₃ was 1.34 eV.^[206] NIR photoconductors with the structure of Au/CsSnI₃ nanowire arrays/Au achieve a broad spectral response range at 475–940 nm wavelength (Figure 17f), a responsivity of 54 mA W⁻¹ and a low specific detectivity of 3.85×10^5 Jones (inferred from shot noise determined by the dark current) at 940 nm wavelength.

6. Sn–Pb Mixed Perovskite-Based Near-Infrared Photodetectors and Imaging Arrays

The bandgap of Sn–Pb mixed perovskites can be lower than that of pristine Pb-based ones (≈ 1.55 eV for MAPbI₃) and

Sn-based ones (≈ 1.30 eV for MASnI₃), which could reach as low as ≈ 1.17 eV and exhibit the desirable NIR absorption to ≈ 1060 nm wavelength.^[26,55] Moreover, compared to pure Sn-based perovskites, mixed Sn–Pb perovskites experimentally gain the higher stability.^[215] According to time-domain DFT combined with nonadiabatic molecular dynamics, Sn–Pb mixed perovskites with the Sn incorporation could localize hole states and form hole polaron-like system, which thus delay the carrier nonradiative recombination and prolong the carrier lifetime. Interestingly, with the increase of the Sn content, Sn–Pb mixed perovskites possess small polarons to large polarons, indicating reduced trap-assisted recombination.^[146,147] Therefore, Sn–Pb mixed perovskite-based PDs and imaging arrays with the high Sn content of ≈ 50 – 60% have been studied and will be discussed below.^[33,34,216,217,220,221] The current progress of these devices is summarized in **Table 6**.

Dewei Zhao, Fujun Zhang, Yanfa Yan, and co-workers adopted Sn–Pb mixed perovskite (FASnI₃)_{0.6}(MAPbI₃)_{0.4} with the narrow bandgap of ≈ 1.25 eV to fabricate highly sensitive broadband photodiodes from 300 to 1000 nm wavelength.^[216] They employed the transfer matrix method to study the optical field distribution of photodiodes and found that devices would have the enhanced interference effect for long-wavelength light (>650 nm) and thus harvest more incident NIR photons with the increase of the perovskite thickness. Experimentally, increased thickness of the active layer from 400 to 1000 nm efficiently contributes to the increased EQE value in the NIR region (Figure 18a), and simultaneously reduces the dark current. Optimized photodiodes with the structure of ITO/PEDOT:PSS/(FASnI₃)_{0.6}(MAPbI₃)_{0.4} (1000 nm thickness)/C₆₀ (70 nm)/BCP (5 nm)/Ag present an almost flat spectral range from 700 to 900 nm with EQE exceeding 65%, a dark

Table 6. Figures of merit and current progress of Sn–Pb mixed perovskite-based NIR devices.

Photoactive materials	Spectral range [nm]	Responsivity [mA W^{-1}]	Specific detectivity [Jones]	EQE	$f_{-3\text{dB}}$ [kHz]	LDR [dB]	$t_{\text{rise}}/t_{\text{fall}}$ [μs]	Ref.
Photodiodes								
$\text{FA}_{0.85}\text{Cs}_{0.15}\text{Sn}_{0.5}\text{Pb}_{0.5}\text{I}_3$	600–1000	530 @ 940 nm	6×10^{12} @ 940 nm ^{b)}	$\approx 80\%$ @ 760–900 nm 70% @ 940 nm	–	103 ^{d)}	$5.83 \times 10^{-2}/0.86$	[24]
$(\text{FASnI}_3)_{0.6}(\text{MAPbI}_3)_{0.4}$	300–1000	400 @ 950 nm	1.1×10^{12} @ 900 nm ^{b)}	$>65\%$ @ 350–900 nm	–	167 ^{c)}	6.9/9.1	[216]
$\text{MA}_{0.5}\text{FA}_{0.5}\text{Pb}_{0.5}\text{Sn}_{0.5}\text{I}_3$	350–1000	>200 @ 800–950 nm	$>10^{12}$ @ 800–970 nm ^{b)}	$\approx 10\%$ @ 800 nm	100	–	–	[34]
$\text{MA}_{0.975}\text{Rb}_{0.025}\text{Sn}_{0.65}\text{Pb}_{0.35}\text{I}_3$	300–1100	400 @ 910 nm	$>10^{12}$ @ 340–1000 nm ^{b)}	–	1000	110 ^{d)}	0.040/0.468	[25]
$\text{MASn}_x\text{Pb}_{1-x}\text{I}_3$	300–1100	200 @ 940 nm	$>10^{11}$ @ 360–985 nm ^{b)}	$>20\%$ @ 780–970 nm	–	100 ^{c)}	0.090/2.27	[218]
$(\text{FASnI}_3)_{0.6}(\text{MAPbI}_3)_{0.4}$	300–1000	–	$\approx 10^{11}$ @ 850 nm ^{a)}	$>45\%$ @ 850 nm	–	–	$1.9 \times 10^4/1.3 \times 10^4$	[219]
$\text{CsPb}_{0.5}\text{Sn}_{0.5}\text{I}_3$ (5% (PEA) ₂ Pb _{0.5} Sn _{0.5} I ₄)	700–900	270 @ 850 nm	5.42×10^{14} @ 850 nm ^{b)}	–	543	–	–	[220]
$\text{MA}_{0.5}\text{FA}_{0.5}\text{Pb}_{0.5}\text{Sn}_{0.5}\text{I}_3$ (2.5% (PEA) ₂ Pb _{0.5} Sn _{0.5} I ₄)	700–1000	≈ 100 @ 800 nm	$\approx 1.6 \times 10^{12}$ @ 800 nm ^{a)}	$\approx 14\%$ @ 800 nm	52	–	10/10	[221]
$\text{Cs}_{0.05}\text{MA}_{0.45}\text{FA}_{0.5}\text{Pb}_{0.5}\text{Sn}_{0.5}\text{I}_3$	300–1050	530 @ 910 nm	2.07×10^{11} @ 910 nm ^{b)}	–	–	–	0.035	[33]
$\text{FA}_{0.5}\text{MA}_{0.45}\text{Cs}_{0.05}\text{Pb}_{0.5}\text{Sn}_{0.5}\text{I}_3$	300–1050	350 @ 950 nm	2.21×10^{11} @ 758 nm ^{b)}	$\approx 40\%$ @ 950 nm	–	185 ^{c)}	–	[217]
Phototransistors								
$(\text{FASnI}_3)_{0.6}(\text{MAPbI}_3)_{0.4}$	500–1100	44.72 @ 900 nm 12.89 @ 1100 nm	2.24×10^{10} @ 900 nm ^{a)}	–	–	–	$2 \times 10^4/4 \times 10^4$	[222]
$\text{CsSn}_{0.6}\text{Pb}_{0.4}\text{I}_{2.6}\text{Br}_{0.4}$	454–860	2.1×10^4 @ 860 nm	3.9×10^{10} @ 860 nm ^{a)}	–	–	25 ^{c)}	$7.35 \times 10^5/5.58 \times 10^5$	[223]

^{a)}The specific detectivity of the corresponding device was inferred from the dark current; ^{b)}The specific detectivity of the corresponding device was calculated by the measured noise; ^{c)}The formula coefficient of LDR was 20; ^{d)}The formula coefficient of LDR was 10.

current of 3.9 nA, a LDR up to 167 dB (the coefficient of LDR is 20), and a NEP of $1.9 \times 10^{-13} \text{ W Hz}^{1/2}$ and a detectivity of $\approx 10^{12}$ Jones at 900 nm (Figure 18b). Besides, unencapsulated devices remain 96% of the initial photocurrent after 90-day storage

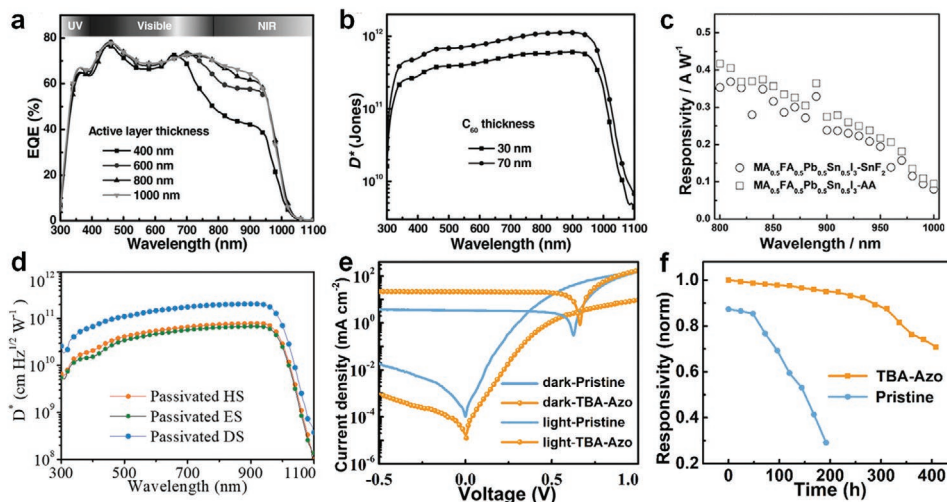


Figure 18. a) Wavelength-dependent EQE of PDs with different perovskite layer thicknesses at -0.2 V bias. b) Wavelength-dependent detectivity of PDs with different C_{60} layer thicknesses at -0.2 V bias. c) Responsivity comparison of PDs with different additives. d) Detectivity comparison of PDs with different passivation methods. e) Current density–voltage curves comparison of PDs with and without TBA-Azo passivation. f) Stability comparison of PDs with and without TBA-Azo passivation in the air. a, b) Reproduced with permission.^[216] Copyright 2017, Wiley-VCH. c) Reproduced with permission.^[34] Copyright 2017, Wiley-VCH. d) Reproduced with permission.^[33] Copyright 2020, Wiley-VCH. e, f) Reproduced with permission.^[217] Copyright 2021, Elsevier Ltd.

in a N₂-filled glove box. Earlier, Alex K.-Y. Jen and co-workers introduced an antioxidant additive (i.e., ascorbic acid) to suppress the oxidation of Sn²⁺ states in MA_{0.5}FA_{0.5}Pb_{0.5}Sn_{0.5}I₃ and thus fabricated broadband photodiodes with the spectral detection ranging from 350 to 1000 nm.^[34] The incorporation of ascorbic acid could retard the formation of Sn vacancy and facilitate the film formation, originating from the Lewis base of the counter anion of ascorbic acid that modulates the crystallization kinetics and passivates the associated Sn-derived defects. Compared with the widely-used SnF₂, photodiodes with ascorbic acid show the larger interfacial carrier recombination resistance and the lower leakage current. With the structure of ITO/PEDOT:PSS/MA_{0.5}FA_{0.5}Pb_{0.5}Sn_{0.5}I₃/PC₆₁BM/bis-C₆₀/Ag, photodiodes achieve a high responsivity of over 0.2 A W⁻¹ (Figure 18c), a detectivity of 10¹² Jones (inferred from the measured noise) at 800–970 nm wavelength, and a –3 dB bandwidth of around 100 kHz.

Liang Shen and co-workers adopted a two-sided passivation strategy by inserting PEAI to both top and bottom sides of Cs_{0.05}MA_{0.45}FA_{0.5}Pb_{0.5}Sn_{0.5}I₃ layers to stabilize Sn–Pb mixed perovskites.^[33] The larger organic cation PEA⁺ on the top of Sn–Pb mixed perovskites facilitates the formation of a 2D perovskite capping layer (PEA₂PbI₄), which prevents the penetration of water and oxygen. The bottom insertion layer could not only reduce the residual PbI₂ content on the bottom perovskite and inhibit the generation of iodine vacancies, but also promote the crystallization through the suspension bond of PEA⁺. Compared to the one-sided passivation, optimized Sn–Pb mixed perovskite photodiodes with two-sided passivation achieve a reduced dark current density of 1.25 × 10⁻⁶ A cm⁻² at –0.1 V, an increased responsivity of 0.53 A W⁻¹ and an increased detectivity of around 10¹¹ Jones (inferred from the measured noise) at 910 nm wavelength (Figure 18d). Importantly, under the 100 mW cm⁻² illumination with 55 °C temperature and the relative humidity of 40–70%, devices can keep ≈60% of the initial detectivity after 260-h continuous operation. Very recently, they introduced an azobenzene derivative, that is, 3,4,5-tris(*n*-dodecyloxy) benzoylamide with an azobenzene moiety (TBA-Azo) to passivate the top of Cs_{0.05}MA_{0.45}FA_{0.5}Pb_{0.5}Sn_{0.5}I₃ and demonstrated remarkably stable Sn–Pb mixed perovskite-based photodiodes.^[217] TBA-Azo comprises the azobenzene moiety and three long alkyl chains at ends. The lone pair electrons of N = N and C–N of azobenzene moiety in TBA-Azo could passivate undercoordinated Pb²⁺ at perovskite surfaces and grain boundaries, which thus dramatically inhibit the nonradiative recombination of carriers, result in a low noise current and fast response speed. The long carbon chains possess hydrophobic properties to enhance stability. Prepared TBA-Azo-treated photodiodes achieve responsivities of 0.45 A W⁻¹ at 770 nm wavelength and of 0.35 A W⁻¹ at 950 nm wavelength, a low dark current of 9.61 × 10⁻⁸ A cm⁻² at –0.1 V (Figure 18e), a noise current of 0.42 pA Hz^{-1/2}, a LDR of 185 dB (the coefficient of LDR is 20), and a detectivity of 2.21 × 10¹¹ Jones. More importantly, TBA-Azo-treated devices remain 90% of original responsivity after ≈300-h storage in the air (Figure 18f), and maintain the initial performance after 3-month storage in a glove box.

Wallace C. H. Choy and co-workers have devoted extensive works in the crystallization kinetics of Sn–Pb mixed perovskites

and developing their efficient NIR photodiodes and imaging arrays.^[24,25,218] They introduced Rb cations to MA Sn-rich Sn–Pb mixed perovskites (the Sn content is 65%) to control crystallization for growing high-quality films.^[25] Interestingly, incorporated Rb can effectively modify surface-energy-induced kinetic process. Ab initio simulation found that Rb incorporation in Sn-rich Sn–Pb mixed perovskites would reduce the surface energy of (110) plane, facilitating the film growth in (110) plane. Moreover, it was expected that Rb incorporation effectively adjusts the orbital interaction between Sn/Pb and I atoms as well as the degree of octahedral tilting of the (Sn/Pb)I₂ frame, which result into the high symmetry (reduced energetic disorder) and thus enhanced crystallinity and strengthened preferred orientation. Consequently, Rb-incorporated MA Sn–Pb mixed perovskites exhibit a lower root mean square roughness of 11.2 nm, a higher texture coefficient of (110) plane relative to (112) plane, reduced potential differences between grain interfaces and interiors, a longer carrier lifetime, and reduced Urbach energy of 16.9 meV. Optimized photodiodes based on MA_{0.975}Rb_{0.025}Sn_{0.65}Pb_{0.35}I₃ exhibit a broad sensitive range of 300–1100 nm wavelength, a large LDR of 110 dB with the incident light intensity from 1.32 pW cm⁻² to 1.05 W cm⁻² (the coefficient of LDR is 10), –3 dB bandwidth of 1 MHz, a rise/fall time of 40/468 ns, a high responsivity of 0.4 A W⁻¹ at 910 nm wavelength, and a flat detectivity of over 10¹² Jones (inferred from the measured noise) between 340 and 1000 nm wavelength (Figure 19a). More importantly, as shown in Figure 19b, encapsulated devices could almost remain photocurrent and dark current after 200-day storage in a glove box. Further, they explored the growth of MA Sn–Pb mixed perovskites and their devices on CMOS-compatible metal/Si-substrates to advance perovskite integration with Si-based electronics.^[218] They proposed and demonstrated the room-temperature crystallization in the Sn-rich Sn–Pb mixed perovskite system to effectively control film crystallization kinetics. Specifically, after being treated by the antisolvent washing, the top of supersaturated precursors favors both the generation of new nuclei and then their rapid completion of crystal growth. Meanwhile, precursors on the bottom may have a relatively lower concentration than that on the top and thus prefer to slowly grow crystals from the pre-existing few nuclei. By controlling the crystallization time, they successfully tune the density and location of nanocrystals in precursor films to achieve compact nanocrystals, which thermally coalesce into high-quality (smooth, dense, and pinhole-free, as shown in Figure 19c) Sn–Pb mixed perovskites with intensified preferred orientation and decreased trap densities. Fabricated photodiodes possess a spectral response range within 300–1100 nm wavelength, a dark current density of 2.8 × 10⁻⁷ A cm⁻², a rise/fall time of 90 ns/2.27 μs, and a detectivity of exceeding 10¹¹ Jones covering 360–985 nm wavelength. Finally, 6 × 6 integrated pixels are constructed to conceptually demonstrate its imaging application (Figure 19d). Very recently, they first introduced thermally stable MA-free FA-Cs Sn–Pb mixed perovskites to realize NIR photodetection.^[24] To achieve sufficient NIR absorption and efficient devices, thick Sn–Pb perovskite films (over 1 μm) are the key prerequisite, which had not been reported in PDs. They proposed an approach of double-side crystallization tuning through the low-temperature space-restricted annealing process to control the crystallization

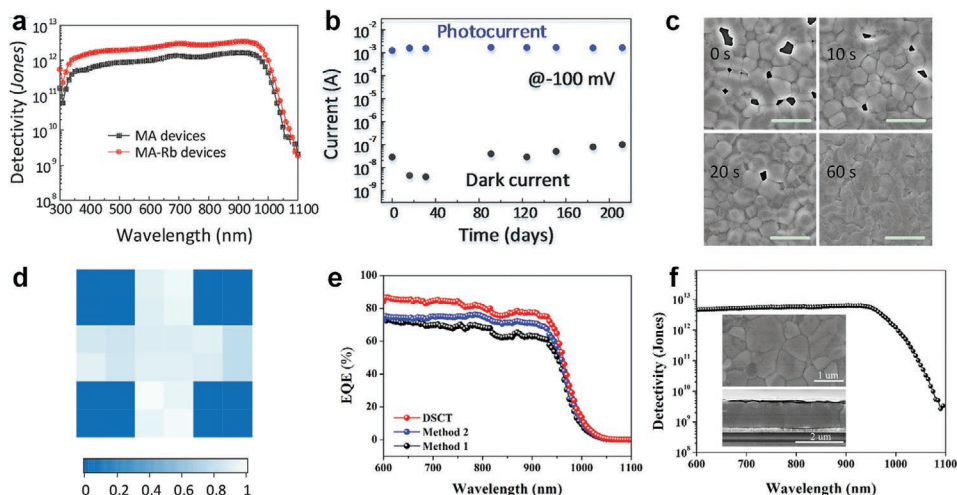


Figure 19. a) Wavelength-dependent detectivity comparison of MA-based and MA-Rb-based photodiodes. b) Photocurrent and dark current stability of MA-Rb-based PDs. c) SEM images of MA Sn–Pb perovskite films under different crystallization times of 0, 10, 20, and 60 s. d) Image of the “+” symbol displayed by the Sn–Pb perovskite-based PDs imaging array with 36 pixels. e) EQE comparison of PDs based on $\text{FA}_{0.85}\text{Cs}_{0.15}\text{Sn}_{0.5}\text{Pb}_{0.5}\text{I}_3$ fabricated by different methods. f) Wavelength-dependent detectivity of PDs based on $\text{FA}_{0.85}\text{Cs}_{0.15}\text{Sn}_{0.5}\text{Pb}_{0.5}\text{I}_3$. The insert are SEM images of FA–Cs Sn–Pb perovskites fabricated by the low-temperature space-restricted annealing method. a,b) Reproduced with permission.^[25] Copyright 2018, Wiley-VCH. c,d) Reproduced with permission.^[218] Copyright 2019, American Chemical Society. e,f) Reproduced with permission.^[24] Copyright 2021, Wiley-VCH.

kinetics. Specifically, the process of space-restricted annealing can preserve the escaped residual solvents and formulate the solvent atmosphere for growing thick precursor films, which retard the crystallization of the top of precursor films. Simultaneously, low-temperature annealing promotes the crystal growth of the bottom of precursor films, which accompanies the release of residual solvents facilitated by the enriched solvent atmosphere. Finally, through the controllable crystallization manner, they achieve smooth (roughness of 29.6 nm), pinhole-free, and void-free FA–Cs Sn–Pb perovskite thick films (1.1 μm thickness) with improved crystallinity, preferred out-of-plane stacking patterns, and low trap density ($4.4 \times 10^{14} \text{ cm}^{-3}$). Optimized photodiodes with the structure of ITO/PEDOT:PSS/ $\text{FA}_{0.85}\text{Cs}_{0.15}\text{Sn}_{0.5}\text{Pb}_{0.5}\text{I}_3$ /PC₆₁BM/ZrAcac/Ag present a high flat EQE of around 80% within 760–900 nm, a recorded responsivity of 0.53 A W^{-1} and a high detectivity of 6×10^{12} Jones at 940 nm wavelength (Figure 19e,f), a low NEP of $47.9 \text{ fW Hz}^{-1/2}$, and a rise/fall time of 58.3 ns/0.86 μs .

Sn–Pb mixed perovskites have been integrated with amorphous indium gallium zinc oxide thin-film transistors (IGZO TFTs) to achieve broadband phototransistors/imaging sensors, which benefit from merits of IGZO TFTs, including the large-area production, low-temperature solution-processability and high field-effect carrier mobility.^[219,222,223] Hang Zhou, Chuan Liu, and co-workers combined $(\text{FASnI}_3)_{0.6}(\text{MAPbI}_3)_{0.4}$ photodiodes with IGZO TFTs to fabricate a 12×12 pixels imaging array through spin-on-patterning method, in which each pixel could be independently controlled by the gate voltage of a TFT (Figure 20a).^[219] Due to its natural hydrophobic characteristic, the perfluoro (1-butenyl vinyl ether) polymer layer (CYTOP) was employed as the encapsulated layer of bottom IGZO TFTs, meanwhile it was etched to pattern top self-assembled Sn–Pb mixed perovskite photodiode arrays (Figure 20b). Patterned photodiodes with the structure of ITO/ SnO_2 / $(\text{FASnI}_3)_{0.6}(\text{MAPbI}_3)_{0.4}$ /P3HT/Au show a spectral response at 300–1000 nm wavelength, an EQE of above 45% and

a detectivity of $\approx 10^{11}$ Jones (inferred from shot noise determined by the dark current) at 850 nm wavelength, and a rise/fall time of 19/13 ms for optical control. In addition, they demonstrated the NIR imaging of number “11” at 850 nm wavelength using fabricated 12×12 pixel arrays (Figure 20c).^[219] Dong-Won Kang, Sung Kyu Park, and co-workers explored a hybrid broadband phototransistor by constructing the heterojunction of Sn–Pb mixed perovskite $\text{CsSn}_{0.6}\text{Pb}_{0.4}\text{I}_{2.6}\text{Br}_{0.4}$ with an IGZO carrier transport layer (Figure 20d).^[223] When exposed to the 40–60% relative humidity at room temperature, $\text{CsSn}_{0.6}\text{Pb}_{0.4}\text{I}_{2.6}\text{Br}_{0.4}$ using Cs cations and Br doping shows an exceptionally stable phase with respect to CsPbI_3 and $\text{MASn}_{0.6}\text{Pb}_{0.4}\text{I}_{2.6}\text{Br}_{0.4}$, potentially suggesting the enhanced stability of hybrid phototransistors. $\text{CsSn}_{0.6}\text{Pb}_{0.4}\text{I}_{2.6}\text{Br}_{0.4}$ achieves a narrow bandgap of 1.36 eV and the absorption onset at ≈ 860 nm wavelength. To restrain the undesired charge transport path and concurrently maintain the light-sensitive channel of Sn–Pb mixed perovskites, they introduced selectively UV-irradiated electrical deactivation, which induce a local destruction of perovskites and thus dark current is reduced by nearly 4 orders of magnitude (Figure 20e). Therefore, Sn–Pb mixed perovskite/IGZO hybrid phototransistors present a broad spectral range from visible to NIR light (≈ 860 nm), a responsivity of 21 A W^{-1} and a detectivity of 3.9×10^{10} Jones (inferred from shot noise determined by the dark current) at 860 nm wavelength, and a rise/fall time of 735/558 ms. Importantly, hybrid devices encapsulated with a PMMA layer exhibit the reduced dark current by about 1 order of magnitude and the decreased photocurrent by around 2 orders of magnitude after 30 days (Figure 20f).

7. Outlook and Summary

Benefiting from the low-cost and facile manufacturability and remarkable photoelectric properties, hybrid halide perovskites have been demonstrated as the ideal photodetection material for

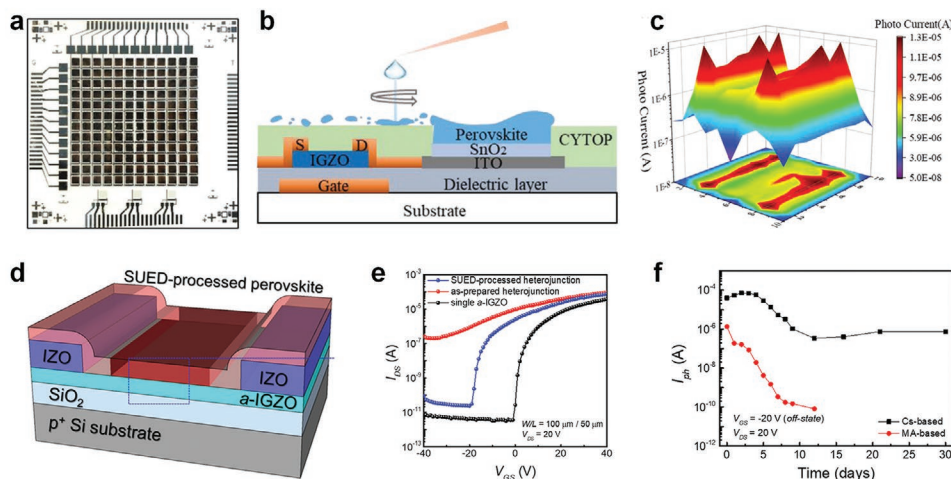


Figure 20. a) The picture of the IGZO TFT array with 12×12 pixels. b) Schematic diagram of perovskite growth on the IGZO TFT array backplane by spin coating method. c) Image of the number “11” obtained by measuring the photocurrent intensity distribution of the pixel array. d) Schematic diagram of the SUED-processed $\text{CsSn}_{0.6}\text{Pb}_{0.4}\text{I}_{2.6}\text{Br}_{0.4}/\text{IGZO}$ phototransistor. e) Transfer characteristic of perovskite/IGZO phototransistors before and after the SUED process. f) Current comparison of phototransistors based on $\text{CsSn}_{0.6}\text{Pb}_{0.4}\text{I}_{2.6}\text{Br}_{0.4}/\text{IGZO}$ and $\text{MASn}_{0.6}\text{Pb}_{0.4}\text{I}_{2.6}\text{Br}_{0.4}/\text{IGZO}$ over time. a–c) Reproduced with permission.^[219] Copyright 2019, Wiley-VCH. d–f) Reproduced with permission.^[223] Copyright 2020, American Chemical Society.

high-efficiency NIR PDs and imaging arrays. Promisingly, some figures of merit of these perovskite-based NIR devices are comparable with that of commercial silicon- and germanium-based NIR devices. More importantly, some key parameters of Sn–Pb mixed perovskite-based devices are even better than that of commercial devices. For instance, Sn–Pb mixed perovskite-based PDs achieve a high responsivity of 0.53 A W^{-1} (corresponding EQE is 70%) at 940 nm wavelength, which is greater than the EQE of rough 10% for common silicon image sensors and also is higher than the 50% EQE of state-of-the-art complicated photon-trapping-structured silicon image sensors.^[128,224] Moreover, Sn–Pb mixed perovskite-based PDs achieve the detectivity of around 10^{12} Jones down to 1000 nm wavelength, which is greater than germanium-based NIR PDs with the value of less than 10^{11} Jones.^[15] To advance perovskite-based NIR PDs and imaging arrays toward commercial applications, further exploration and efforts should be made to address following issues, including spectral response extension to longer wavelengths, the integration of pixel devices, the flexibility and stability of these NIR devices.

7.1. Spectral Response Extension to Longer Wavelengths

Both perovskite/silicon hybrid PDs and Sn–Pb mixed perovskite-based PDs can achieve the response onset to $\approx 1100 \text{ nm}$. Together with mature processing techniques of silicon, the incorporation of Sn–Pb mixed perovskites can not only provide the high NIR absorption coefficient, which effectively reduces the thickness of the photoactive layer and thus increases the incident light angle,^[225] but also enhance the performance in the NIR region due to remarkable photoelectric properties of perovskites. NIR PDs with perovskite/polymer layered heterojunction or perovskite/organic bulk-heterojunction hybrid structure show the detection wavelength of less than $\approx 1100 \text{ nm}$ determined by organic narrow-bandgap

semiconductors. Although perovskite:dye bulk-heterojunction PDs extend the spectral detection range to around $1.6 \mu\text{m}$, devices show the poor performance. Hence, new organic NIR semiconductors with the spectral absorption of longer than 1100 nm could be introduced and explored their roles for efficient NIR PDs. Perovskite/QDs layered heterojunction PDs and perovskite:QDs bulk heterojunction PDs can achieve the response to the optical fiber communication band ($\approx 1550 \text{ nm}$ wavelength) and even to $2.6 \mu\text{m}$ wavelength. Furthermore, perovskite/2D semiconductors PDs have achieved the NIR response to $\approx 1550 \text{ nm}$ wavelength and potentially reach the detection range to longer than $2 \mu\text{m}$.^[226] The tradeoff between the NIR absorption and the photogenerated carrier extraction would limit the performance of perovskite/2D semiconductors PDs. Among these perovskite/narrow-bandgap semiconductors hybrid PDs, the suitable energy-level alignment at the interface of perovskite/narrow-bandgap semiconductors should be carefully considered to efficiently extract light-excited carriers, contributing to efficient photodetection.

7.2. Pixel Integration

As a proof of concept, perovskite-based NIR PDs have been integrated to produce low-density pixel arrays with the pixel number of less than 12×12 and further demonstrated their imaging applications. Due to the long tissue penetration depth of NIR, low-density perovskite-based NIR pixel arrays can be explored their role in personal health monitoring. According to photoplethysmography, low-density NIR pixel arrays can be used to record blood volume changes in the microvascular bed of tissue, which is closely correlated with the information about the cardiovascular system.^[227,228] Further, high-density pixel arrays present broad applications in document scanning, biometric fingerprinting, spectrometers, night vision, commercial image sensors, etc. Pb-based perovskites have been integrated

with a high-resolution thin-film transistor backplane to demonstrate applications in X-ray imaging and optical scanning.^[4,229] Encouragingly, it is desirable to develop efficient high-density pixel arrays with perovskite-based NIR PDs and explore their applications.

7.3. Flexible Near-Infrared Devices

Flexibility of NIR PDs indicates the capability that enable devices work under deformation, which is pivotal for emerging wearable devices. Simulated results suggest that the B–X chemical bond in ABX₃ perovskites determines the elastic properties and perovskites present the low shear modulus, indicating potential uses in flexible devices.^[230] Importantly, microstructure texture of perovskites would largely influence the flexibility.^[231,232] Although Pb-based polycrystalline perovskites have been demonstrated in flexible NIR PDs, the detailed influence of microstructured morphologies, bending radii and device structures of perovskite/NIR materials on the flexibility has been hardly reported. In addition, the moduli of tin-based perovskites (including bulk, shear, and Young's modulus) are larger than that of Pb-based compounds, suggesting the enhanced flexibility for Sn-contained perovskites. Therefore, it is desirable to develop efficient flexible NIR PDs and imaging arrays using Sn- and Sn–Pb-based perovskites and explore their practical uses.

7.4. Stability

Stability concerns of perovskite-based NIR devices will inhibit the commercialization. Due to the degradation factors (e.g., water, oxygen, and light), unencapsulated perovskite-based NIR PDs normally have the short shelf life of less than several weeks. Compared with Pb-based perovskites, easy oxidation of Sn²⁺ to Sn⁴⁺ states in Sn-contained perovskites might result in the accelerated degradation of device performance. Notably, encapsulated Sn–Pb perovskite-based NIR PDs stored in a N₂-filled glove box have the long shelf life of over 200 days, suggesting the importance of encapsulation.^[25] Hence, developing effective encapsulated techniques is highly desirable for high-storage-stability perovskite NIR devices. Moreover, the operational stability that characterizes cycles (i.e., on/off states) of PDs under continuous illumination is highly significant in practical uses. Benefiting from the rapid progress in perovskite solar cells, perovskite-based devices show the stable photocurrent up to around 500 h under the illumination of 100 mW cm⁻², indicating the high light stability.^[59] Further, the prolonged cycle property of perovskite-based NIR PDs under various intensities of incident light should be carefully investigated. Additionally, the prolonged bending cycles of flexible perovskite-based NIR PDs at bending radii should be conducted.

To sum up, we have reviewed the current progress of hybrid halide perovskite-based NIR PDs and imaging arrays, in which Pb-/Sn-/Sn–Pb-based perovskites are employed. We first discuss the formation and optoelectronic properties of perovskites, and introduce the working mechanism and common figures of merit of PDs. To achieve NIR response, sub-bandgap

absorption and intraband transition of Pb-based perovskites are discussed for NIR absorption and detection. Besides, narrow-bandgap semiconductors (including silicon, CuO, TMDs, PbS QDs, PbSe QDs, organic macromolecule/dyes, and up-conversion nanocrystals) have been incorporated with Pb-based perovskites to obtain broadband PDs, some of which have the spectral response onset at 2.6 μm wavelength. To pursuit efficient NIR detection, pure Sn-based perovskite devices employ some strategies of template-assisted engineering and reducing additives to inhibit the natural oxidation of Sn²⁺ states. Furthermore, NIR devices with Sn–Pb mixed perovskites employ compositional engineering, passivation strategies, crystallization tuning, and encapsulation to realize high-efficiency and long shelf-life PDs with the high EQE of 70% at 940 nm wavelength. Finally, potential works, including spectral response extension, pixel integration, flexible devices, and stability, are discussed to boost perovskite-based NIR devices toward commercial applications.

Acknowledgements

The authors acknowledge the financial support from Guangdong Basic and Applied Basic Research Foundation (No. 2021A1515012198) and the Science and Technology Program of Guangzhou (No. 202102021084). J.H. acknowledges the financial support from the Key-Area Research and Development Program of Guangdong Province (No. 2019B010153001, 2020B010165001), Guangdong Basic and Applied Basic Research Foundation (No. 2019B1515120025), the 2016 Guangzhou Innovation and Entrepreneurship Leader Team (No. CXLJTD-201608), and Guangzhou Key Laboratory of IoT Identification IC (202002010002).

Conflict of Interest

The authors declare no conflict of interest.

Keywords

hybrid halide perovskites, imaging arrays, narrow-bandgap materials, near-infrared photodetectors, Sn–Pb narrow-bandgap perovskites

Received: December 7, 2021

Revised: January 26, 2022

Published online:

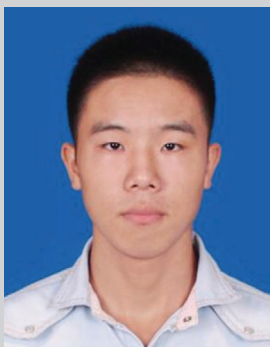
- [1] Q. Tian, L. Zhang, Y. Wei, W.-W. Fei, W.-H. Zhao, *Adv. Mech. Eng.* **2013**, 5, 546752.
- [2] J. V. Frangioni, *Curr. Opin. Chem. Biol.* **2003**, 7, 626.
- [3] G. Hong, A. L. Antaris, H. Dai, *Nat. Biomed. Eng.* **2017**, 1, 0010.
- [4] Y. C. Kim, K. H. Kim, D.-Y. Son, D.-N. Jeong, J.-Y. Seo, Y. S. Choi, I. T. Han, S. Y. Lee, N.-G. Park, *Nature* **2017**, 550, 87.
- [5] J. Li, K. Pu, *Chem. Soc. Rev.* **2019**, 48, 38.
- [6] C. Ng, E. C. Almaz, J. C. Simon, D. Fried, C. L. Darling, *J. Biomed. Opt.* **2019**, 24, 036002.
- [7] E. Adamopoulos, A. Bovero, F. Rinaudo, *Heritage Sci.* **2020**, 8, 53.
- [8] S. K. Piper, A. Krueger, S. P. Koch, J. Mehnert, C. Habermehl, J. Steinbrink, H. Obrig, C. H. Schmitz, *Neuroimage* **2014**, 85, 64.
- [9] T. Yokota, P. Zalar, M. Kaltenbrunner, H. Jinno, N. Matsuhisa, H. Kitanosako, Y. Tachibana, W. Yukita, M. Koizumi, T. Someya, *Sci. Adv.* **2016**, 2, e1501856.

- [10] K. Shou, C. Qu, Y. Sun, H. Chen, S. Chen, L. Zhang, H. Xu, X. Hong, A. Yu, Z. Cheng, *Adv. Funct. Mater.* **2017**, *27*, 1700995.
- [11] Z. Wu, Y. Zhai, W. Yao, N. Eedugurala, S. Zhang, L. Huang, X. Gu, J. D. Azoulay, T. N. Ng, *Adv. Funct. Mater.* **2018**, *28*, 1805738.
- [12] R. Saran, R. J. Curry, *Nat. Photonics* **2016**, *10*, 81.
- [13] N. Killilea, M. Wu, M. Sytnyk, A. A. Y. Amin, O. Mashkov, E. Spiecker, W. Heiss, *Adv. Funct. Mater.* **2019**, *29*, 1807964.
- [14] Q. Li, Y. Guo, Y. Liu, *Chem. Mater.* **2019**, *31*, 6359.
- [15] F. P. G. d. Arquer, A. Armin, P. Meredith, E. H. Sargent, *Nat. Rev. Mater.* **2017**, *2*, 16100.
- [16] D. Zhang, Y. Xu, W. Huang, X. Tian, Y. Xia, L. Xu, S. Fan, *Infrared Phys. Technol.* **2019**, *98*, 297.
- [17] F. Hao, C. C. Stoumpos, R. P. H. Chang, M. G. Kanatzidis, *J. Am. Chem. Soc.* **2014**, *136*, 8094.
- [18] G. Maculan, A. D. Sheikh, A. L. Abdelhady, M. I. Saidaminov, M. A. Haque, B. Murali, E. Alarousu, O. F. Mohammed, T. Wu, O. M. Bakr, *J. Phys. Chem. Lett.* **2015**, *6*, 3781.
- [19] C. C. Stoumpos, C. D. Malliakas, M. G. Kanatzidis, *Inorg. Chem.* **2013**, *52*, 9019.
- [20] S. Shrestha, R. Fischer, G. J. Matt, P. Feldner, T. Michel, A. Osvet, I. Levchuk, B. Merle, S. Golkar, H. Chen, S. F. Tedde, O. Schmidt, R. Hock, M. Rühlig, M. Göken, W. Heiss, G. Anton, C. J. Brabec, *Nat. Photonics* **2017**, *11*, 436.
- [21] W. Wei, Y. Zhang, Q. Xu, H. Wei, Y. Fang, Q. Wang, Y. Deng, T. Li, A. Gruverman, L. Cao, J. Huang, *Nat. Photonics* **2017**, *11*, 315.
- [22] F. Ye, H. Lin, H. Wu, L. Zhu, Z. Huang, D. Ouyang, G. Niu, W. C. H. Choy, *Adv. Funct. Mater.* **2019**, *29*, 1806984.
- [23] L. Dou, Y. M. Yang, J. You, Z. Hong, W. H. Chang, G. Li, Y. Yang, *Nat. Commun.* **2014**, *5*, 5404.
- [24] H. Liu, H. L. Zhu, Z. Wang, X. Wu, Z. Huang, M. R. Huque, J. A. Zapien, X. Lu, W. C. H. Choy, *Adv. Funct. Mater.* **2021**, *31*, 2010532.
- [25] H. L. Zhu, Z. Liang, Z. Huo, W. K. Ng, J. Mao, K. S. Wong, W. J. Yin, W. C. H. Choy, *Adv. Funct. Mater.* **2018**, *28*, 1706068.
- [26] H. L. Zhu, W. C. H. Choy, *Sol. RRL* **2018**, *2*, 1800146.
- [27] H. L. Zhu, J. Xiao, J. Mao, H. Zhang, Y. Zhao, W. C. H. Choy, *Adv. Funct. Mater.* **2017**, *27*, 1605469.
- [28] J. Song, J. Li, X. Li, L. Xu, Y. Dong, H. Zeng, *Adv. Mater.* **2015**, *27*, 7162.
- [29] H. Lin, L. Zhu, H. Huang, C. J. Reckmeier, C. J. Liang, A. L. Rogach, W. C. H. Choy, *Nanoscale* **2016**, *8*, 19846.
- [30] Y. Wang, X. Li, J. Song, L. Xiao, H. Zeng, H. Sun, *Adv. Mater.* **2015**, *27*, 7101.
- [31] Z. Li, M. Yang, J.-S. Park, S.-H. Wei, J. J. Berry, K. Zhu, *Chem. Mater.* **2016**, *28*, 284.
- [32] P. N. Rudd, J. Huang, *Trends Chem.* **2019**, *1*, 394.
- [33] Y. Zhao, C. Li, J. Jiang, B. Wang, L. Shen, *Small* **2020**, *16*, 2001534.
- [34] X. Xu, C.-C. Chueh, P. Jing, Z. Yang, X. Shi, T. Zhao, L. Y. Lin, A. K. Y. Jen, *Adv. Funct. Mater.* **2017**, *27*, 1701053.
- [35] F. Cao, W. Tian, M. Wang, M. Wang, L. Li, *InfoMat* **2020**, *2*, 577.
- [36] C. K. Liu, Q. Tai, N. Wang, G. Tang, Z. Hu, F. Yan, *ACS Appl. Mater. Interfaces* **2020**, *12*, 18769.
- [37] A. Waleed, M. M. Tavakoli, L. Gu, Z. Wang, D. Zhang, A. Manikandan, Q. Zhang, R. Zhang, Y. L. Chueh, Z. Fan, *Nano Lett.* **2017**, *17*, 523.
- [38] J. Q. Liu, Y. Gao, G. A. Wu, X. W. Tong, C. Xie, L. B. Luo, L. Liang, Y. C. Wu, *ACS Appl. Mater. Interfaces* **2018**, *10*, 27850.
- [39] B. H. Yu, Y. Cheng, M. Li, S. W. Tsang, F. So, *ACS Appl. Mater. Interfaces* **2018**, *10*, 15920.
- [40] T. Zhu, Y. Yang, L. Zheng, L. Liu, M. L. Becker, X. Gong, *Adv. Funct. Mater.* **2020**, *30*, 1909487.
- [41] Y. Zhang, Y. Liu, Z. Yang, S. F. Liu, *J. Energy Chem.* **2018**, *27*, 722.
- [42] C. Zou, Y. Xi, C.-Y. Huang, E. G. Keeler, T. Feng, S. Zhu, L. D. Pozzo, L. Y. Lin, *Adv. Opt. Mater.* **2018**, *6*, 1800324.
- [43] F. P. G. d. Arquer, X. Gong, R. P. Sabatini, M. Liu, G.-H. Kim, B. R. Sutherland, O. Voznyy, J. Xu, Y. Pang, S. Hoogland, D. Sinton, E. Sargent, *Nat. Commun.* **2017**, *8*, 14757.
- [44] X. Zou, Y. Li, G. Tang, P. You, F. Yan, *Small* **2019**, *15*, 1901004.
- [45] Q. Lin, A. Armin, P. L. Burn, P. Meredith, *Laser Photonics Rev.* **2016**, *10*, 1047.
- [46] X. Cheng, L. Jing, Y. Yuan, S. Du, J. Zhang, X. Zhan, J. Ding, H. Yu, G. Shi, *J. Phys. Chem. C* **2019**, *123*, 16669.
- [47] C. Liu, K. Wang, P. Du, E. Wang, X. Gong, A. J. Heeger, *Nanoscale* **2015**, *7*, 16460.
- [48] R. Guo, C. Bao, F. Gao, J. Tian, *Adv. Opt. Mater.* **2020**, *8*, 2000557.
- [49] Y. Yu, Y. Zhang, Z. Zhang, H. Zhang, X. Song, M. Cao, Y. Che, H. Dai, J. Yang, J. Wang, H. Zhang, J. Yao, *J. Phys. Chem. Lett.* **2017**, *8*, 445.
- [50] S. Chen, C. Teng, M. Zhang, Y. Li, D. Xie, G. Shi, *Adv. Mater.* **2016**, *28*, 5969.
- [51] L. Shen, Y. Lin, C. Bao, Y. Bai, Y. Deng, M. Wang, T. Li, Y. Lu, A. Gruverman, W. Li, J. Huang, *Mater. Horiz.* **2017**, *4*, 242.
- [52] N. Li, Y. Lei, W. K. E. Chana, F. Zhu, *J. Mater. Chem. C* **2019**, *7*, 4808.
- [53] Q. Lin, Z. Wang, M. Young, J. B. Patel, R. L. Milot, L. M. Maestro, R. R. Lunt, H. J. Snaith, M. B. Johnston, L. M. Herz, *Adv. Funct. Mater.* **2017**, *27*, 1702485.
- [54] X. Zhang, S. Yang, H. Zhou, J. Liang, H. Liu, H. Xia, X. Zhu, Y. Jiang, Q. Zhang, W. Hu, X. Zhuang, H. Liu, W. Hu, X. Wang, A. Pan, *Adv. Mater.* **2017**, *29*, 1604431.
- [55] Y. Ogomi, A. Morita, S. Tsukamoto, T. Saitho, N. Fujikawa, Q. Shen, T. Toyoda, K. Yoshino, S. S. Pandey, T. Ma, S. Hayase, *J. Phys. Chem. Lett.* **2014**, *5*, 1004.
- [56] I. Chung, B. Lee, J. He, R. P. H. Chang, M. G. Kanatzidis, *Nature* **2012**, *485*, 486.
- [57] S. J. Lee, S. S. Shin, Y. C. Kim, D. Kim, T. K. Ahn, J. H. Noh, J. Seo, S. I. Seok, *J. Am. Chem. Soc.* **2016**, *138*, 3974.
- [58] R. Lin, K. Xiao, Z. Qin, Q. Han, C. Zhang, M. Wei, M. I. Saidaminov, Y. Gao, J. Xu, M. Xiao, A. Li, J. Zhu, E. H. Sargent, H. Tan, *Nat. Energy* **2019**, *4*, 864.
- [59] K. Xiao, R. Lin, Q. Han, Y. Hou, Z. Qin, H. T. Nguyen, J. Wen, M. Wei, V. Yeddu, M. I. Saidaminov, Y. Gao, X. Luo, Y. Wang, H. Gao, C. Zhang, J. Xu, J. Zhu, E. H. Sargent, H. Tan, *Nat. Energy* **2020**, *5*, 870.
- [60] C. Xie, C.-K. Liu, H.-L. Loi, F. Yan, *Adv. Funct. Mater.* **2020**, *30*, 1903907.
- [61] J. Miao, F. Zhang, *J. Mater. Chem. C* **2019**, *7*, 1741.
- [62] H. Wang, D. H. Kim, *Chem. Soc. Rev.* **2017**, *46*, 5204.
- [63] W. Ke, C. C. Stoumpos, M. G. Kanatzidis, *Adv. Mater.* **2019**, *31*, 1803230.
- [64] C. Wang, Z. Song, C. Li, D. Zhao, Y. Yan, *Adv. Funct. Mater.* **2019**, *29*, 1808801.
- [65] S. Gu, R. Lin, Q. Han, Y. Gao, H. Tan, J. Zhu, *Adv. Mater.* **2020**, *32*, 1907392.
- [66] C. Li, Z. S. Wang, H. L. Zhu, D. Zhang, J. Q. Cheng, H. Lin, D. Ouyang, W. C. H. Choy, *Adv. Energy Mater.* **2018**, *8*, 1801954.
- [67] J. Li, Y. Shen, Y. Liu, F. Shi, X. Ren, T. Niu, K. Zhao, S. F. Liu, *ACS Appl. Mater. Interfaces* **2017**, *9*, 19176.
- [68] M. I. Saidaminov, A. L. Abdelhady, B. Murali, E. Alarousu, V. M. Burlakov, W. Peng, I. Dursun, L. Wang, Y. He, G. Maculan, A. Goriely, T. Wu, O. F. Mohammed, O. M. Bakr, *Nat. Commun.* **2015**, *6*, 7586.
- [69] D. Shi, V. Adinolfi, R. Cornin, M. Yuan, E. Alarousu, A. Buin, Y. Chen, S. Hoogland, A. Rothenberger, K. Katsiev, Y. Losovyj, X. Zhang, P. A. Dowben, O. F. Mohammed, E. H. Sargent, O. M. Bakr, *Science* **2015**, *347*, 519.
- [70] S. Tong, H. Wu, C. Zhang, S. Li, C. Wang, J. Shen, S. Xiao, J. He, J. Yang, J. Sun, Y. Gao, *Org. Electron.* **2017**, *49*, 347.

- [71] Q. Dong, Y. Fang, Y. Shao, P. Mulligan, J. Qiu, L. Cao, J. Huang, *Science* **2015**, *347*, 967.
- [72] D. N. Dirin, I. Cherniukh, S. Yakunin, Y. Shynkarenko, M. V. Kovalenko, *Chem. Mater.* **2016**, *28*, 8470.
- [73] Y. Liu, Y. Zhang, Z. Yang, D. Yang, X. Ren, L. Pang, S. Liu, *Adv. Mater.* **2016**, *28*, 9204.
- [74] H. S. Rao, W. G. Li, B. X. Chen, D. B. Kuang, C. Y. Su, *Adv. Mater.* **2017**, *29*, 1602639.
- [75] E. M. Hutter, G. E. Eperon, S. D. Stranks, T. J. Savenije, *J. Phys. Chem. Lett.* **2015**, *6*, 3082.
- [76] M. I. Saidaminov, A. L. Abdelhady, G. Maculan, O. M. Bakr, *Chem. Commun.* **2015**, *51*, 17658.
- [77] F. Yao, J. Peng, R. Li, W. Li, P. Gui, B. Li, C. Liu, C. Tao, Q. Lin, G. Fang, *Nat. Commun.* **2020**, *11*, 1194.
- [78] Y.-X. Chen, Q.-Q. Ge, Y. Shi, J. Liu, D.-J. Xue, J.-Y. Ma, J. Ding, H.-J. Yan, J.-S. Hu, L.-J. Wan, *J. Am. Chem. Soc.* **2016**, *138*, 16196.
- [79] Z. Yang, Y. Deng, X. Zhang, S. Wang, H. Chen, S. Yang, J. Khurgin, N. X. Fang, X. Zhang, R. Ma, *Adv. Mater.* **2018**, *30*, 1704333.
- [80] Y. Liu, Y. Zhang, Z. Yang, J. Feng, Z. Xu, Q. Li, M. Hu, H. Ye, X. Zhang, M. Liu, K. Zhao, S. F. Liu, *Mater. Today* **2019**, *22*, 67.
- [81] M. I. Saidaminov, V. Adinolfi, R. Comin, A. L. Abdelhady, W. Peng, I. Dursun, M. Yuan, S. Hoogland, E. H. Sargent, O. M. Bakr, *Nat. Commun.* **2015**, *6*, 8724.
- [82] P. K. Nayak, D. T. Moore, B. Wenger, S. Nayak, A. A. Haghighirad, A. Fineberg, N. K. Noel, O. G. Reid, G. Rumbles, P. Kukura, K. A. Vincent, H. J. Snaith, *Nat. Commun.* **2016**, *7*, 13303.
- [83] Y. Liu, H. Ye, Y. Zhang, K. Zhao, Z. Yang, Y. Yuan, H. Wu, G. Zhao, Z. Yang, J. Tang, Z. Xu, S. F. Liu, *Matter* **2019**, *1*, 465.
- [84] A. A. Zhumekenov, V. M. Burlakov, M. I. Saidaminov, A. Alofi, M. A. Haque, B. Turedi, B. Davaasuren, I. Dursun, N. Cho, A. M. El-Zohry, M. D. Bastiani, A. Giugni, B. Torre, E. D. Fabrizio, O. F. Mohammed, A. Rothenberger, T. Wu, A. Goriely, O. M. Bakr, *ACS Energy Lett.* **2017**, *2*, 1782.
- [85] P. Zhu, S. Gu, X. Shen, N. Xu, Y. Tan, S. Zhuang, Y. Deng, Z. Lu, Z. Wang, J. Zhu, *Nano Lett.* **2016**, *16*, 871.
- [86] J.-H. Im, J. Luo, M. Franckevičius, N. Pellet, P. Gao, T. Moehl, S. M. Zakeeruddin, M. K. Nazeeruddin, M. Grätzel, N.-G. Park, *Nano Lett.* **2015**, *15*, 2120.
- [87] J. Feng, C. Gong, H. Gao, W. Wen, Y. Gong, X. Jiang, B. Zhang, Y. Wu, Y. Wu, H. Fu, L. Jiang, X. Zhang, *Nat. Electron.* **2018**, *1*, 404.
- [88] W. Deng, L. Huang, X. Xu, X. Zhang, X. Jin, S.-T. Lee, J. Jie, *Nano Lett.* **2017**, *17*, 2482.
- [89] L. Gu, M. M. Tavakoli, D. Zhang, Q. Zhang, A. Waleed, Y. Xiao, K.-H. Tsui, Y. Lin, L. Liao, J. Wang, Z. Fan, *Adv. Mater.* **2016**, *28*, 9713.
- [90] R. Huang, D.-H. Lin, J.-Y. Liu, C.-Y. Wu, D. Wu, L.-B. Luo, *Sci. China Mater.* **2021**, *64*, 2497.
- [91] A. Bhorde, S. Nair, H. Borate, S. Pandharkar, R. Aher, A. Punde, A. Waghmare, P. Shinde, P. Vairale, R. Waykar, V. Doiphode, V. Jadkar, Y. Hase, S. Rondiya, N. Patil, M. Prasad, S. Jadkar, *New J. Chem.* **2020**, *44*, 11282.
- [92] S. Tang, Y. Deng, X. Zheng, Y. Bai, Y. Fang, Q. Dong, H. Wei, J. Huang, *Adv. Energy Mater.* **2017**, *7*, 1700302.
- [93] B. Dou, J. B. Whitaker, K. Bruening, D. T. Moore, L. M. Wheeler, J. Ryter, N. J. Breslin, J. J. Berry, S. M. Garner, F. S. Barnes, S. E. Shaheen, C. J. Tassone, K. Zhu, M. F. A. M. van Hest, *ACS Energy Lett.* **2018**, *3*, 2558.
- [94] S.-G. Li, K.-J. Jiang, M.-J. Su, X.-P. Cui, J.-H. Huang, Q.-Q. Zhang, X.-Q. Zhou, L.-M. Yang, Y.-L. Song, *J. Mater. Chem. A* **2015**, *3*, 9092.
- [95] D. K. Mohamad, J. Griffin, C. Bracher, A. T. Barrows, D. G. Lidzey, *Adv. Energy Mater.* **2016**, *6*, 1600994.
- [96] R. R. Søndergaard, M. Hösel, F. C. Krebs, *J. Polym. Sci., Part B: Polym. Phys.* **2013**, *51*, 16.
- [97] S. D. Stranks, G. E. Eperon, G. Grancini, C. Menelaou, M. J. P. Alcocer, T. Leijtens, L. M. Herz, A. Petrozza, H. J. Snaith, *Science* **2013**, *342*, 341.
- [98] A. Kojima, K. Teshima, Y. Shirai, T. Miyasaka, *J. Am. Chem. Soc.* **2009**, *131*, 6050.
- [99] N. J. Jeon, J. H. Noh, Y. C. Kim, W. S. Yang, S. Ryu, S. I. Seok, *Nat. Mater.* **2014**, *13*, 897.
- [100] M. Xiao, F. Huang, W. Huang, Y. Dkhissi, Y. Zhu, J. Etheridge, A. Gray-Weale, U. Bach, Y.-B. Cheng, L. Spiccia, *Angew. Chem.* **2014**, *126*, 10056.
- [101] Q. Chen, H. Zhou, Z. Hong, S. Luo, H.-S. Duan, H.-H. Wang, Y. Liu, G. Li, Y. Yang, *J. Am. Chem. Soc.* **2014**, *136*, 622.
- [102] H. Zhang, J. Mao, H. X. He, D. Zhang, H. L. Zhu, F. X. Xie, K. S. Wong, M. Gratzel, W. C. H. Choy, *Adv. Energy Mater.* **2015**, *5*, 1501354.
- [103] L. Zhu, B. Yuh, S. Schoen, X. Li, M. Aldighaithir, B. J. Richardson, A. Alamer, Q. Yu, *Nanoscale* **2016**, *8*, 7621.
- [104] F. Hao, C. C. Stoumpos, P. Guo, N. Zhou, T. J. Marks, R. P. H. Chang, M. G. Kanatzidis, *J. Am. Chem. Soc.* **2015**, *137*, 11445.
- [105] F. Zuo, S. T. Williams, P.-W. Liang, C.-C. Chueh, C.-Y. Liao, A. K.-Y. Jen, *Adv. Mater.* **2014**, *26*, 6454.
- [106] C.-M. Tsai, H.-P. Wu, S.-T. Chang, C.-F. Huang, C.-H. Wang, S. Narra, Y.-W. Yang, C.-L. Wang, C.-H. Hung, E. W.-G. Diau, *ACS Energy Lett.* **2016**, *1*, 1086.
- [107] C. Liu, W. Li, H. Li, C. Zhang, J. Fan, Y. Mai, *Nanoscale* **2017**, *9*, 13967.
- [108] Y. Zong, Z. Zhou, M. Chen, N. P. Padture, Y. Zhou, *Adv. Energy Mater.* **2018**, *8*, 1800997.
- [109] J. Tong, Z. Song, D. H. Kim, X. Chen, C. Chen, A. F. Palmstrom, P. F. Ndione, M. O. Reese, S. P. Dunfield, O. G. Reid, J. Liu, F. Zhang, S. P. Harvey, Z. Li, S. T. Christensen, G. Teeter, D. Zhao, M. M. Al-Jassim, M. F. A. M. van Hest, M. C. Beard, S. E. Shaheen, J. J. Berry, Y. Yan, K. Zhu, *Science* **2019**, *364*, 475.
- [110] B. Zhao, M. Abdi-Jalebi, M. Tabachnyk, H. Glass, V. S. Kamboj, W. Nie, A. J. Pearson, Y. Puttisong, K. C. Gödel, H. E. Beere, D. A. Ritchie, A. D. Mohite, S. E. Dutton, R. H. Friend, A. Sadhanala, *Adv. Mater.* **2017**, *29*, 1604744.
- [111] W. Liao, D. Zhao, Y. Yu, N. Shrestha, K. Ghimire, C. R. Grice, C. Wang, Y. Xiao, A. J. Cimaroli, R. J. Ellingson, N. J. Podraza, K. Zhu, R.-G. Xiong, Y. Yan, *J. Am. Chem. Soc.* **2016**, *138*, 12360.
- [112] Y. Zong, N. Wang, L. Zhang, M.-G. Ju, X. C. Zeng, X. W. Sun, Y. Zhou, N. P. Padture, *Angew. Chem., Int. Ed.* **2017**, *56*, 12658.
- [113] M. Liu, Z. Chen, Q. Xue, S. H. Cheung, S. K. So, H.-L. Yip, Y. Cao, *J. Mater. Chem. A* **2018**, *6*, 16347.
- [114] S. Shao, Y. Cui, H. Duim, X. Qiu, J. Dong, G. H. ten Brink, G. Portale, R. C. Chiechi, S. Zhang, J. Hou, M. A. Loi, *Adv. Mater.* **2018**, *30*, 1803703.
- [115] J. Im, C. C. Stoumpos, H. Jin, A. J. Freeman, M. G. Kanatzidis, *J. Phys. Chem. Lett.* **2015**, *6*, 3503.
- [116] J. Huang, Y. Yuan, Y. Shao, Y. Yan, *Nat. Rev. Mater.* **2017**, *2*, 17042.
- [117] A. Miyata, A. Mitioglu, P. Plochocka, O. Portugall, J. T.-W. Wang, S. D. Stranks, H. J. Snaith, R. J. Nicholas, *Nat. Phys.* **2015**, *11*, 582.
- [118] K. Galkowski, A. Mitioglu, A. Miyata, P. Plochocka, O. Portugall, G. E. Eperon, J. T.-W. Wang, T. Stergiopoulos, S. D. Stranks, H. J. Snaith, R. J. Nicholas, *Energy Environ. Sci.* **2016**, *9*, 962.
- [119] Y. Shao, Z. Xiao, C. Bi, Y. Yuan, J. Huang, *Nat. Commun.* **2014**, *5*, 5784.
- [120] Y. Liu, Z. Yang, D. Cui, X. Ren, J. Sun, X. Liu, J. Zhang, Q. Wei, H. Fan, F. Yu, X. Zhang, C. Zhao, S. Liu, *Adv. Mater.* **2015**, *27*, 5176.
- [121] Y. Bi, E. M. Hutter, Y. Fang, Q. Dong, J. Huang, T. J. Savenije, *J. Phys. Chem. Lett.* **2016**, *7*, 923.
- [122] D. W. de Quilettes, S. M. Vorpahl, S. D. Stranks, H. Nagaoka, G. E. Eperon, M. E. Ziffer, H. J. Snaith, D. S. Ginger, *Science* **2015**, *348*, 683.

- [123] H. Wei, Y. Fang, P. Mulligan, W. Chuirazzi, H.-H. Fang, C. Wang, B. R. Ecker, Y. Gao, M. A. Loi, L. Cao, J. Huang, *Nat. Photonics* **2016**, *10*, 333.
- [124] C. Q. Xia, J. Peng, S. Poncé, J. B. Patel, A. D. Wright, T. W. Crothers, M. U. Rothmann, J. Borchert, R. L. Milot, H. Kraus, Q. Lin, F. Giustino, L. M. Herz, M. B. Johnston, *J. Phys. Chem. Lett.* **2021**, *12*, 3607.
- [125] C. Barugkin, J. Cong, T. Duong, S. Rahman, H. T. Nguyen, D. Macdonald, T. P. White, K. R. Catchpole, *J. Phys. Chem. Lett.* **2015**, *6*, 767.
- [126] S. De Wolf, J. Holovsky, S.-J. Moon, P. Löper, B. Niesen, M. Ledinsky, F.-J. Haug, J.-H. Yum, C. Ballif, *J. Phys. Chem. Lett.* **2014**, *5*, 1035.
- [127] H. P. Wang, S. Li, X. Liu, Z. Shi, X. Fang, J. H. He, *Adv. Mater.* **2021**, *33*, 2003309.
- [128] Z. M. Beiley, A. Pattantyus-Abraham, E. Hanelt, B. Chen, A. Kuznetsov, N. Kollí, E. H. Sargent, *Proc. SPIE* **2017**, *10100*, 8.
- [129] M. A. Green, M. J. Keevers, *Prog. Photovoltaics* **1995**, *3*, 189.
- [130] S. Valerio, S. Nicola, M. Daniela, C. Xueqing, W. Qingqian, M. Sofia, C. Silvia, R. Aurora, G. Agnieszka, P. Emanuele, M. M. Laura, Q. Francesco, S. Michele, M. Andrea, B. Giovanni, *Adv. Opt. Mater.* **2018**, *6*, 1701254.
- [131] Y. Yamada, T. Yamada, L. Q. Phuong, N. Maruyama, H. Nishimura, A. Wakamiya, Y. Murata, Y. Kanemitsu, *J. Am. Chem. Soc.* **2015**, *137*, 10456.
- [132] J. Even, L. Pedesseau, J.-M. Jancu, C. Katan, *J. Phys. Chem. Lett.* **2013**, *4*, 2999.
- [133] W.-J. Yin, J.-H. Yang, J. Kang, Y. Yan, S.-H. Wei, *J. Mater. Chem. A* **2015**, *3*, 8926.
- [134] W.-J. Yin, T. Shi, Y. Yan, *Adv. Mater.* **2014**, *26*, 4653.
- [135] Y. Yamada, T. Yamada, Y. Kanemitsu, *Bull. Chem. Soc. Jpn.* **2017**, *90*, 1129.
- [136] X. Wu, M. T. Trinh, D. Niesner, H. Zhu, Z. Norman, J. S. Owen, O. Yaffe, B. J. Kudisch, X. Y. Zhu, *J. Am. Chem. Soc.* **2015**, *137*, 2089.
- [137] N. K. Noel, A. Abate, S. D. Stranks, E. S. Parrott, V. M. Burlakov, A. Goriely, H. J. Snaith, *ACS Nano* **2014**, *8*, 9815.
- [138] J. Xu, A. Buin, A. H. Ip, W. Li, O. Voznyy, R. Comin, M. Yuan, S. Jeon, Z. Ning, J. J. McDowell, P. Kanjanaboos, J.-P. Sun, X. Lan, L. N. Quan, D. H. Kim, I. G. Hill, P. Maksymovych, E. H. Sargent, *Nat. Commun.* **2015**, *6*, 7081.
- [139] K. Yan, Z. Wei, T. Zhang, X. Zheng, M. Long, Z. Chen, W. Xie, T. Zhang, Y. Zhao, J. Xu, Y. Chai, S. Yang, *Adv. Funct. Mater.* **2016**, *26*, 8545.
- [140] R. Dong, Y. Fang, J. Chae, J. Dai, Z. Xiao, Q. Dong, Y. Yuan, A. Centrone, X. C. Zeng, J. Huang, *Adv. Mater.* **2015**, *27*, 1912.
- [141] W.-J. Yin, T. Shi, Y. Yan, *Appl. Phys. Lett.* **2014**, *104*, 063903.
- [142] K. Miyata, D. Meggiolaro, M. T. Trinh, P. P. Joshi, E. Mosconi, S. C. Jones, F. De Angelis, X.-Y. Zhu, *Sci. Adv.* **2017**, *3*, e1701217.
- [143] X. Y. Zhu, V. Podzorov, *J. Phys. Chem. Lett.* **2015**, *6*, 4758.
- [144] M. Bonn, K. Miyata, E. Hendry, X. Y. Zhu, *ACS Energy Lett.* **2017**, *2*, 2555.
- [145] A. Buin, P. Pietsch, J. Xu, O. Voznyy, A. H. Ip, R. Comin, E. H. Sargent, *Nano Lett.* **2014**, *14*, 6281.
- [146] A. Mahata, D. Meggiolaro, F. De Angelis, *J. Phys. Chem. Lett.* **2019**, *10*, 1790.
- [147] R. Shi, R. Long, *J. Phys. Chem. Lett.* **2019**, *10*, 6604.
- [148] F. Urbach, *Phys. Rev.* **1953**, *92*, 1324.
- [149] M. H. Du, *J. Mater. Chem. A* **2014**, *2*, 9091.
- [150] J. Yang, H. Sato, H. Orio, X. Liu, M. Fahlman, N. Ueno, H. Yoshida, T. Yamada, S. Kera, *J. Phys. Chem. Lett.* **2021**, *12*, 3773.
- [151] K. Tanaka, T. Takahashi, T. Ban, T. Kondo, K. Uchida, N. Miura, *Solid State Commun.* **2003**, *127*, 619.
- [152] E. Menéndez-Proupin, P. Palacios, P. Wahnón, J. C. Conesa, *Phys. Rev. B* **2014**, *90*, 045207.
- [153] G. Giorgi, J.-I. Fujisawa, H. Segawa, K. Yamashita, *J. Phys. Chem. Lett.* **2013**, *4*, 4213.
- [154] F. Brivio, K. T. Butler, A. Walsh, M. van Schilfgarde, *Phys. Rev. B* **2014**, *89*, 155204.
- [155] H. L. Zhu, J. Q. Cheng, D. Zhang, C. J. Liang, C. J. Reckmeier, H. Huang, A. L. Rogach, W. C. H. Choy, *ACS Nano* **2016**, *10*, 6808.
- [156] N. Alwadaï, M. A. Haque, S. Mitra, T. Flemban, Y. Pak, T. Wu, I. Roqan, *ACS Appl. Mater. Interfaces* **2017**, *9*, 37832.
- [157] L. Protesescu, S. Yakunin, M. I. Bodnarchuk, F. Krieg, R. Caputo, C. H. Hendon, R. X. Yang, A. Walsh, M. V. Kovalenko, *Nano Lett.* **2015**, *15*, 3692.
- [158] R. Prasanna, A. Gold-Parker, T. Leijtens, B. Conings, A. Babayigit, H.-G. Boyen, M. F. Toney, M. D. McGehee, *J. Am. Chem. Soc.* **2017**, *139*, 11117.
- [159] Y. Xie, J. Fan, C. Liu, S. Chi, Z. Wang, H. Yu, H. Zhang, Y. Mai, J. Wang, *Adv. Opt. Mater.* **2018**, *6*, 1700819.
- [160] F. Zhang, B. Yang, K. Zheng, S. Yang, Y. Li, W. Deng, R. He, *Nano-Micro Lett.* **2018**, *10*, 43.
- [161] B. Yang, F. Zhang, J. Chen, S. Yang, X. Xia, T. Pullerits, W. Deng, K. Han, *Adv. Mater.* **2017**, *29*, 1703758.
- [162] B. Yang, J. Chen, Q. Shi, Z. Wang, M. Gerhard, A. Dobrovolsky, I. G. Scheblykin, K. J. Karki, K. Han, T. Pullerits, *J. Phys. Chem. Lett.* **2018**, *9*, 5017.
- [163] Q. Lin, A. Armin, P. L. Burn, P. Meredith, *Nat. Photonics* **2015**, *9*, 687.
- [164] Y. Ji, W. Xu, N. Ding, H. Yang, H. Song, Q. Liu, H. Ågren, J. Widengren, H. Liu, *Light: Sci. Appl.* **2020**, *9*, 184.
- [165] F. Zhao, K. Xu, X. Luo, Y. Liang, Y. Peng, F. Lu, *Adv. Opt. Mater.* **2018**, *6*, 1700509.
- [166] H. Sun, W. Tian, F. Cao, J. Xiong, L. Li, *Adv. Mater.* **2018**, *30*, 1706986.
- [167] Z. X. Zhang, L. H. Zeng, X. W. Tong, Y. Gao, C. Xie, Y. H. Tsang, L. B. Luo, Y. C. Wu, *J. Phys. Chem. Lett.* **2018**, *9*, 1185.
- [168] F. Cao, Q. Liao, K. Deng, L. Chen, L. Li, Y. Zhang, *Nano Res.* **2018**, *11*, 1722.
- [169] L. H. Zeng, Q. M. Chen, Z. X. Zhang, D. Wu, H. Yuan, Y. Y. Li, W. Qarony, S. P. Lau, L. B. Luo, Y. H. Tsang, *Adv. Sci.* **2019**, *6*, 1901134.
- [170] W. Qu, S. Weng, L. Zhang, M. Sun, B. Liu, W. Du, Y. Zhang, *Appl. Phys. Express* **2020**, *13*, 121001.
- [171] D. Zhao, J. Huang, R. Qin, G. Yang, J. Yu, *Adv. Opt. Mater.* **2018**, *6*, 1800979.
- [172] Y. Wang, D. Yang, X. Zhou, D. Ma, A. Vadim, T. Ahamad, S. M. Alshehri, *Adv. Opt. Mater.* **2017**, *5*, 1700213.
- [173] W. Xu, Y. Guo, X. Zhang, L. Zheng, T. Zhu, D. Zhao, W. Hu, X. Gong, *Adv. Funct. Mater.* **2018**, *28*, 1705541.
- [174] G. Wu, R. Fu, J. Chen, W. Yang, J. Ren, X. Guo, Z. Ni, X. Pi, C.-Z. Li, H. Li, H. Chen, *Small* **2018**, *14*, 1802349.
- [175] C. Li, J. Lu, Y. Zhao, L. Sun, G. Wang, Y. Ma, S. Zhang, J. Zhou, L. Shen, W. Huang, *Small* **2019**, *15*, 1903599.
- [176] C. Li, H. Wang, F. Wang, T. Li, M. Xu, H. Wang, Z. Wang, X. Zhan, W. Hu, L. Shen, *Light: Sci. Appl.* **2020**, *9*, 31.
- [177] X. Geng, F. Wang, H. Tian, Q. Feng, H. Zhang, R. Liang, Y. Shen, Z. Ju, G.-Y. Gou, N. Deng, Y.-t. Li, J. Ren, D. Xie, Y. Yang, T.-L. Ren, *ACS Nano* **2020**, *14*, 2860.
- [178] Y. Cheng, Z. Shi, S. Yin, Y. Li, S. Li, W. Liang, D. Wu, Y. Tian, X. Li, *Sol. Energy Mater. Sol. Cells* **2020**, *204*, 110230.
- [179] H. Cong, X. Chu, F. Wan, Z. Chu, X. Wang, Y. Ma, J. Jiang, L. Shen, J. You, C. Xue, *Small Methods* **2021**, *5*, 2100517.
- [180] Z. Zhang, C. Xu, C. Zhu, X. Tong, C. Fu, J. Wang, Y. Cheng, L. Luo, *Sens. Actuators, A* **2021**, *332*, 113176.
- [181] C.-Y. Chang, K.-S. Wu, C.-Y. Chang, *Adv. Funct. Mater.* **2021**, <https://doi.org/10.1002/adfm.202108356>.
- [182] I. M. Asuo, D. Banerjee, A. Pignolet, R. Nechache, S. G. Cloutier, *Phys. Status Solidi RRL* **2021**, *15*, 2000537.

- [183] C. P. Veeramalai, S. Yang, R. Zhi, M. Sulaman, M. I. Saleem, Y. Cui, Y. Tang, Y. Jiang, L. Tang, B. Zou, *Adv. Opt. Mater.* **2020**, *8*, 2000215.
- [184] F.-X. Liang, L. Liang, X.-Y. Zhao, L.-B. Luo, Y.-H. Liu, X.-W. Tong, Z.-X. Zhang, J. C. A. Huang, *Adv. Opt. Mater.* **2019**, *7*, 1801392.
- [185] F. Huang, Y. Peng, G. Liu, *J. Phys. Chem. C* **2019**, *123*, 11073.
- [186] L. Mi, Y. Chang, Y. Zhang, E. Xu, Y. Jiang, *J. Mater. Chem. C* **2020**, *8*, 7812.
- [187] J.-Y. Zhang, J.-L. Xu, T. Chen, X. Gao, S.-D. Wang, *ACS Appl. Mater. Interfaces* **2019**, *11*, 44430.
- [188] I. Ka, L. F. Gerlein, I. M. Asuo, R. Nechache, S. G. Cloutier, *Nanoscale* **2018**, *10*, 9044.
- [189] Z. Duan, J. Ning, M. Chen, Y. Xiong, W. Yang, F. Xiao, S. V. Kershaw, N. Zhao, S. Xiao, A. L. Rogach, *ACS Appl. Mater. Interfaces* **2020**, *12*, 35201.
- [190] X. Luo, F. Zhao, L. Du, W. Lv, K. Xu, Y. Peng, Y. Wang, F. Lu, *npj Flexible Electron.* **2017**, *1*, 6.
- [191] X. Zhang, Q. Wang, Z. Jin, J. Zhang, S. F. Liu, *Nanoscale* **2017**, *9*, 6278.
- [192] A. Ren, J. Zou, H. Lai, Y. Huang, L. Yuan, H. Xu, K. Shen, H. Wang, S. Wei, Y. Wang, X. Hao, J. Zhang, D. Zhao, J. Wu, Z. Wang, *Mater. Horiz.* **2020**, *7*, 1901.
- [193] C. Xie, F. Yan, *ACS Appl. Mater. Interfaces* **2017**, *9*, 1569.
- [194] C. Xie, P. You, Z. Liu, L. Li, F. Yan, *Light: Sci. Appl.* **2017**, *6*, e17023.
- [195] D.-H. Kang, S. R. Pae, J. Shim, G. Yoo, J. Jeon, J. W. Leem, J. S. Yu, S. Lee, B. Shin, J.-H. Park, *Adv. Mater.* **2016**, *28*, 7799.
- [196] B. Du, W. Yang, Q. Jiang, H. Shan, D. Luo, B. Li, W. Tang, F. Lin, B. Shen, Q. Gong, X. Zhu, R. Zhu, Z. Fang, *Adv. Opt. Mater.* **2018**, *6*, 1701271.
- [197] Y. Lee, J. Kwon, E. Hwang, C. H. Ra, W. J. Yoo, J. H. Ahn, J. H. Park, J. H. Cho, *Adv. Mater.* **2015**, *27*, 41.
- [198] Y. Fang, Q. Dong, Y. Shao, Y. Yuan, J. Huang, *Nat. Photonics* **2015**, *9*, 679.
- [199] Y. Liu, J. Sun, Z. Yang, D. Yang, X. Ren, H. Xu, Z. Yang, S. F. Liu, *Adv. Opt. Mater.* **2016**, *4*, 1829.
- [200] F. Zhou, I. Abdelwahab, K. Leng, K. P. Loh, W. Ji, *Adv. Mater.* **2019**, *31*, 1904155.
- [201] G. Walters, B. R. Sutherland, S. Hoogland, D. Shi, R. Comin, D. P. Sellan, O. M. Bakr, E. H. Sargent, *ACS Nano* **2015**, *9*, 9340.
- [202] N. Li, Y. S. Lau, Z. Xiao, L. Ding, F. Zhu, *Adv. Opt. Mater.* **2018**, *6*, 1801084.
- [203] L. Xie, Z. Hong, J. Zan, Q. Wu, Z. Yang, X. Chen, X. Ou, X. Song, Y. He, J. Li, Q. Chen, H. Yang, *Adv. Mater.* **2021**, *33*, 2101852.
- [204] N. Ding, W. Xu, D. Zhou, G. Pan, D. Li, Y. Ji, X. Chen, D. Yang, X. Bai, C.-G. Ma, H. Song, *Nano Energy* **2020**, *76*, 105103.
- [205] W. Hu, H. Cong, W. Huang, Y. Huang, L. Chen, A. Pan, C. Xue, *Light: Sci. Appl.* **2019**, *8*, 106.
- [206] M. Han, J. Sun, M. Peng, N. Han, Z. Chen, D. Liu, Y. Guo, S. Zhao, C. Shan, T. Xu, X. Hao, W. Hu, Z. Yang, *J. Phys. Chem. C* **2019**, *123*, 17566.
- [207] C. K. Liu, Q. Tai, N. Wang, G. Tang, H. L. Loi, F. Yan, *Adv. Sci.* **2019**, *6*, 1900751.
- [208] I. Chung, J.-H. Song, J. Im, J. Androulakis, C. D. Malliakas, H. Li, A. J. Freeman, J. T. Kenney, M. G. Kanatzidis, *J. Am. Chem. Soc.* **2012**, *134*, 8579.
- [209] M. H. Kumar, S. Dharani, W. L. Leong, P. P. Boix, R. R. Prabhakar, T. Baikie, C. Shi, H. Ding, R. Ramesh, M. Asta, M. Graetzel, S. G. Mhaisalkar, N. Mathews, *Adv. Mater.* **2014**, *26*, 7122.
- [210] F. Hao, C. C. Stoumpos, D. H. Cao, R. P. H. Chang, M. G. Kanatzidis, *Nat. Photonics* **2014**, *8*, 489.
- [211] N. K. Noel, S. D. Stranks, A. Abate, C. Wehrenfennig, S. Guarnera, A.-A. Haghighirad, A. Sadhanala, G. E. Eperon, S. K. Pathak, M. B. Johnston, A. Petrozza, L. M. Herz, H. J. Snaith, *Energy Environ. Sci.* **2014**, *7*, 3061.
- [212] L. Ma, F. Hao, C. C. Stoumpos, B. T. Phelan, M. R. Wasielewski, M. G. Kanatzidis, *J. Am. Chem. Soc.* **2016**, *138*, 14750.
- [213] T.-B. Song, T. Yokoyama, C. C. Stoumpos, J. Logsdon, D. H. Cao, M. R. Wasielewski, S. Aramaki, M. G. Kanatzidis, *J. Am. Chem. Soc.* **2017**, *139*, 836.
- [214] S. J. Lee, S. S. Shin, J. Im, T. K. Ahn, J. H. Noh, N. J. Jeon, S. I. Seok, J. Seo, *ACS Energy Lett.* **2018**, *3*, 46.
- [215] K. Korshunova, L. Winterfeld, W. J. D. Beenken, E. Runge, *Phys. Status Solidi B* **2016**, *253*, 1907.
- [216] W. Wang, D. Zhao, F. Zhang, L. Li, M. Du, C. Wang, Y. Yu, Q. Huang, M. Zhang, L. Li, J. Miao, Z. Lou, G. Shen, Y. Fang, Y. Yan, *Adv. Funct. Mater.* **2017**, *27*, 1703953.
- [217] N. Ma, J. Jiang, Y. Zhao, L. He, Y. Ma, H. Wang, L. Zhang, C. Shan, L. Shen, W. Hu, *Nano Energy* **2021**, *86*, 106113.
- [218] H. L. Zhu, H. Lin, Z. Song, Z. Wang, F. Ye, H. Zhang, W. Yin, Y. Yan, W. C. H. Choy, *ACS Nano* **2019**, *13*, 11800.
- [219] Y. Wang, C. Chen, T. Zou, L. Yan, C. Liu, X. Du, S. Zhang, H. Zhou, *Adv. Mater. Technol.* **2020**, *5*, 1900752.
- [220] F. Cao, J. Chen, D. Yu, S. Wang, X. Xu, J. Liu, Z. Han, B. Huang, Y. Gu, K. L. Choy, H. Zeng, *Adv. Mater.* **2020**, *32*, 1905362.
- [221] J. Liu, Y. Zou, B. Huang, Y. Gu, Y. Yang, Z. Han, Y. Zhang, X. Xu, H. Zeng, *Nanoscale* **2020**, *12*, 20386.
- [222] L. Yan, X. Du, C. Liu, S. Zhang, H. Zhou, *Phys. Status Solidi A* **2019**, *216*, 1900417.
- [223] C. Jo, S. Lee, J. Kim, J. S. Heo, D.-W. Kang, S. K. Park, *ACS Appl. Mater. Interfaces* **2020**, *12*, 58038.
- [224] E. P. Devine, W. Qarony, A. Ahamed, A. S. Mayet, S. Ghandiparsi, C. Bartolo-Perez, A. F. Elrefaie, T. Yamada, S. Y. Wang, M. S. Islam, *IEEE Sens. J.* **2021**, *21*, 10556.
- [225] K. Nishimura, S. Shishido, Y. Miyake, H. Kanehara, Y. Sato, J. Hirase, Y. Sato, Y. Tomekawa, M. Yamasaki, M. Murakami, M. Harada, Y. Inoue, *Jpn. J. Appl. Phys.* **2018**, *57*, 1002B4.
- [226] A. Chaves, J. G. Azadani, H. Alsalman, D. R. da Costa, R. Frisenda, A. J. Chaves, S. H. Song, Y. D. Kim, D. He, J. Zhou, A. Castellanos-Gomez, F. M. Peeters, Z. Liu, C. L. Hinkle, S.-H. Oh, P. D. Ye, S. J. Koester, Y. H. Lee, P. Avouris, X. Wang, T. Low, *npj 2D Mater. Appl.* **2020**, *4*, 29.
- [227] J. Allen, *Physiol. Meas.* **2007**, *28*, R1.
- [228] Y. Khan, D. Han, A. Pierre, J. Ting, X. Wang, C. M. Lochner, G. Bovo, N. Yaacobi-Gross, C. Newsome, R. Wilson, A. C. Arias, *Proc. Natl. Acad. Sci. U. S. A.* **2018**, *115*, E11015.
- [229] A. J. M. van Breemen, R. Ollearo, S. Shanmugam, B. Peeters, L. C. J. M. Peters, R. L. van de Ketterij, I. Katsouras, H. B. Akkerman, C. H. Frijters, F. Di Giacomo, S. Veenstra, R. Andriessen, R. A. J. Janssen, E. A. Meulenkaamp, G. H. Gelinck, *Nat. Electron.* **2021**, *4*, 818.
- [230] J. Feng, *APL Mater.* **2014**, *2*, 081801.
- [231] J. Yu, M. Wang, S. Lin, *ACS Nano* **2016**, *10*, 11044.
- [232] L. Ćirić, K. Ashby, T. Abadie, M. Spina, M. Duchamp, B. Náfrádi, M. Kollár, L. Forró, E. Horváth, *Appl. Phys. Lett.* **2018**, *112*, 111901.



Luyao Mei received his B.Sc degree and M.Sc. degree from Nanchang University in 2017 and 2020, respectively. Now he is a Ph.D. student at Sun Yat-sen University. His research interests include formation of narrow-bandgap perovskite films, NIR photodetectors, and imaging arrays.



Zhanfeng Huang received his Ph.D. degree in Electronic Engineering from The University of Hong Kong in 2019. He is now an Assistant Professor at School of Microelectronics Science and Technology, Sun Yat-sen University. His research interests cover perovskite optoelectronics, near-infrared photodetectors, nanomaterials, and devices.



Lu Zhu is an Associate Professor at School of Microelectronics Science and Technology, Sun Yat-sen University. He received the B.Sc. degree from Northwest University in 2009, M.Sc. degree from Beijing Jiaotong University in 2012, Ph.D. degree from The University of Hong Kong in 2016, respectively. He conducted the postdoctoral work in The University of Hong Kong from 2016 to 2019. His research interests include UV–vis–NIR photodetectors and image sensors, NIR semiconductors, nanofabrication, flexible devices, and optoelectronic neuromorphic chips.